



UNIVERSITÀ
DEGLI STUDI
DI BRESCIA

DOTTORATO DI RICERCA IN
INGEGNERIA DELL'INFORMAZIONE

settore scientifico disciplinare

FIS/01 Fisica Sperimentale

FIS/03 Fisica della Materia

CICLO

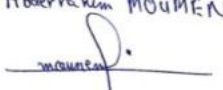
XXXIII

TITOLO TESI

**PREPARATION AND CHARACTERIZATION OF SEMICONDUCTOR
NANOSTRUCTURES FOR CHEMICAL SENSORS APPLICATIONS**

DOTTORANDO

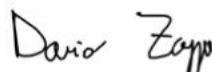
ABDERRAHIM MOUMEN

Abderrahim MOUMEN


RELATRICE: **PROF. ELISABETTA COMINI**



CORRELATORE: **DR. DARIO ZAPPA**



PHD COORDINATOR: **PROF. COSTANTINO DE ANGELIS**



Abstract (English)

Chemical gas sensors are devices that are able to change their properties according to the interaction of the surface with the surrounding atmosphere. Among these, conductometric sensors offer manifold advantages compared to other technologies in various applications, such as environmental monitoring, citizen security, and medical diagnosis, encompassing low cost, limited power consumption, reduced size/weight, good stability, and sensitivity to harmful compounds. In particular, nanostructures are promising sensing materials thanks to their favourable chemical reactivity and large surface-to-volume ratio, which provide a high active area for the interaction with the target analytes.

The research activities performed during these three years are dedicated to the synthesis and characterization of different semiconductor nanomaterials and the investigation of their chemical gas sensing performances in various application fields. Two classes of materials are explored: one dimensional metal oxides (1D MOX), including ZnO nanowires/nanorods and α -Bi₂O₃ nanowires, and two-dimensional transition metal dichalcogenides (2D TMDC), such as 2H-WSe₂ nanosheets.

1D MOX nanostructures are synthesized using Vapor Solid Liquid (VLS) mechanism, which uses a metal catalyst as a seed layer to assist and to control the growth. In this context, ZnO nanostructures are synthesized using different catalysts (Au, Pt, Ag and Cu) and the effect of these metal on growth and sensing mechanism is discussed. ZnO nanowires & nanorods, synthesized using Au as catalyst, show the best sensing performances towards H₂ at 350 °C with high response, good repeatability, small response and recovery times and good selectivity. Like ZnO, α -Bi₂O₃ nanowires are produced using a similar VLS mechanism, and the capability to detect small concentrations of acetone and ethanol is discussed. Sensing devices based on α -

Bi_2O_3 nanowires operated at $350\text{ }^\circ\text{C}$ are fast with full recovery of the conductance baseline and good long-term stability. Moreover, $\alpha\text{-Bi}_2\text{O}_3$ sensor is stable at high relative humidity level (90 %). Due to these features, $\alpha\text{-Bi}_2\text{O}_3$ nanowires are very promising for the development of conductometric sensor for breath analyser for diabetes diagnosis. Moreover, $\alpha\text{-Bi}_2\text{O}_3$ nanowires functionalized with noble metals (Au and Ag) and metal oxides (TiO_2) nanoparticles (NPs) have been investigated for hydrogen detection. In particular, the use of TiO_2 NPs leads to a great improvement of H_2 response (25 times higher than the pristine sample).

On the other hand, research activities focused on the synthesis of nanomaterials able to perform room temperature sensing. This has a great importance for the fabrication of low power consumption sensing devices for portable applications. 2H-WSe₂ nanosheets is grown using Atmospheric Pressure Chemical Vapor Deposition (APCVD). The number of layers that form the material, which can vary from bilayer up to 17 layers, is controlled by adjusting the number of droplets during the drop casting of a dispersion containing 2H-WSe₂ nanosheets onto the transducer. As a result, the bilayer 2H-WSe₂ based sensor shows the best response towards NO_2 at room temperature. This sensor has an excellent long-term stability (up to 9 months), full selectivity towards NO_2 and high stability at high relative humidity (90 %).

In summary, the results obtained in the synthesis of nanomaterials and the novel insights on the detection and transduction mechanisms perfectly satisfy the scope and the ultimate objectives expected from this thesis. As well as the good sensing performances achieved for both 1D ZnO and $\alpha\text{-Bi}_2\text{O}_3$ nanostructures, an extra chemical sensitization (spillover effect) through catalyst (Au as an example) on the sensing properties has been discussed in details. Moreover, the functionalization of $\alpha\text{-Bi}_2\text{O}_3$ nanowires with some metal and metal oxides to improve the sensing performance has been reported for the first time. Finally, beyond MOX nanostructures, 2D TMDC such as WSe₂ nanosheets are synthesized as a new class of nanomaterials for gas sensing,

showing an extraordinary capability for the fabrication of fully selective and highly sensitive NO₂ sensor at room temperature.

Abstract (Italiano)

I sensori di gas chimici sono dispositivi in grado di modificare le proprie proprietà in base all'interazione della superficie con l'atmosfera circostante. Tra questi, i sensori conduttometrici offrono molteplici vantaggi rispetto ad altre tecnologie in varie applicazioni, quali il monitoraggio ambientale, la sicurezza dei cittadini e la diagnosi medica, comprendendo basso costo, consumo energetico limitato, dimensioni/peso ridotti, buona stabilità e sensibilità ai composti nocivi. In particolare, le nanostrutture sono particolarmente promettenti come materiali di rilevamento grazie alla loro reattività chimica favorevole e all'ampio rapporto superficie/volume, che forniscono un'elevata area attiva per l'interazione con gli analiti target.

Le attività di ricerca contenute in questa tesi di Dottorato si sono focalizzate sulla sintesi e sulla caratterizzazione di diversi nanomateriali semiconduttori, ed in particolare allo studio delle loro prestazioni nell'ambito della rilevazione chimica di composti volatili in differenti campi applicativi. Due classi di materiali sono analizzate principalmente: gli ossidi metallici monodimensionali (1D MOX), tra cui nanofili/nanorod di ZnO e nanofili di α -Bi₂O₃, ed i dicalcogenuri di metalli di transizione bidimensionali (2D TMDC), tra i quali nanosheets di 2H-WSe₂.

Le nanostrutture MOX 1D sono state sintetizzate utilizzando il meccanismo di crescita "Vapore Liquido Solido" (VLS), il quale usa un catalizzatore metallico per supportare e controllare la crescita. In questo contesto, le nanostrutture di ZnO sono state sintetizzate utilizzando diversi catalizzatori (Au, Pt, Ag e Cu) ed è stato discusso l'effetto di questi metalli sulla crescita e sul meccanismo di rilevamento delle specie volatili di interesse. I nanofili e nanorod di ZnO, cresciuti utilizzando l'oro come catalizzatore, mostrano le migliori prestazioni per la rivelazione di H₂ a 350

°C, presentando una risposta elevata, buona ripetibilità, tempi di risposta e recupero ridotti ed una buona selettività. Similmente allo ZnO, i nanofili di α -Bi₂O₃ sono stati preparati utilizzando il meccanismo VLS, e si è studiata la capacità di rilevare piccole concentrazioni di acetone ed etanolo. Il sensore basato su nanofili di α -Bi₂O₃ funzionante a 350 °C è veloce, ed inoltre mostra il pieno recupero della linea di base della conduttanza ed ha una buona stabilità a lungo termine. Il sensore è stabile anche ad un livello di umidità relativa elevato (90%). I nanofili di α -Bi₂O₃ mostrano eccellenti prestazioni e sono molto promettenti per una loro possibile integrazione in analizzatori del respiro per la diagnosi del diabete. Inoltre, i nanofili α -Bi₂O₃, funzionalizzati con metalli nobili (Au e Ag) e nanoparticelle (NP) di ossidi metallici (TiO₂), sono stati studiati per il rilevamento dell'idrogeno. In particolare, le nanoparticelle di TiO₂ consentono di ottenere un sensibile miglioramento della risposta in presenza di H₂ (25 volte superiore rispetto al campione non funzionalizzato).

Infine, le attività di ricerca si sono concentrate anche sulla sintesi di nanomateriali in grado di rilevare gas a temperatura ambiente. Questo ha una straordinaria importanza per la fabbricazione di dispositivi a basso consumo energetico da introdurre in dispositivi portatili. In questo contesto, i nanosheets di 2H-WSe₂ sono stati cresciuti utilizzando la tecnica di Deposizione Chimica da Vapore a Pressione Atmosferica (APCVD). Il numero di strati che compone questo materiale (da 2 a 17) è controllato regolando il numero di gocce depositate sul trasduttore, contenenti i nanosheets di 2H-WSe₂, durante il processo di drop casting. Il sensore a doppio strato di 2H-WSe₂ mostra la migliore risposta nella rilevazione di NO₂ a temperatura ambiente. Questo dispositivo sensore ha un'eccellente stabilità a lungo termine (fino a 9 mesi), completa selettività verso NO₂ ed alta stabilità anche ad alti valori di umidità relativa (90%).

In sintesi, i risultati ottenuti nella sintesi dei nanomateriali ed i nuovi studi riguardanti i meccanismi di trasduzione e rilevamento soddisfano perfettamente gli obiettivi finali e le tematiche attese da

questo lavoro di tesi. Oltre alle buone prestazioni di rilevamento ottenute per le nanostrutture 1D ZnO e α -Bi₂O₃, è stata discussa e studiata una sensibilizzazione chimica aggiuntiva (effetto spillover) con proprietà di rilevamento attraverso l'uso di un catalizzatore (Au ad esempio). Inoltre, per la prima volta in letteratura, in questa tesi è stata studiata la funzionalizzazione di nanofili α -Bi₂O₃ con alcuni metalli ed ossidi metallici per migliorare le prestazioni come sensori chimici. Infine, oltre alle nanostrutture MOX, i TMDC 2D tra i quali i nanosheets di WSe₂ sono stati sintetizzati aprendo le porte ad una nuova classe di nanomateriali per il rilevamento di gas, mostrando straordinarie proprietà per la fabbricazione di sensori di NO₂ completamente selettivi ed altamente sensibili a temperatura ambiente.

Contents

Abstract (Italiano)	1
Abstract (English)	3
Introduction and objectives	10
Thesis organization	13
Chapter 1: Chemical gas sensors: state of the art and detection mechanism	15
Introduction	16
1.1. State of art on chemical sensors	16
1.1.1 Definition and classification	16
1.1.2 Semiconductors gas sensors	17
1.1.2.1 Sensing Characteristics	17
1.1.2.2 Advantages of chemical gas sensors based on semiconductors	19
1.1.2.3 Device structure	21
1.2. Chemical gas sensing mechanism	25
1.2.1. Phenomena involved in detection	25
1.2.2. Adsorption on the surface of semiconductors	26
1.2.2.1 Oxygen adsorption	26
1.2.2.2 Solid /Gas interaction and charge transfer	27
1.2.2.3 Size effect on sensing performance	29
Conclusion	31
Chapter 2: Semiconductor nanomaterials: growth and characteristics	32
Introduction	33
2.1. Nanomaterials growth, classes and dimensionality	33
2.1.1. Nanomaterials: Why nano-size matters against bulk?	33
2.1.2. Nanomaterials classification and dimensionality for chemical sensors applications.	35
2.1.3. Synthesis of nanomaterials: Top-down and bottom-up approaches	37
2.2. Metal oxides and metal dichalcogenides for chemical sensors applications	39

2.2.1. One dimensional (1D) metal oxides	39
2.2.2. Two dimensional (2D) metal dichalcogenides	41
2.3. Investigated materials	43
2.3.1. Zinc oxide	43
2.3.1.1. Crystalline structure	43
2.3.1.2. Properties and the application	44
2.3.2. Bismuth oxide	46
2.3.2.1. Crystalline structure	46
2.3.2.2. Properties and applications	48
2.3.3. Tungsten diselenide	49
2.3.3.1. Crystalline structure	49
2.3.3.2. Properties and applications	51
Conclusion.....	53
Chapter 3: Materials and methods	54
Introduction.....	55
3.1. Synthesis techniques	55
3.1.1. Magnetron sputtering	55
3.1.2. Vapor phase growth	57
3.1.2.1. Vapor-Liquid-Solid (VLS) growth mechanism	57
3.1.2.2. Atmospheric pressure chemical vapor deposition (APCVD)	59
3.2. Gas sensing setup	62
3.3. Synthesis of one dimensional ZnO nanostructures	66
3.3.1. Material preparation	66
3.3.2. Material characterization	67
3.4. Synthesis of α -Bi ₂ O ₃ nanowires	69
3.4.1. Material preparation	69
3.4.2. Synthesis of α -Bi ₂ O ₃ functionalized with nanoparticles.....	70
3.4.3. Material characterisation	71
3.5. Synthesis of 2H-WSe ₂ nanosheets	72
3.5.1. Material preparation	72
3.5.2. Material characterization	73
3.5.3. 2H-WSe ₂ device integration	74
Conclusion.....	75

Chapter 4. 1D ZnO nanostructures for chemical sensors applications.....	76
Introduction.....	77
4.1. Effect of catalysts on the morphology of 1D ZnO	77
4.2. Structural properties of ZnO nanostructures	81
4.3. Conductometric sensing: hydrogen (H ₂) detection	84
4.3.1 Working Principle	84
4.3.2 Catalyst effect on sensing characteristics	85
4.3.3 Sensing properties	88
Conclusion.....	95

Chapter 5. 1D α -Bi₂O₃ nanowires and nanoparticles - functionalized α -Bi₂O₃ for chemical sensors applications

Introduction.....	97
5.1. Morphological and structural properties of α -Bi ₂ O ₃ nanowires	97
5.2. Gas sensing properties	105
5.2.1. Gas sensing mechanism	105
5.2.2. Response towards acetone and ethanol.....	108
5.2.3. α -Bi ₂ O ₃ for Breath analysis application: Humidity effect, sensor kinetic, repeatability and selectivity	115
5.3. Au, TiO ₂ and Ag Functionalized α -Bi ₂ O ₃ NWs	121
5.3.1. Morphological analysis	121
5.3.2. H ₂ response improvement using nanoparticles - functionalized α -Bi ₂ O ₃ NWs sensors.....	122
Conclusion.....	123

Chapter 6. 2H-WSe₂ nanosheets for chemical sensors applications: NO₂ detection at room temperature.....

Introduction.....	126
6.1. Structural and morphological properties of WSe ₂ grown using APCVD.....	126

6.2.	X-ray Photoelectron Spectroscopy (XPS)	130
6.3.	Stability of 2H-WSe ₂ dispersion at different sonication frequency.....	133
6.4.	The effect of modulating the number of droplets on the number of layers.....	134
6.5.	Gas sensing properties	137
6.5.1.	Sensing mechanism of WSe ₂ nanosheets towards NO ₂ gas	137
6.5.2.	The response towards NO ₂	141
6.5.3.	The response towards NO ₂ , NH ₃ and H ₂ S.....	144
6.5.4.	Selectivity, humidity effect and long-term stability studies towards NO ₂	151
	Conclusion.....	156
	Conclusions	157
	References	160
	ACKNOWLEDGMENT.....	182
	List of publications	182
	List of conferences	184

Introduction and objectives

Nowadays, the specific demand for chemical detection and monitoring has emerged rapidly. Domestic or industrial accidents caused by dangerous chemical compounds and pollutants demonstrate the real need for early detection systems. As a result, these detection devices have many potential applications in significant fields such as transportation, environment, health, industry and agriculture. Taking environmental protection as an example, the environmental pollutants rising from several sources may contaminate water, air and land, causing a dramatic health risk. In fact, around the world, thousands of chemicals pose a risk to human and animal lives as well as the ecosystem (international development research centre: *Environmental pollution. (2010, December 13) Retrieved from: <https://www.idrc.ca/en/stories/environmental-pollution>*). Therefore, both governments and people are obliged to work together to do more efforts and to implement effective actions to solve such problem.

Based on World Health Organization (WHO) reports, 91% of the world's population lives in places where air quality exceeds WHO guideline limits: 4.2 million die every year as a result of exposure to ambient (outdoor) air pollution, and 3.8 million die every year as a result of household exposure to smoke from dirty cookstoves and fuels (World Health Organization : Air pollution. Retrieved from: <http://www.who.int/airpollution/en/>). These complex and urgent problems require innovative and action-oriented approaches for finding practical solutions for this health risk.

The need of effective chemical detector systems for environmental quality, as well as for the other applications mentioned before, continues to grow for several years in various fields such as analytical chemistry, environmental monitoring, food, pharmaceutical industries, automotive industry and more. In particular, in recent years the detection of toxic, noxious and/or flammable gases has become very important both for domestic and industrial points of view.

Pollutants/chemicals compounds such as H₂, NO_x, CO, CO₂, NH₃ and Volatile Organic Compounds (VOCs) such as acetone and ethanol have effects on human and animal health and also on the environment.

Currently, some gas analysis techniques are currently available to accurately determine the composition of a gaseous environment, such as gas chromatography and mass spectrometry. Nevertheless, these devices are inadequate in some cases because of their cost, size and difficulty of use. Among chemical sensors, conductometric sensors are sensors based on semiconductor materials such as metal oxides and metal dichalcogenides, which are particularly interesting because of their ease of use, they do not exhibit the same drawbacks of previously reported techniques and are a good alternative to these analysis systems.

On the other hand, the rapid development of nanoscience and nanotechnology has greatly pushed the scientific community and industrial companies to explore new features of both conventional and novel materials at the nanoscale level. Thanks to nanotechnology, it becomes possible to develop materials by controlling their structure at atomic level, resulting in new properties for the material to be used in all applications fields and in chemical sensors in particular. In this context, two classes of semiconductor nanomaterials with two different shapes (dimensionality) will be investigated in this thesis: one-dimensional metal oxide (1D MOX) such as nanowires and two-dimensional transition metal dichalcogenides (2D TMDC) nanosheets, to fabricate high-performance chemical sensors for different applications.

The main objectives of this thesis are:

- Synthesis and characterization of one-dimensional ZnO nanostructures using Vapor Liquid Solid (VLS) mechanism for chemical sensors applications. Since this growth mechanism is based mainly on the use of catalyst seeds to assist the growth of MOX, the idea is to study the effect of different catalysts (two of them are used for the first time to grow ZnO

for chemical sensor applications) on the growth of the 1D ZnO nanostructures as well as on the final sensing performances.

- The growth and investigation of structural, morphological and electrical properties of α - Bi_2O_3 nanowires and then investigating their sensing capability towards low concentration of acetone and ethanol at different relative humidity levels, to study its suitability as a new material in medical applications as breath analyzer. Moreover, the functionalization of metal oxides as strategy to improve further the sensing performances will also be targeted. In this context, noble metals (Au and Ag) and metal oxide (TiO_2) nanoparticles (NPs) - functionalization of α - Bi_2O_3 nanowires will be studied for the first time, providing a new system (NPs- Bi_2O_3) of functionalized -metal oxides for chemical sensors applications.
- Investigating the new class of semiconductors materials of 2D transition metal dichalcogenides (2D TMDC), and in particular 2H-WSe₂ nanosheets grown by APCVD, to fabricate sensors able to detect chemical compounds at room temperature. The capability of 2H-WSe₂ towards NO₂ gas will be investigated, and robust room-temperature NO₂ sensors will be fabricated. We thoroughly investigated the effect of the number of droplets (leading to several layers of 2H-WSe₂ with different thicknesses) on the sensing characteristics, including gas response, long-term stability, humidity and selectivity. This work will be of great interest in understanding and fabricating a low power consumption NO₂ sensor for its future miniaturization.

Thesis organization

Chapter 1: Presents the state of the art of chemical – gas sensors technology, including definitions and classifications of chemical sensors as well as the advantages of the sensors based on semiconductor materials against others. This chapter will also shed light on the gas sensing mechanism, explaining briefly all possible scenarios.

Chapter 2: Provides a literature review about nanomaterials synthesis and classifications in terms of shapes and dimensionality. Specifically, this chapter also sheds light on the 1D metal oxide and 2D transition metal dichalcogenides and their capability for chemical sensors applications, following by an overview of the investigated semiconductor materials that have been targeted in this manuscript, such as ZnO, α -Bi₂O₃ and 2H-WSe₂.

Chapter 3: Deals with the experimental setup that has been used to conduct this research with a detailed explanation of each instrument and the growth mechanism involved. Moreover, it provides a detailed description of the preparation and characterization of each material.

Chapter 4: This chapter reports the results on the effect of catalysts seeds (such as Au, Pt, Ag and Cu) on the growth of ZnO nanowires by VLS mechanism, as well as on the sensing performance. The morphological and structural properties will be explained in detail and the sensing capability towards hydrogen (H₂) will be investigated.

Chapter 5: Investigates the α -Bi₂O₃ nanowires synthesized by VLS mechanism including a comprehensive characterization of the samples. Here, performance of α -Bi₂O₃ nanowires will be demonstrated as a new material for breath analysis applications. Moreover, nanoparticles (NPs) -functionalized α -Bi₂O₃ will be investigated for chemical sensors applications.

Chapter 6: Describes the optimization of the synthesis of 2H-WSe₂ nanosheets, including the thermal stability of the nanosheets, the long-term stability of the dispersion and the exfoliation time. The structural and morphological characterizations will be carried out. Then, the NO₂ sensing properties will be investigated to fabricate room temperature NO₂ sensors based on these WSe₂ nanosheets.

Chapter 1: Chemical gas sensors: state of the art and detection mechanism

Introduction

Nowadays, the detection of toxic and inflammable chemical compounds has great importance in different fields. Therefore, a huge effort has been spent to develop different high-performance chemical gas sensors. Among the one used nowadays, semiconductor-based conductometric gas sensors deserve special attention, due to their low cost of mass production, the possibility of miniaturization, their good sensitivity and high stability towards reducing and oxidizing gases. This chapter displays the state of the art of chemical gas sensors. In particular, the attention is applied to gas sensors based on semiconductor nanomaterials explaining both the conception and the detection mechanism.

1.1. State of art on chemical sensors

1.1.1. Definition and classification

A chemical sensor is a device that converts a chemical information into a measurable signal. This device is composed of three fundamental parts: a receptor, a transducer and a packaging module

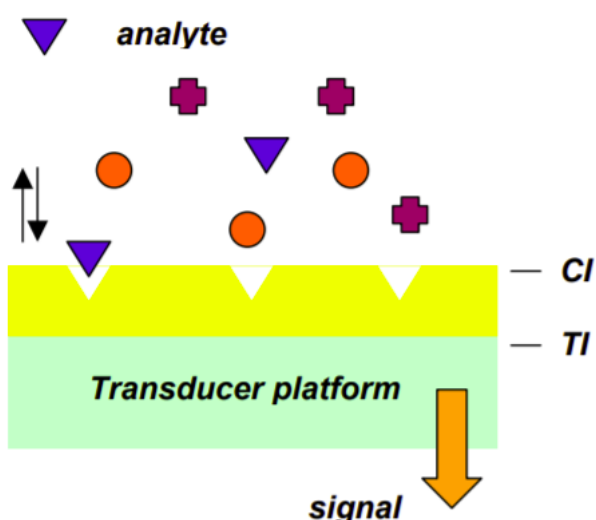


Figure 1. Cross-section of a chemical sensor. CI indicates the chemical interface, whereas TI indicates the transducer interface.

[1]. The receptor is the chemical recognition element, which defines the ability of the sensor surface to interact with the chemical information or analyte (molecules in gas or liquid phase) and transform it into a form of measurable energy. The interaction occurs at the receptor/analyte interface and the particular processes are an adsorption reaction, liquid-solid interactions or ion exchange. The transducer is the part of the sensor capable of transforming the measurable energy into an exploitable signal. These various parts are shown in Figure 1 [2]. Specifically, gas sensors are chemical sensors devices made up of a sensitive element, able to react with certain gas presented in the surrounding atmosphere. This reaction can be accompanied by a modification of the physical or chemical properties of the sensitive element, which, by a transduction process, generates an electrical, optical, mechanical or thermal signal. These variations can then be directly correlated with the evolution of the composition of the gas compound.

It is difficult to make an exhaustive classification of all gas sensors that are currently available or in development. However, depending on the operation mode, the materials used and the detection mechanisms, we can distinguish between several main types that can be used in the field of gas detection according to the transduction mechanism [2]. They can be electrical, mechanical, optical, thermal sensors, etc [3].

1.1.2. Semiconductors gas sensors

1.1.2.1. Sensor performance characteristics

Semiconductor based gas sensors are electrical sensors based on the variation of the electrical conductance or resistance of the semiconductor material under gas exposure. An high performant chemical-gas sensor must achieve many requirements, which depend on the objectives to be reached and on the targeted application. Among the performance requirements, the most necessary are: response, stability, selectivity, response and recovery time and reproducibility

[4,5]. These sensing characteristics will be extracted and investigated in this thesis throughout the studies done on a different classes of semiconductor materials.

1. Response

The response is defined as the variation of the electrical conductance of the sensor according to the variation of the gas concentration. We may say that a gas sensor is sensitive if a small variation of gas concentration (low ppm or even ppb concentration) generates a large variation in the output signal (electrical conductance). The general definition of the response is expressed as follow:

$$R = \frac{G_{gas} - G_{air}}{G_{air}} = \frac{\Delta G}{G_{air}} \quad or \quad R = \frac{G_{air} - G_{gas}}{G_{gas}} = \frac{\Delta G}{G_{gas}} \quad Eq 1$$

Where G is the electrical conductance towards gas (the signal output) (G_{gas}) or under air injection (G_{air}). Please note that the response towards a specific gas is represented in different forms, mainly depending on the nature of the gas (reducing or oxidizing) as well as the nature of the semiconductor material (n-type or p-type semiconductor). This will be investigated in detail in the following sections.

2. Selectivity

It depicts the ability of a sensor to detect one compound among others. It is defined as the ratio of the sensitivity of one gas over the sensitivity to other gases. The selectivity represents the major limitation and the challenging point for gas sensors based on metal oxides as sensitive material. However, some strategies can be applied to overcome this challenge such as bulk doping, surface decoration and heterojunction-based gas sensors.

3. Stability

The sensor is stable when, for fixed conditions, it maintains the same response and the constant baseline value over a certain time duration. The stability is principally related to sensor drifts over

time in the short or long term. The sensor drift results in the variation of the electrical conductance when it is exposed to an analyte under the same conditions. It has several origins related to both the sensitive material and measurement conditions such as measuring time, working temperature and relative humidity. These factors can affect both the response and conductance baseline and achieve different responses over (or after) a certain time. As a consequence, poor sensor repeatability may be achieved.

4. Response and recovery time

The response time is the time taken by the sensor to react to an analyte, and it is defined as the time required by the sensor to reach 90% of final conductance variation in presence of an analyte (gas). On the other hand, the time needed to return to the initial configuration once the analyte disappears is called recovery time, and it represents the time needed for a sensor to reach 10% of conductance variation during the recovery. It should be noted that it is often very difficult to estimate this time without taking into account the complete measurement system, including the volume of the measurement chamber and the gas flow rate that can be either small or large depending on the conditions of measured, affecting the stabilization time of the system.

5. Repeatability

The reproducibility of a gas sensor reflects its ability to generate the same response behavior towards the same gas, keeping the same gas test conditions. The system is reproducible if it responds to gas the same way regardless of the number of measurements and the time between measurements. The repeatability includes the response and recovery time and sensitivity.

1.1.2.2. Advantages of chemical gas sensors based on semiconductors

Several transduction principles are commercially exploited today to detect different analytes. Currently, the measure of gas concentrations (gas analyzers) is generally performed using

measuring stations based on physical principles such as gas chromatography–mass spectrometry (GC–MS) [6]. These systems are very efficient but also very bulky and require expensive equipment, which reduces their use for the analysis of gas samples taken from the real environment.

Current research, in agreement with industrial needs, aims to reduce dimensions, power consumption and price while at the same time increase performance [7,8]. Due to their low cost of mass production, the possibility of miniaturization, their good sensitivity towards reducing and oxidizing gases and high stability towards gases when operating at high temperature (such as in the case of metal oxides gas sensors), semiconductor gas sensors are the subject of special attention [9–13]. However, certain issues (such as selectivity) remain problematic and prevent the desired performance from being achieved with these systems [14,15]. The principle of operation of a semiconductor-based conductometric chemical sensor is based on the variation of the electrical conductance (or electrical resistance) of the semiconductor when interacting with gas [16–18]. Several types of materials can be used, such as conducting polymers, graphene, carbon nanotubes, transition metal chalcogenide, etc. [19–22]. Indeed, metal oxides have got intense attention because of their high sensitivity, good stability and low cost [23]. Besides, thanks to new synthesis techniques, it is possible to obtain good geometric and structural control (high aspect ratio, high porosity, nanoparticles, etc.), which allows a large exchange surface with the gas enhancing the sensing characteristics.

Table 1. Comparison of several types of chemical-gas sensors [3].

Characteristics	Type of chemical-gas sensors				
	Semi-conductor	Electro-chemical	Catalytic combustion	Thermal conductive	Infrared absorption
Sensitivity	++	+	+	--	++
Stability	+	--	+	+	+
Selectivity	--	+	--	--	++
Response time	++	-	+	+	-
Accuracy	+	+	+	+	++
Durability	+	-	+	+	++
Maintenance	++	+	++	+	-
Cost	++	+	++	+	-
Miniaturization	++	-	+	+	--
(++) excellent; (+) good ; (-) poor; (--) bad					

1.1.2.3. Device structure

The conductometric gas sensors are generally composed of:

- A sensitive semiconductor layer, which will interact directly with the target gas.
- Electrodes, to measure the electrical conductance and to follow the interaction process.
- The heater system, which modulates the temperature and activates the adsorption reactions on the surface of the semiconductor.

The heater should be electrically isolated from electrodes. These different elements are shown in Figure 2. The simplicity of design of such a system makes these devices very suitable for low-cost chemical sensors fabrication.

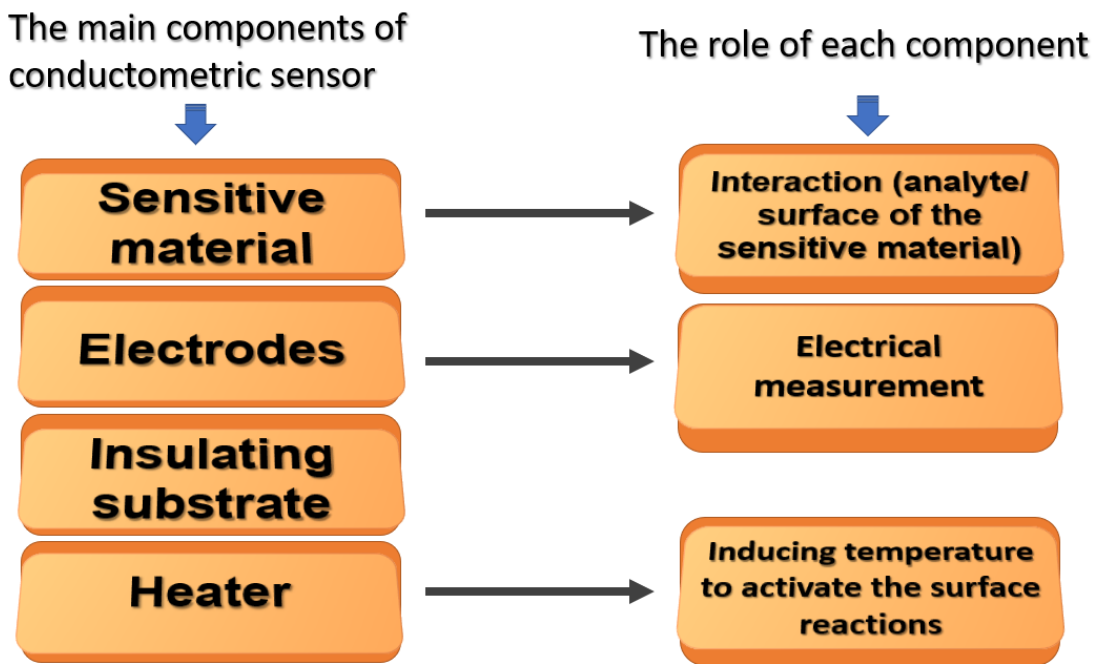


Figure 2. Functional schematic of a semiconductor gas sensor.

1) Electrodes

The electrodes establish the electrical contact with the sensitive material by conducting the charges of the sensitive material to the external measurement circuit [24]. The geometry and the nature of the material chosen for the electrodes strengthen the transfer of maximum charges from the sensitive material to the measurement circuit. The most common materials that can be used as electrodes are gold (Au) and platinum (Pt) thanks to their long-term stability during gas testing under high temperatures in different environments [25]. Although, other elements such as silver (Ag), palladium (Pd), or aluminum (Al) are also used for the construction of electrodes in gas sensors [24,26]. Indeed, in terms of geometry, we can distinguish two device structures: cylindrical layout structure in which the electrode is formed on the alumina tube or cylinder wafer as support as shown in Figure 3 [24], and the planar layout structure where the electrodes with parallel or interdigital geometry are formed on an alumina substrate. It has been shown that the interdigitated electrode is the best configuration, since it provides a high electrical contact area

between the electrodes. However, in this structure, the width of the digits (the finger) or the space between the electrodes has a huge impact on the stability and sensitivity of the gas sensor, as investigated in many reports [24,27].

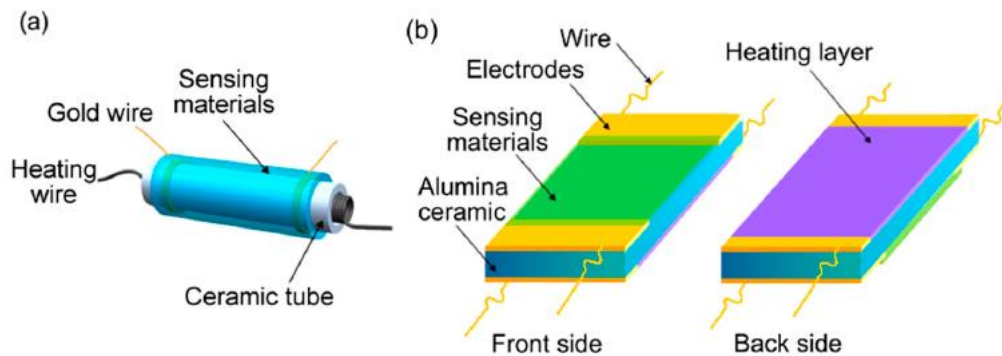


Figure 3. a) cylindrical and b) planar electrode geometries.

2) Heaters

The heater has great importance to operate the conductometric sensors. It allows the sensitive layer to reach the high temperatures required to activate the gas adsorption reactions at the surface of the semiconductor. Usually, metal oxides (MOX) gas sensors require high temperatures (500 °C or 600 °C) to be operated. Indeed, MOX materials have shown high stability at those temperatures. However, in the case of transition metal dichalcogenides (TMDC) the reactions must occur at low temperatures since the materials can be easily oxidized at high temperatures. The heater is considered as optional part in TMDC based gas sensors as they are activated at low or room temperature. Furthermore, the homogeneity of the temperature is very important, and for this reason the sensitive material should be heated uniformly. Different materials can be used as heater elements; however, noble materials such as platinum have shown high chemical stability at the highest temperature [28].

On the other hand, reducing the energy consumption of the sensor devices is another challenge to be solved for conductometric sensors [29]. As a solution, a micro-heater or micro electro mechanical system (MEMS) can be used as a hot-plate, resulting in a perfect solution to reduce the power of the sensor device for its future miniaturization. Recently, Figaro company (<https://www.figaro.co.jp/en/technicalinfo/miniaturization.html>) has invented a MEMS product that can reduce the consumed power to up to 15 MW. Many materials have been used as heating layer to construct micro-heater in MEMS such as SiC, Pt, poly-Si, silicon and TiN [30–33].

3) Sensitive material

Theoretically, there are no limitations of using any material to build conductometric gas sensors, regardless of physical, chemical, electrical or technological issues related to their design or structural properties. Many reports have investigated the characteristics and gas sensors' performance using different organic and inorganic materials. Carbon-based materials such as carbon nanotube and graphene, metal oxides semiconductors, metal dichalcogenides, conducting polymers and composite materials have shown great potential as gas sensors materials [19–22,34]. The sensitive material is the key for high-performance gas sensors fabrication. Indeed, reducing the size, increasing the aspect ratio and increasing the porosity of the nanostructures are required to enhance further the gas adsorption onto the surface of the materials. Moreover, when developing chemical sensors the most important requirements are size, dimensions and morphology control of the sensitive material, together with the nature or the composition of the material used. These factors affect the overall properties of a semiconductor gas sensor. Many efforts have been made to synthesize materials in different forms and shapes such as 0D, 1D, 2D and 3D nanostructures. Controlling the morphology and reducing the size of sensing material are crucial needs for developing a new generation of gas sensors. For example, taking the MOX, which are the most investigated and commercialized conductometric gas sensors

since 1962, a new generation of chemical sensors based on nanostructured one-dimensional metal oxides (MOX) has been recently investigated [12,35]. Morphologies such as nanowires show high stability and overcome the problem of coalescence that has been reported in the case of thin-film and powder morphology. The nanoscale size of these materials modulates the bandgap energy, affecting the electrical and optical properties and yielding to a high specific area (surface to volume ratio). The latter, in particular, enhances surface charge exchange between the gases and the MOX surface, thus providing high sensitivity and high stability under gas exposure [11]. Furthermore, a new class of materials i.e. 2D transition metal dichalcogenides (TMDC) have shown superior potential in chemical sensors applications due to their layered structures, which leads to an high mechanical stability that is a very important factor for flexible sensor fabrication [36]. In this thesis, 1D MOX and 2D TMDC will be investigated in detail as sensitive materials for conductometric gas sensors.

1.2. Chemical gas sensing mechanism

1.2.1. Phenomena involved in gas detection

The sensing mechanism is based on: (1) oxygen adsorption (from air) onto MOX surface and (2) surface reactions with the surrounding environment [37]. However, the chemical information (gaseous molecules) is translated through the electronic structure of the material and its surfaces into exploitable electrical characteristics, such as the change in electrical conductivity. Indeed, the interactions are essentially of adsorption reactions. Adsorption is the attachment of a molecule (gaseous molecules in our case) to the surface of a solid (the semiconductor sensitive material). In presence of a gas, the surface will be covered with different adsorbed gas molecules where two adsorption processes could occur [38]:

- Physical adsorption or physisorption: involves electrostatic forces such as Van der Waals and it occurs at low temperatures. During physisorption, the adsorbed and the adsorbent can be considered as two independent systems, in which adsorption occurs without charge exchange.
- Chemical adsorption or chemisorption: involves stronger interactions. It is accompanied by the transfer of charges between the adsorbed species and the adsorbent.

1.2.2. Adsorption on the surface of semiconductors

1.2.2.1. Oxygen adsorption

The adsorption of oxygen molecules on the surface of the sensitive materials such as in the case of semiconductor metal oxides mainly depends on the energy supplied, which is related to the operating temperature of the sensor. In other words, the sensitivity is a result of the surface state of the material together with the temperature. When changing the temperature there are effects due to the chemical kinetics of surface reactions, which can be exploited for detection.

Oxygen is of paramount importance in the reaction of metal oxides and the surroundings, and resides essentially on chemical adsorption in different forms depending on the working temperatures [39]. All scenarios that can occur during the adsorption of oxygen on the surface of SnO₂ as a function of temperature have been explained in detail in refs [40,41]. Oxygen may adsorb as O₂ (ads) (dissociative adsorption) or as O (ads) (non-dissociative adsorption) via physical adsorption (physisorption) at low temperatures (lower than 150 °C), or chemically adsorb (chemisorption) as O₂⁻ at 200 °C, or could chemisorb as O⁻ form at temperatures above 200 °C [42]. The chemisorption of oxygen modifies the electron concentration on MOX surface in opposite directions depending on conductivity type (n- or p-) of semiconductor, as explained in Figure 4 [43]. In the case of n-type semiconductor,

in which the majority carriers are electrons, the interaction with oxygen molecules (in the air) leads to a change of the electrical conductance caused by the creation of an electrons depletion layer on the surface. This depletion layer is due to electrons transfer from the conduction band into the adsorbed oxygen caused by the high electronic affinity of oxygen. In the case of p-type semiconductors, instead, the majority of carriers are holes. The adsorption of oxygen results in an increase of holes concentration in the valence band (electrons trapped by oxygen ionosorption) [19,27], creating holes accumulation layer (HAL) and thus increasing the conductance of p-type semiconductor under air exposure with high electrical conductance.

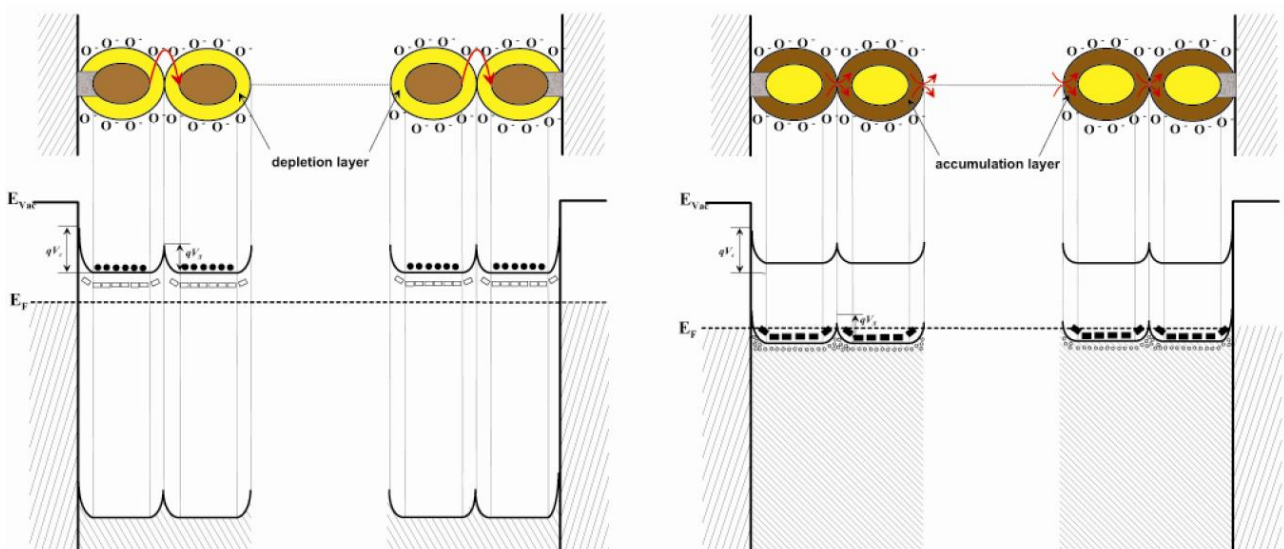


Figure 4. Conduction mechanism and the energy band diagram of n-type and p-type metal oxide semiconductors upon exposure to oxygen. Where E_F is the Fermi level and qV_s is the band bending.

1.2.2.2. Solid /Gas interaction and charge transfer

During gas injection, various possible scenarios may occur, depending on the semiconducting behavior of the material (n- or p-), the injected gases nature (reducing or oxidizing), electronic affinity, ionization energy, etc. In the case of the interaction of oxidizing gases such as (NO_2 , CO_2 , O_2) with the surface of the semiconductor material, two reactions may take place at the

surface either by simple adsorption on the surface or by reaction with ionosorbed oxygen. In the first case, since the oxidizing gases are acceptors of electrons, they trap more electrons. Their effect on the electrical conductance of the semiconductor is added to the effect of the pre-adsorbed oxygen explained in the last section (ionosorbed oxygen). For the second case, if the oxidizing gas interacts with the oxygen pre-adsorbed, the mechanism is often quite complex and several chemical reactions could occur.

To be precise, the ionosorption of oxygen affects the electrons depletion layer or/and the holes accumulation layer depending on the conductive nature of the semiconductor (SC) (n- or p-type). This can induce a decrease of the conductance (SC type n) or an increase of the conductance (SC type p), when applying a reducing gas, as it will react with the ionosorbed oxygen forming a new molecule that can be desorbed [19].

In summary, the surface conductivity of the semiconductor materials varies with the amount and the nature of adsorbed gas. When applying a reducing gas, which has a reducing character (electron donor), an increase in the electrons density occurs in an n-type semiconductor and therefore an increase in conductivity. In the case of a p-type semiconductor, a decrease in conductivity is a result of the compensation between the electrons and the positive carriers (holes) as explained in Figure 5 [46].

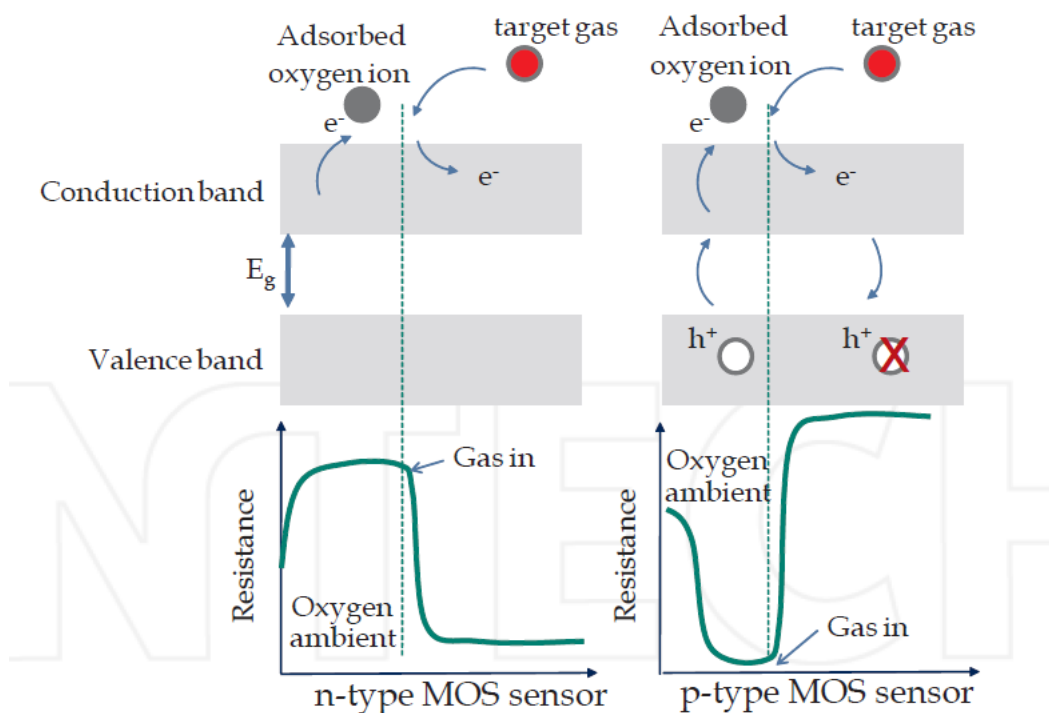


Figure 5. The behaviour of the electrical resistance of n- and p-type metal oxide semiconductors (MOS) upon exposure to oxidizing and reducing gases.

1.2.2.3. Size effect on sensing performance

For the sake of clarification and simplicity, we will consider the traditional porous film of metal oxides, which contains a system of connected grains, to study the effect of the particle size on the sensing properties of the conductometric sensors. Note that the size is only one of the factors that affect the performance of the sensor. However, other factors such as material defects, morphology and the kind of semiconductor material could also tune the sensing properties. Xu and Yamazoe et al. demonstrated that the sensor performances improve when the grains size

reduces as shown in Figure 6 [47]. They proposed a 'grain model' in which grain geometry factors such as the grain-size, grain-grain connectivity (neck control) and grain-boundary describe and control the conductance mechanism in thin films gas sensors. Several detailed studies have been reported on the 'grain model' in MOX thin films-based gas sensors. According to this model, decreasing grain size (D) leads to significant improvement of sensitivity. To be more precise, the sensing characteristics are strongly related to Debye length (L_D) and the depth of space charge layer (L) (Equations 2 and 3), which depends on D and is modulated by the adsorbed species [48].

$$L = L_D \sqrt{\frac{eV_s}{KT}} \quad \text{Eq 2}$$

$$L_D = \sqrt{\frac{\epsilon KT}{2\pi e^2 N}} \quad \text{Eq 3}$$

Where ϵ is the dielectric constant of the material, qV_s is the band bending, N is the concentration of charge carries, T is the absolute temperature and K is the Boltzmann constant. According to that semiquantitative grain model, three cases could be distinguished when we associate the particle size with the space charge layer as shown in Figure 6 [49]. These cases/approximations could be desirable or undesirable for high-performance gas sensors design [50].

If the grain size is much larger than the space charge layer ($D \gg 2l$), the grain boundary contact controls the electrical conductance and the response of the adsorbed species of the system (chain of connected grains). In this case, the system is not sensitive to the adsorbed species.

If the grain size is equal to the space charge layer ($D=2L$), here we may talk about 'neck control'. Each grain is connected with the neighbour by the neck and a space charge layer is formed around the neck, forming a conductance channel along with the system. In this case, the electrical conductance depends not only on the grain boundary barriers but also on the electrical conductance channels. Therefore, the material is more sensitive to the surface reaction.

When D is less than $2L$ ($D \ll 2L$), the space charge layer dominates and every grain is fully depleted. Therefore, the conductance of the system (chain of interconnected grains) is controlled by the conductance of the grains (grain control mechanism). In this case, there is no significant potential barrier in inter-particles for charge transport and the energy bands are flat. Small charge transfers due to surface reaction with the adsorbed species may induce a significant change in the electrical conductance of the system. This case is the most suitable for a highly sensitive gas sensor design.

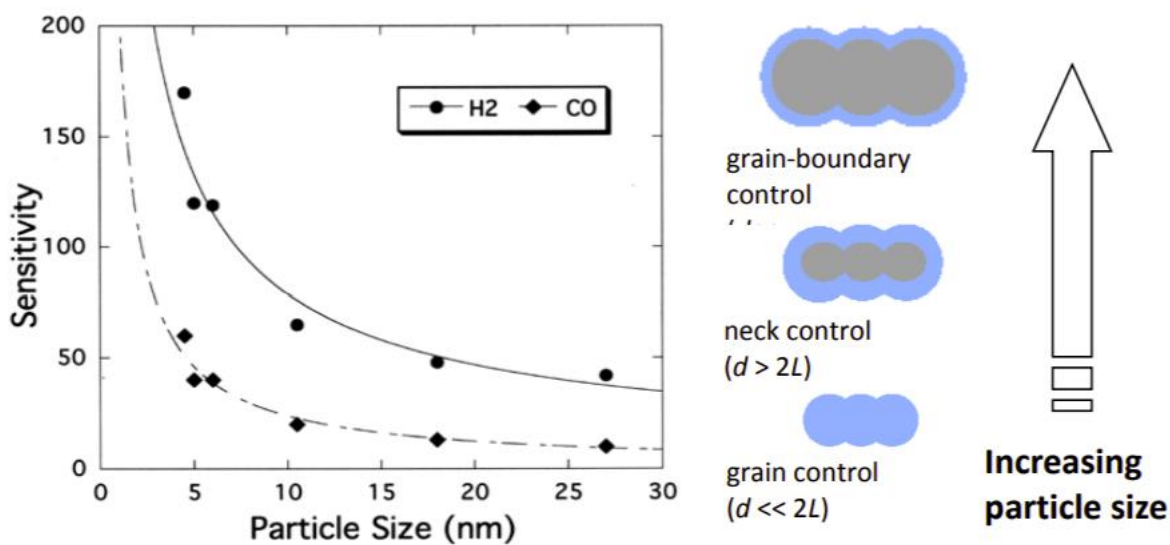


Figure 6. (Right) schematic explains the grain model in MOX thin films gas sensors. (Left) example of the effect of the size of SnO₂ particles on the sensitivity.

Conclusion

In this chapter, the state of art of chemical gas sensors have has been displayed including the definitions and classifications. Afterward, the conductometric gas sensors based on semiconductor material have been explained in detail, highlighting the advantages of these devices, sensing characteristics, the mechanism of detection and the surface reaction. Moreover, the structure of these devices has been investigated. The simplicity of design of such a system makes these devices very suitable for low-cost chemical sensors fabrication.

Chapter 2: semiconductor nanomaterials: growth and characteristics

Introduction

Thanks to nanotechnology, the development of materials by controlling their structure at the atomic level became possible, resulting in new material characteristics for their utilization in many applications fields, and chemical sensors in particular. The nanoscale size of nanomaterials yields a high specific area (surface to volume ratio), enhancing the surface charge exchange between the volatile molecules and the surface, thus providing high sensitivity in presence of target compounds. Among the different materials, 1D metal oxides (MOX) and 2D transition metal dichalcogenides (TMDC) have shown superior potential in chemical sensors applications. This chapter provides general information about nanomaterials, including their synthesis and characteristics and application as chemical sensors. Most importantly, in this thesis an overview about the investigated nanomaterials, such as 1D ZnO nanostructures, α -Bi₂O₃ nanowires and 2D WSe₂, their properties, applications and capability as chemical sensors applications have been displayed.

2.1. Nanomaterials growth, classes and dimensionality

2.1.1. Nanomaterials: Why nano-size matters against bulk?

Nanomaterials are defined as materials or components that are controlled by nano-dimension sizes (smaller than 100 nanometer), such as nanofiber, nanowires, nanorods, nanoparticles, nanosheets, composite materials, thin layers or structural constituents, etc, and exhibit unique optical, electronic, or mechanical properties.

Several reports investigated the size threshold of the nanomaterials, proposing 100 nm as suggested by Paul et al. [51], or 50 nm as reported by Kittelson et al. [52]. The justification for choosing this upper limit was based on the similarity of some physicochemical properties with those of bulk materials when the size nanomaterial exceeds those values. Therefore, we can assume that materials respecting the size range from 1 to 100 nm being classified as nano [53].

Nanomaterials have attracted the scientific committee because of their huge impact in several application fields. This influence is rising by tuning their properties due to the transition from bulk to nano-material without including the shape effect. Unlike bulk materials that have constant properties regarding its size, the nano-size effect is driving the properties of the materials towards greater performances and can be attributed to two effects: surface effect and quantum confinement effect [54,55].

The surface effect depends principally on the fraction of atoms (or particle number per unit mass) that the surface of the material contains, which is greater in the case of nanomaterial due to the high surface to volume ratio compared with bulk material. As a result, the surface effect increases and the chemical reactivity enhances. At the same time, the confinement effect occurs mainly when the size of the nanomaterial is small enough, leading to a transition from continuous (in the case of bulk) to discrete energy levels with delocalized electrons states [56]. The Quantum confinement effect may modulate the optical and electronic behavior of the materials. As an illustration, it has been shown that the fluorescence of quantum dots (QDs) can be tuned between red and blue, and the bandgap energy of the semiconductor increases by decreasing the size of the QDs [57].

Furthermore, many modifications of matter could occur when working on materials at nanoscale level. One of the most important phenomena that should be pointed is the transition from non-magnetic (at Bulk state) to magnetic (at nanosize state) as observed in the case of Pt, Au as they gained magnetic moment when the size has been reduced [57]. Moreover, the melting point can be reduced, as well as changes can occur from chemistry point of view such as increasing the catalytic effect [53]. Taking into account the well-known definitions and characteristics, the chemical gas sensors applications are based mainly on surface reactions with the analyte, hence, the first key point for high sensing performance is the high specific area generated in nanomaterials.

2.1.2. Nanomaterials classification and dimensionality for chemical sensors applications

From the morphological point of view, nanostructured materials could be classified according to their dimensionality into four categories 0D, 1D, 2D and 3D nanostructures [58]. These morphologies have shown many advantages and disadvantages in detection applications.

Zero dimensional nanostructures: such as hollow spheres, spherical nanoparticles and quantum dots (QDs) are well investigated by several research groups in many applications and in chemical sensors applications in particular. The tunable size and shape, as well as very tiny size, provide high surface to volume ratio [59,60]. Examples such as ZnO and SnO₂ QDs have shown potentiality for high-performance H₂S sensor fabrication [61,62]. Composite materials-based quantum dots have shown a good selectivity towards H₂S at room temperatures and exhibited capability in the non-invasive exhaled diagnosis [63]. However, some drawbacks are a low conductivity, hard to be functionalized, difficulties in device integration and lack of device stability which limit the utilization of 0D nanostructures in practical detection applications [64].

One Dimensional nanostructures: such as nanowires, nanorods, nanobelts, nanofibers, etc, have shown huge potential in chemical sensors applications. Specifically, nanowires are the subject of interest in the last few years. Properties of 1D materials, such as high aspect ratio, enhanced surface/volume ratio, high crystallinity, high thermal stability, high carrier charge transport, compatibility with electronic devices with excellent stability, make 1D nanostructures a predominant choice for chemical sensors fabrication. Recently, metal oxide nanowires are considered as a new nanostructured material to build the new generation of nano-conductometric devices [4]. However few problems are still present, such as the lack of selectivity and the high working temperature required, which need some chemical modification to be overcome.

Two-dimensional nanostructures (2D): such as nanoflakes, nanosheets, are described by lateral size and large specific area as well as rich surface chemistry to make them an efficient candidate for monitoring and sensing applications. Together with graphene, single- and few-layer 2D TMDC nanostructures have an excellent functionalization ability and mechanical flexibility, which makes it the first choice for high-performance flexible chemical device fabrication [65–68]. However, problems such as large-scale production as well as thermal instability of 2D materials as in the case of metal chalcogenides are the drawbacks to be overcome for practical application.

Three-dimensional nanostructures (3D): Compared to the other dimensional nanostructures, 3D structures such as flowers-like structures and composites-like structures are bulk-like structure with a size exceeds 100 nm (out of nanometer range), which can limit (in some cases) their utilization in gas detection.

Based on the above explanations, conclusions can be extracted. Both morphological and materials composition information give and build an important summary that will be taken as a ground state for the following sections: huge capabilities and emerging properties of 1D and 2D morphologies, as well as the potential of metal oxides and transition metal dichalcogenides, have shown exceptional potential for high performance and new generations chemical sensors. MOX show physico-chemical properties that drive to the fabrication of chemical sensors activated at high and even at low temperatures with high stability. Layered transition metal dichalcogenides nanostructures, instead, are considered as a new class of materials for chemical sensors. Therefore, in the next sections, the focus will be on 1D metal oxide nanostructures, such as nanowires, and layered metal di-chalcogenides, such as nanosheets or flakes-based, nano-conductometric sensors.

2.1.3. Synthesis of nanomaterials: Top-down and bottom-up approaches

Nanostructured materials have been used for wide applications such as catalyst for chemical reactions, as vectors to transport drugs to target cells, biosensing, optoelectronics applications, energy and so on. Indeed, the shape or the morphology of the nanostructured materials control the physico-chemical properties resulting in an enhancement of the detection efficiency; however, these properties depend on morphologies and can be tuned via growth techniques, which can be either liquid, solid or vapor based approaches. Regardless of the morphology and the composition, the nanostructured materials could be synthesized using two different approaches: top-down and bottom up as shown in Figure 7 [69].

Top-down is the traditional approach of the actual semiconductor industry. A miniature device is realized by starting with bulk wafer by fragmentation or eliminating the non-needed parts and then adding other parts to get smaller nanosized objects. In a top-down approach, usually, the starting material is in solid-state and its fragmentation towards nanostructured material could occur using mechanical processing methods such as cutting, etching or using ball milling. Lithographic techniques such as photolithography or electron beam lithography, which are also known as <subtractive techniques>, have been involved to this approach and they are considered as the most popular top-down techniques frequently used in microelectronics fabrication also [70].

Bottom-up is also called <building up> approach. It consists in the construction of bigger structures and devices from smaller structures such as single atoms or molecules. This approach is based on the formation of cluster by self-assembling the atoms, which then comes to each other to form desirable nanosized material (nanostructure) [71]. Both vapor and liquid matter are the sources or the states of starting materials to build up nanostructures. Several techniques can be used to achieve the bottom-up approach, either by using physical vapor deposition (PVD) such as thermal and ion beam evaporation, or by using chemical techniques such as chemical vapor

deposition (CVD), sol-gel, hydrothermal, spray pyrolysis and microemulsion synthesis. The advantages and disadvantages of the both approaches are summarized in table 2.

Table 2. Advantages and disadvantages of top-down and bottom-up approaches.

Advantages/Disadvantages	top-down	bottom-up
Advantages	<p>Large scale production.</p> <p>Chemical purification is not required.</p> <p>High control of the size, shape and the thickness.</p>	<p>Nanosized nanoparticles, nanowires, nanorods, nanoshells, nanotubes can be synthesized.</p> <p>The deposition parameters are controllable.</p> <p>Nanometric size (1 to 20 nm).</p> <p>Low-cost production.</p>
Disadvantages	<p>Bigger size (20-1000nm).</p> <p>Difficulties in controlling the deposition parameters.</p> <p>Requires precise instrumentation, cleanroom and nanofabrication facilities.</p> <p>High cost production.</p>	<p>Difficulties in large scale production.</p> <p>Chemical purifications of nanomaterials are required.</p>

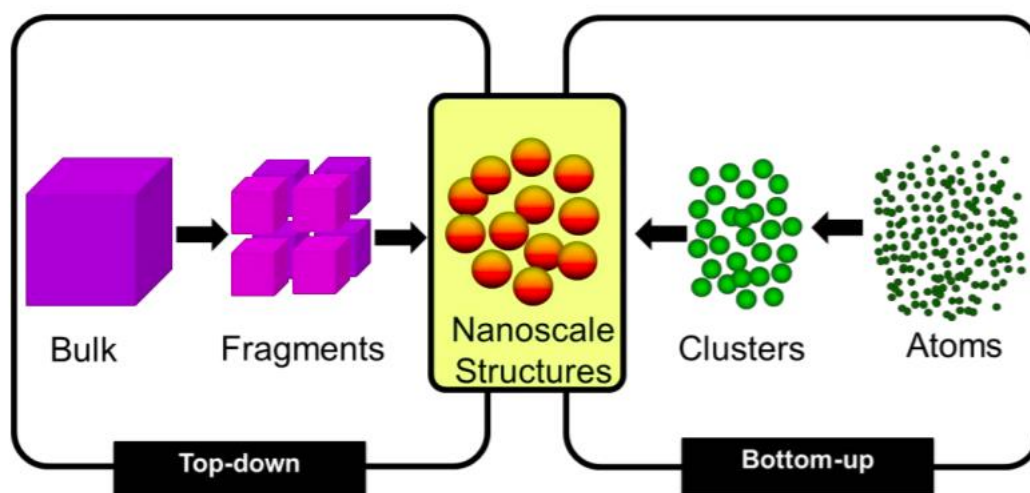


Figure 7. Top-down and bottom-up approaches to synthesis nanomaterials.

2.2. Metal oxides and transition metal dichalcogenides for chemical sensors applications

2.2.1. One dimensional (1D) metal oxides

Over the last decades, metal oxides have been considered as the first choice as sensitive materials for conductometric device fabrication. This selection is based on the physicochemical properties of metal oxides as well as their low-cost, high chemical stability, easy fabrication and long-term stability. Gas sensors based on MOX have received huge attention and many actions have been made to improve their capability in many applications, such in both outdoor and indoor monitoring, detection of toxic, combustible and harmful gases. The story has started in the 1954s by Heiland [72], 1960s by Seiyama et al. [73] and later by Shaver in the 1967s [74] when the first observations of the sensing mechanism underlying MOX sensors have been discovered. A change in the semiconductor properties in terms of electrical resistance of MOX semiconductors (mainly ZnO and WO₃) have been observed in a surrounding atmosphere containing oxygen, propane and other analytes. However, the first practical application of these devices has been

patented by Taguchi in 1971 using SnO₂ thick film as sensitive material and commercialized by Figaro Inc. [75].

In the classical band theory, defects in the metal oxide introduce additional discrete energy levels into the band structure of the material. These levels can be donors or acceptors depending on the nature of the defects. MOX semiconductors can be classified into two categories, n-type MOX semiconductors in which the majority charge carriers are the electrons (e⁻) and described by their oxygen vacancies such as in case of SnO₂, ZnO and WO₃, and p-type MOX semiconductors such as CuO, NiO, α-Bi₂O₃ in which the majority charge carriers are holes (h⁺) and characterized by the metal ions deficiency. In p-type semiconductors we observe the formation of acceptor levels located above the valence band. When the electron of the valence band is excited and passes over the acceptor level, a positive hole (h⁺) will be created in the valence band. Therefore, the conductance is associated with holes concentration. Figure 8 shows the most representative n-type materials that have been explored in chemical sensors applications. It is reported that n-type MOX semiconductors are the most explored semiconductors compared to p-types that represent only 10% [44]. The most used MOX for the fabrication of conductometric gas sensors are SnO₂, ZnO, TiO₂ and WO₃, due to their high chemical and good thermal stability in comparison with other MOX [3]. These characteristics allow the detection in critical environments even at high temperatures. Indeed, p-MOX have crucial advantages such as low humidity dependence and good catalytic properties, which make them good catalysts for conductometric sensors performances improvement [44]. Indeed, finding MOX nanomaterials specifically tailored for chemical sensing is crucial to discriminate the presence of a target molecule in presence of interfering species, such as in some challenging applications (for example breath analyses).

The demand for high-performance chemical sensors has pushed the scientific committee to employ different strategies to grow MOX nanostructures with increased sensing capability. As

well known, one common strategies to improve the sensing capability are bulk doping and surface decoration. However, the basic is to start with morphology itself by controlling the growth to achieve other shapes building a new generation of chemical sensors. In this context, 1D nanostructures have shown potential for the fabrication of chemical sensors devices. 1D metal oxides nanowires are characterized by their high crystallinity, high electronic transport as well as high stability. Moreover, 1D nanostructures are able to overcome one of the main issue of the so-called “second generation” of conductometric devices based on MOX thin films, which were suffering from the coalescent of the grains affecting the stability of the sensors at high temperature [76]. However, 1D MOX based conductometric sensors are not commercialized yet.

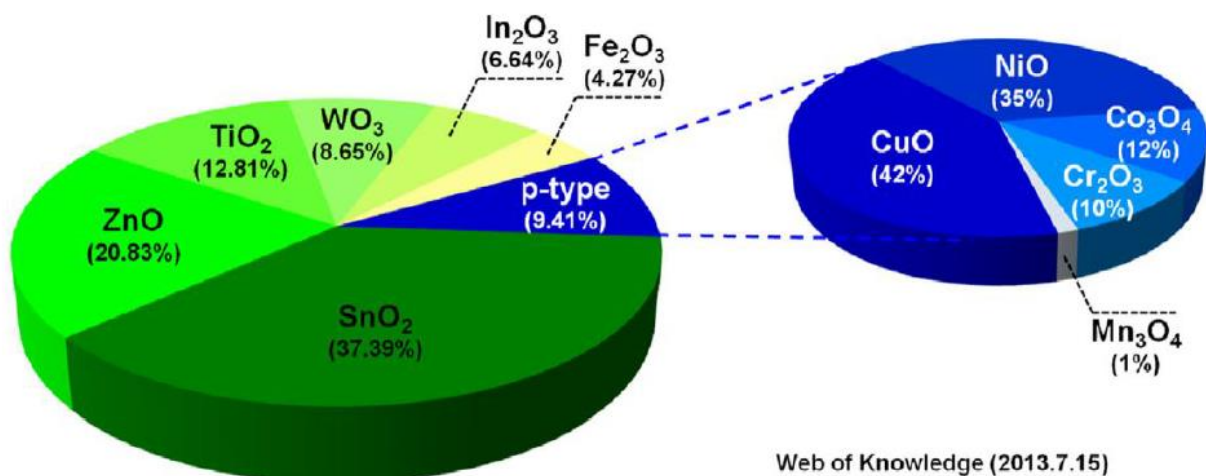


Figure 8. Studies on *n*- and *p*-type oxide semiconductor gas sensors (internet search of Web of Knowledge)

2.2.2. Two dimensional (2D) transition metal dichalcogenides

TMDC are inorganic compounds of type MX_2 where M is a transition metal atom (Ti, Zr, Hf, V, Nb, Ta, Mo, W, Tc, or Re) in groups IV, V, and VI of the periodic table and X is a chalcogen atom

(S, Se, or Te) (Figure 9). In these materials, one layer of transition atoms is sandwiched between two layers of chalcogen atoms (X-M-X). The 2D layered structure of TMDC is made up by strong molecular interlayer bonds and weak van der Waals interlayer bonds [77].

2D transition metal dichalcogenides materials possess a high surface-to-volume ratio that provides a large active surface for the interaction with the surrounding atmosphere [78], together with structural defects such as point defects, grain boundaries and edges that play significant roles in gas sensing. Such layered structure is very promising for gas sensors applications as it increases the surface reaction, adsorption and desorption, etc [79,80]. Moreover, it provides high mechanical stability for flexible and wearable sensors platform. The bandgap energy is related to the thickness of the material, and could be tuned easily to control the electronic properties of the material [79]. Recently, many TMDC materials have been investigated for gas sensors applications as a new class of materials, such as MoS₂, WS₂, MoSe₂, MoTe₂, etc [78,81–83]. Among them, MoS₂ has been investigated mostly [84]. The gas sensing properties of these materials depend mainly on the electronic properties, surface configurations as well as the carrier charge transfer. The gas /surface interactions are driven by the amount of charge transfer and the adsorption energy [77].

Transition Metal Dichalcogenides (TMDC) - MX ₂																			
M = Transition metal X = Chalcogen																			
1													13	14	15	16	17	18	
H													B	C	N	O	F	He	
Li	Be																		Ne
Na	Mg	3	4	5	6	7	8	9	10	11	12	Al	Si	P	S	Cl	Ar		
K	Ca	Sc	Ti	V	Cr	Mn	Fe	Co	Ni	Cu	Zn	Ga	Ge	As	Se	Br	Kr		
Rb	Sr	Y	Zr	Nb	Mo	Tc	Ru	Rh	Pd	Ag	Cd	In	Sn	Sb	Te	I	Xe		
Cs	Ba	Lu	Hf	Ta	W	Re	Os	Ir	Pt	Au	Hg	Tl	Pb	Bi	Po	At	Rn		
Fr	Ra	Lr	Rf	Db	Sg	Bh	Hs	Mt	Ds	Rg	Cn	Uut	Fl	Uup	Lv	Uus	Uuo		

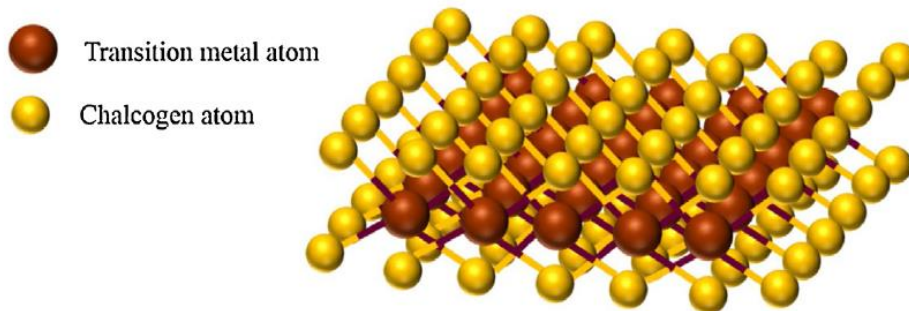


Figure 9. Schematic representation of the crystalline structure of the layered transition metal dichalcogenides material [37].

2.3. Investigated materials

2.3.1. Zinc oxide:

2.3.1.1. Crystalline structure

ZnO is considered as a n-type semiconductor (3.37eV), but in some cases p-type ZnO has also been obtained under specific synthetic conditions [85]. Three different crystalline structures of ZnO could be formed including hexagonal wurtzite, cubic zinc blend and cubic rocksalt structure [86]. Thermodynamically, the most stable phase of ZnO is the hexagonal wurtzite structure, in which each oxygen ions O^{2-} is coordinated by four Zn^{2+} ions in a tetrahedral form (**Figure 10**) [87]. However, growing ZnO on cubic substrate could lead to the formation of the zinc blend structure [88]. Instead, rocksalt structure can be formed only at high pressure [89] and it can also be stabilized by doping ZnO with metals such as Mg, Mn, and Co [90]. These crystalline structures are summarized in Table 3:

Table 3. Polymorphic phases of ZnO.

ZnO Phase	Symmetry	Lattice parameters	Group	Cell parameters	Ref.
Wurtzite	Hexagonal	$a=b \neq c$ $\alpha=\beta=90^\circ$, $\gamma=120^\circ$	P6_3mc	$a(\text{\AA}) = 3.249$ $c(\text{\AA}) = 5.204$	[91]
Rocksalt Zincblende	Cubic Cubic	$a=b=c$ $a=b=c$ $\alpha=\beta=\gamma=90^\circ$	Fm_3m F_43m	$a(\text{\AA}) = 4.37$ $a(\text{\AA}) = 4.463$	[92]

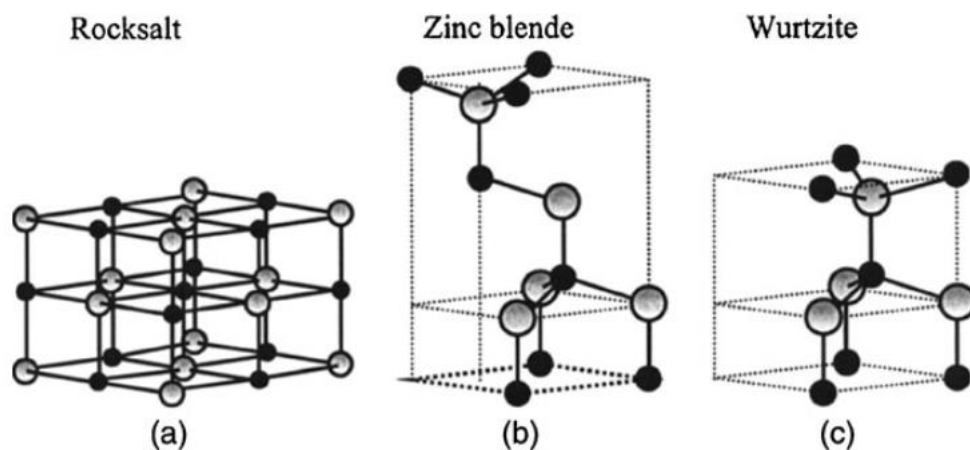


Figure 10. ZnO crystal structures: cubic rocksalt (a), cubic zincblende (b) and hexagonal Wurtzite (c). The shaded gray and black spheres represent zinc and oxygen atoms.

2.3.1.2. Properties and the applications

Generally, the transparent conductive oxide (TOC) such as ZnO thin films are highly transparent in the visible (VIS, 400-800) nm spectral range. However, doping ZnO with some elements could increase the bandgap, thus improving the transparency in this energy range. In this context, aluminum-doped zinc oxide (Al:ZnO) has great importance to tune the bandgap energy and also

increasing the electrical conductance, making ZnO a good material in solar cell application [93]. The conduction band (CB) and the valence band (VB) of ZnO are separated by the bandgap E_g . Figure 11 depicts the bandgap structure of wurtzite ZnO obtained from Density Functional Theory (DFT) calculations within the generalized gradient approximation including self-interaction corrections (GGA+U) [94]. As shown in Figure 11, ZnO has a direct bandgap of about 3.4 eV and presents high thermal and chemical stability, large exciton binding energy of 60 meV at room temperature and high electron mobility. Moreover, it is a non-toxic and environmentally-friendly material, making ZnO a suitable material for many applications.

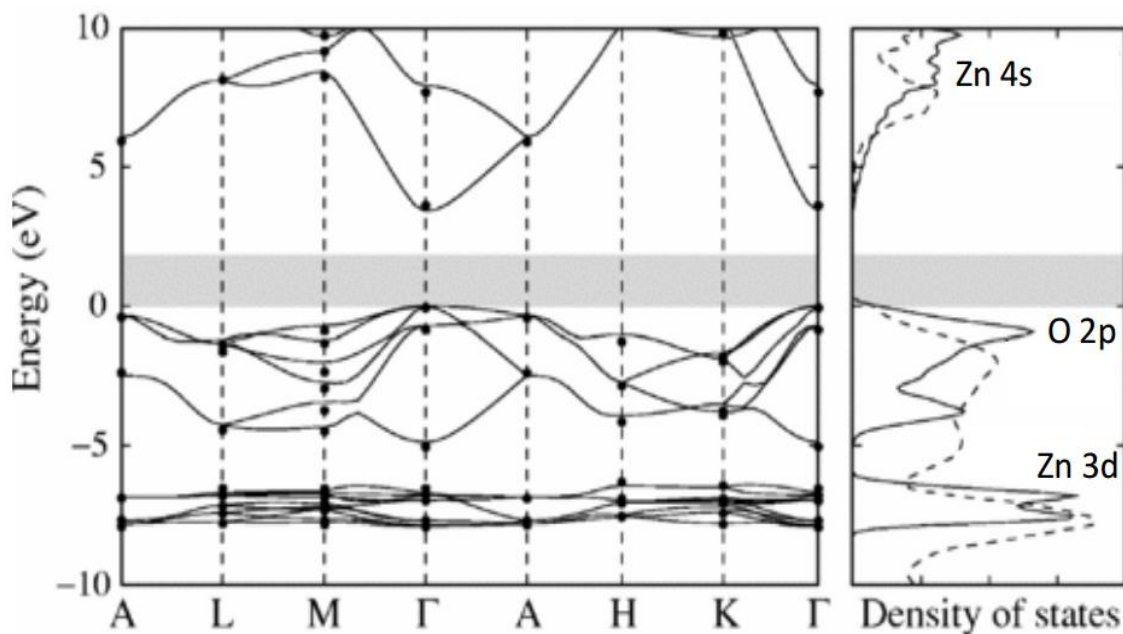


Figure 11. Bandgap structure of wurtzite ZnO obtained from density-functional theory calculations within the generalized-gradient approximation including self interaction corrections (GGA+U). The conduction band states have been rigidly shifted to the experimental bandgap. In the right plot, the solid and dashed lines show the calculated and experimental density of states, respectively. The gray area indicates the calculated bandgap [94].

ZnO also shows good piezoelectric properties. During the application of a mechanical stress, a displacement between the barycentres of positive and negative charges appears, thus creating a dipole moment. Gao et al. investigated the fundamental theory of nano-generator and nano-

piezotronics, determined that a lateral force of 80 nN exerted on a ZnO nanowire with a diameter of 50 nm and a length of 600 nm gave a potential of 0.3 V [95]. When a force of the same magnitude is applied along the axis of a nanowire, a potential difference of 0.4 V is obtained [96]. ZnO nanostructures have shown potentiality in lasers, thanks to the wide 3.47 eV gap and electron-hole exciton energy of 60 meV, providing emission in the UV range at room temperature (25 °C). ZnO is contemplated in the construction of lasers, although a high concentration of charge carriers is usually required for this type of application. In solar cell applications ZnO can be used as a thin film window layer in CIS, CIGS and CZTS photovoltaic panels due to its high transparency and high electrical conductance [97]. Moreover, in biosensing, nanomedicine and energy-based applications, ZnO has shown good performance [98,99].

Furthermore, and related to our application, the ZnO is considered as the second most used material in chemical sensors applications after SnO₂. However, the easy control of the morphology of ZnO towards nanosized ZnO nanomaterial, as well as the intrinsic physico-chemical properties make ZnO a perfect candidate for chemical detection [100].

2.3.2. Bismuth oxide:

2.3.2.1. Crystalline structure

In the last years, several efforts have been done to obtain pure and stable Bi₂O₃. Indeed, the synthesis as well as the investigation of the properties of the Bi₂O₃ nanomaterials have been and are still complicated due to the presence of polymorphs. Frequently, there is a mixture or a coexistence of bismuth oxide phases and the formation of non-stoichiometric oxides [101,102]. This complexity resides in existence of several crystalline structures which are divided into stable oxides structures (α -Bi₂O₃ and δ -Bi₂O₃) and metastable phases such as β -Bi₂O₃, γ -Bi₂O₃ and ω -Bi₂O₃. Each phase has different structural, electrical and optical characteristics. In general, temperature (heating or cooling) and

pressure are the factors responsible on the structural and crystallographic solid-solid transformations.

α - Bi_2O_3 is one of the most stable bismuth oxides. It is a p-type semiconductor with a monoclinic structure, belonging to space group symmetry of $P2_1/c$, with a band gap energy ranging from 2.29 to 3.31 eV (depending on nanostructure size and synthesis technique). The crystalline structure is shown in Figure 12 [102]. In this figure, the grey spheres are the bismuth (Bi) atoms and the red spheres represent the oxygen (O) atoms. The unit cell contains two bismuth (Bi-I and Bi-II) atoms. The first Bi atom (Bi-I) is coordinated by five oxygen atoms (two O-I, two O-III, and one O-II) while the second Bi atom (Bi-II) is coordinated by six oxygen atoms (two O-I, two O-III, and two O-II) [102]. The microstructural parameters are shown in Table 4.

Table 4. Crystalline structure, space group symmetry and lattice parameters of α - Bi_2O_3 .

Phase	Symmetry	Lattice parameters	Group	Cell parameters	Ref.
Bismite (α - Bi_2O_3)	Monoclinic	$a \neq b \neq c$ $\alpha = \beta = 90^\circ \neq \gamma$	$P2_1/c$	$a(\text{\AA}) = 5.86$ $c(\text{\AA}) = 8.15$ $c(\text{\AA}) = 7.54$ $\beta = 113.66^\circ$	JCPDS (Reference code. 98- 002-1528)

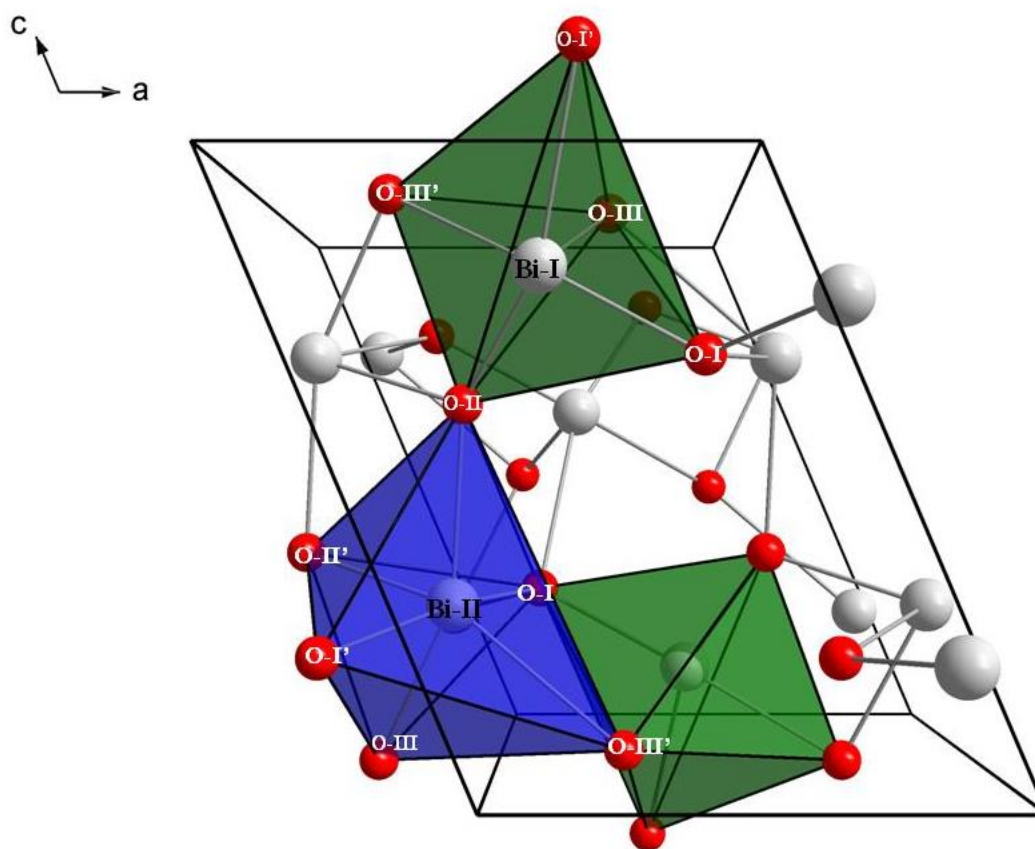


Figure 12. The crystal structure of α - Bi_2O_3

2.3.2.2. Properties and applications

Nanomaterials based on bismuth oxide polymorphs has shown potentiality as suitable visible light photocatalysts for the degradation of organic pollutants. However, the photocatalytic activity of the materials is heavily affected by many factors such as the morphology, specific area, the density of the nanostructures and orientation [103–105]. Among the bismuth oxides polymorphs, α - Bi_2O_3 is the less studied phase. The first investigation of the photocatalytic activity of α - Bi_2O_3 has been reported by Zhang et al., who synthesized the Bi_2O_3 powder by sonochemical method to degrade methyl orange by

applying visible light ($\lambda > 400$ nm) [106]. An highly photocatalytic activity of Bi_2O_3 has been observed, even higher than anatase TiO_2 in visible light [107]. Despite that, the photocatalytic activity of $\alpha\text{-Bi}_2\text{O}_3$ has not been fully studied and needs further investigation. On the other hand, α -bismuth oxide ($\alpha\text{-Bi}_2\text{O}_3$) has been investigated a new as a photoanode material in Dye Sensitized Solar Cells (DSSC), with efficiency that varies from 0.09 and 0.05% [108]. Bi_2O_3 based composite materials such as $\text{Bi}_2\text{O}_3\text{-MnO}_2$ have shown great potential as an electrochemical supercapacitor (ES) electrode for energy storage devices fabrication [109]. Moreover, bismuth oxide has shown good potential in medical applications [110]. A cytotoxicity study on Bi_2O_3 functionalized by hyaluronic acid (HA) has shown a good biocompatibility, showing contrast enhancement in tumor imaging by computer tomography (CT) [111].

Beyond conventional SnO_2 and ZnO -based materials for chemical sensors, a new nanoscaled material based on Bi_2O_3 nanowires will be investigated in this thesis for the development of nano-chemical sensor devices. $\alpha\text{-Bi}_2\text{O}_3$ is hardly reported as conductometric sensor for two reasons: (1) non-stoichiometric oxide is frequently formed and (2) n-type MOX- based chemical sensors dominate the literature concerning MOX chemical sensors, thanks to their sensing performances and stability even at high temperatures compared with p-MOX. Nevertheless, as cited before, this does not mean that p-type materials are not considerable in such applications. Indeed, p-MOX have a crucial advantage such as low humidity dependence as well as their good catalytic property, which make them good catalyst for conductometric sensors performances improvement [44].

2.3.3. Tungsten diselenide:

2.3.3.1. Crystalline structure

To date, 2D-layered TMDC, such as molybdenum disulfide (MoS_2), tungsten disulfide (WS_2) and tungsten selenide (WSe_2) have been explored as sensitive 2D layered materials that can detect NO_2 owing to their large surface-to-volume ratio with high surface activities and excellent compatibility with the current Si-based fabrication technologies for electronic devices [112–114]. Among the TMDC, WSe_2 is an inorganic compound that exists in two famous polymorphs which are 1T- WSe_2 and 2H- WSe_2 phases. 1T phase has a tetragonal symmetry and it has a metallic behavior. 2H phase, instead, has an hexagonal crystalline structure and is characterized by a semiconductor behavior. The 1T- WSe_2 phase is less stable and often transform to the 2H- WSe_2 phase. However, reversibility in phase transition processes between 1T and 2H phases has been found. It has been demonstrated that the 2H- WSe_2 could transform back to 1T- WSe_2 upon organolithium or organoalkali metal treatment, while annealing in argon atmosphere may convert 1T to 2H phase [115–117]. In the following sections, the focus will be on the semiconducting 2H- WSe_2 as sensitive material for conductometric sensor applications since the sensitive materials should have a semiconductor behavior to be used as performant conductometric sensors. Figure 14 shows the crystalline structure of 2H- WSe_2 . This has a hexagonal crystalline structure (belonging to $P6_3/mmc$ space group symmetry) in which each W atom is bonded/coordinated to/by six Se atoms or ligands that are arranged in trigonal prismatic molecular geometry. Moreover, each Se atom is bonded to three W atoms arranged in pyramidal molecular geometry. WSe_2 is made up of single layers of Se and W arranged periodically with hexagonal structure [118]. The stacking of one tungsten layer with two selenide layers forms (constructs) a Se-W-Se sandwich layer in which W atoms are located in between two Se layers. The values of the lattice parameters are shown in Table 5. The microstructural parameters such as a, c, z as well as the interlayer distance between the atoms (layers) are tabulated in Table 5 [119].

Table 5. Crystalline structure, space group symmetry and lattice parameters of 2H-WSe₂.

WSe ₂ Phase	Symmetry	Lattice parameters	Group	Cell parameters	Ref.
2H-WSe ₂	Hexagonal	$a=b\neq c$ $\alpha=\beta=90^\circ$, $\gamma=120^\circ$	P6 ₃ /m mc	$a(\text{\AA})=3.280$ $c(\text{\AA})=12.950$ $z(\text{\AA})=1.671$ $\omega(\text{\AA})=3.133$	[118,119]

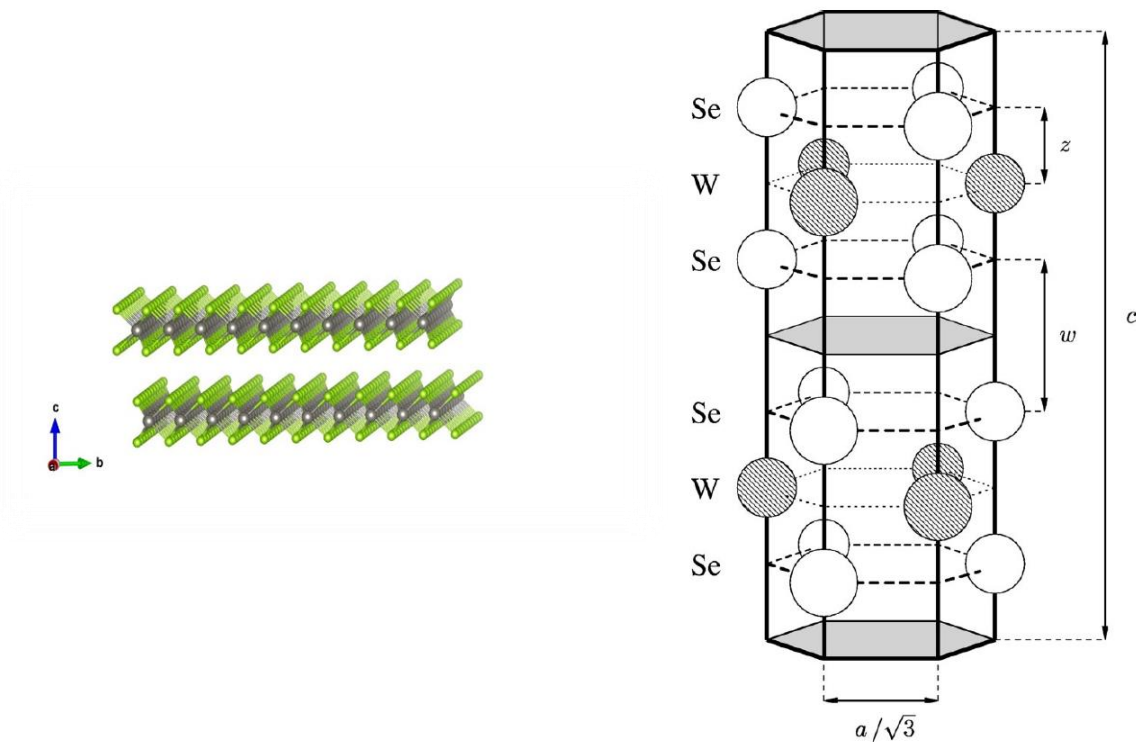


Figure 14. (a) Unit cell Crystal structure of WSe₂. (b) Top view 2H-WSe₂ displaying the hexagonal structure.

2.3.3.2. Properties and applications

The 2H variant of tungsten di-selenide (2H-WSe₂) is considered as a potential candidate among transition metal di-chalcogenides (TMDCs) in many applications such as chemical sensors, solar

cells, energy storage and photocatalysis [120–123]. Some of the recent works on WSe_2 layered structure show that this material is extensively used in applications, such as in building new generation sodium ions batteries (SIB). WSe_2 /carbon composite architecture has excellent performance as novel and efficient anode material in SIB owing to multilayer structure and large interlayer spacing that helps facilitating and further increase the intercalation of sodium ions [124,125]. WSe_2 has shown its capability as a suitable candidate for solar water splitting. Hybrid structure such as carbon nanotube/ WSe_2 exhibits superior performance in photodegradation of organic dye methyl orange [126,127]. High-performance flexible solar cells are also widely investigated using multiple layers of WSe_2 due to which high-power conversion efficiency is achieved. [128] Among all the widely researched TMDC, the 2H variant of tungsten di-selenide ($2H-WSe_2$) is a commonly known semiconductor that shows its ability towards detecting toxic gases such as NO_2 [114]. Previous reports by several groups demonstrate a p-type field-effect transistor (FET) based on mechanically exfoliated $2H-WSe_2$ monolayers for NO_2 detection where palladium (Pd) was used as source and drain electrodes to lower the contact resistance for hole injection [129]. Upon exposure to 0.05% of NO_2 , the source-drain current increased five orders of magnitude due to the decrease of the Schottky barrier and the increase of p-doping [129].

Further, in devices with a top-contact gate, the on-off ratio was also significantly improved after NO_2 exposure [129]. TMDC are also characterized by an abundance or absence of central chalcogen atoms, functioning as suitable coordination sites for specific heavy metal ions. For many of these reasons, as cited above, TMDC and WSe_2 , in particular, are now being considered promising sorbents towards detecting various harmful gases that cause serious health issues.

Conclusion

In this chapter, a detailed description of the investigated nanomaterials have been displayed, including their synthesis, classification and gas sensors applications. Afterward, the capability of MOX and TMDC nanomaterials as chemical sensors has been described further, giving the properties and advantages compared with other categories of materials. Specifically, this chapter described in detail the investigated semiconductor materials that have been targeted in this thesis: ZnO, α -Bi₂O₃ and 2H-WSe₂.

Chapter 3: Materials and methods

Introduction

Among different techniques that have been used to grow the nanomaterials, those based on the bottom-up approach have several advantages compared to top-down one. Among the bottom-up techniques, vapor phase growth has been widely utilized as an easy, scalable, cheap and effective technique to synthesize one-dimensional and two-dimensional nanomaterials including metal oxides and metal chalcogenides nanostructures. This chapter displays the techniques and the procedure that have been used to grow 1D ZnO nanostructures, α -Bi₂O₃ nanowires and WSe₂ nanosheets, as well as the characterization and device fabrication.

3.1. Synthesis techniques

3.1.1. Magnetron sputtering

Magnetron sputtering has been used in this work to deposit the metal catalysts assisting the growth of 1D metal oxides, such as for ZnO and α -Bi₂O₃ using Vapor Liquid Solid (VLS) mechanism. Moreover, it has been used to deposit metals and metal oxides nanoparticles for surface functionalization of 1D MOX structures. **Figure 15** shows the schematic of the sputtering plant made by Kenotec company (Italy). It is composed of two vacuum chambers: a big circular chamber (process chamber) for the deposition that can host four different targets materials, and a small tubular chamber (also called load-lock chamber) for the insertion and placement of the samples prior the deposition without breaking the vacuum in the process chamber. The two chambers are connected with a gate valve. A turbomolecular drag pumping station TMH 064 D E produces the vacuum in the load lock chamber, using an electronic drive unit. Instead, the vacuum is created in the process chamber using a rotative and turbomolecular pump. The first is Edwards Rotary vane pump RV12, with maximum displacement of 17 m³/h, maximum pumping speed of 14.2 m³/h and ultimate total pressure of around 10⁻³ mbar

<http://sensor.unibs.it/resources/fabrication>. In our magnetron sputtering system, the process chamber has an home position and can host four different positions for targets. Two of them are connected to the DC power supply and the others are connected to RF power supply (600W maximum power). The position of the sample holder is controlled by a step-by-step motor by the computer. The working principle of the sputtering process is based on the creation of a plasma of a gaseous discharge to bombard a target material. Due to this, target atoms are ejected and impinge on a substrate [130]. The deposition of the coating film can be controlled by tuning different parameters such as temperature (from RT to 600 °C), plasma composition (argon and oxygen coming from two lines in which the flux and the pressure are controlled by two Mass-flow controllers), the pressure inside the chamber and the electrical power applied. A custom Microsoft Access/Visual Basic software fully control the system.



Figure 15. Magnetron sputtering system.

3.1.2. Vapor phase growth

3.1.2.1. Vapor-Liquid-Solid (VLS) growth mechanism

In this work, metal oxides such as ZnO and α -Bi₂O₃ have been prepared using the Vapor Liquid Solid (VLS) mechanism. VLS is based essentially on the presence of a seed catalyst layer to assist the growth of 1D MOX nanostructures with the high control of the diameter and alignment of the 1D MOXs. However, another mechanism can also be exploited to grow 1D nanostructures. It is called Vapor Solid (VS) and excludes the need of catalyst seed. The VLS process used for each metal oxide will be explained in next chapters. The experimental set-up for metal oxides synthesis using VLS consists of a tubular alumina furnace able to reach the high temperatures (1500 °C) necessary to evaporate the metal oxide bulk powder (Figure 16). A pump controls the

vacuum inside the tube, while mass-flow controllers adjust the argon and oxygen flows that are used as carrier gases to ease the transportation of the material in the vapor phase. All parameters influencing the final synthesis, such as pressure in the tube, deposition time, evaporation temperature and the carrier flux are fully controlled by a custom LabVIEW Virtual Instruments (VI) in order to ensure the best reproducibility for the growth. In VLS growth mechanism, catalysts play a major role and behave as nucleation sites for MOX growth, controlling the diameters of the nanostructures. Inside the alumina tube, a crucible containing the MOX powder is positioned in the middle of the furnace and heated up at high temperatures keeping the pressure constant. After powder evaporation, the vapor is then transported using a carrier gas flow such as argon to a colder region, where another alumina holder, containing the target substrates covered by catalysts, is placed at low temperature for condensation. During the heating up of the furnace, the inert gas is flowed in the reverse direction (from the substrate to crucible containing powder) till reaching the desired temperature, to reduce the formation of nanostructures with undesired morphologies. Once reached the target temperature, the flow takes back to direct flow (from the crucible containing powder to the substrate).



Figure 16. Vapor-phase growth custom furnace

3.1.2.2. Atmospheric pressure chemical vapor deposition (APCVD)

CVD is a sophisticated tool for vapor transport and subsequent deposition of materials, with the unique ability to synthesize low dimensional nanostructures at acceptable lower temperatures and less harsh reaction conditions than traditional evaporation-condensation methods. Moreover, very high purity, multiple structures containing mono-layers, multi-layers and nano-composites with desirable characteristics can be prepared with this technique [131]. Recently, many variants of CVD have been developed including atmospheric pressure CVD (APCVD), modified metal-organic CVD (m-MOCVD), and low-pressure CVD (LPCVD) in addition to highly sophisticated deposition systems such as plasma enhanced CVD (PECVD). Among all the conventional deposition techniques, APCVD is very reliable and sustainable because it can be easily utilized for coating materials from gaseous precursors onto appropriate substrates. It has

been considered as the most promising medium for large-scale production of 2D materials with high-quality on several substrates [132,133].

APCVD conveniently implicates the catalytic activation of chemical reactions of gaseous reactant at the surface/interface of catalytic metal substrate in appropriate environment, such as seen in the case of graphene fabrication [134]. The steps required for the growth mechanism are described in detail in Figure 17 [134]. APCVD is essentially based on the formation of active gaseous reactants (precursors), transport of the reactants via carrier gas, adsorption of gaseous reactants onto the heated substrate, production of the film via heterogeneous reaction and desorption of the hazardous products. In addition, for the sake of comparison, while LPCVD has shown drawbacks in the synthesis of 2D materials as the final product is often non-uniform layers, APCVD showed a high control of large monolayer of graphene (for example), with less small multilayers on the top of the big mono layer. This is attributed to a diminished mean free path/diffusion coefficient of the reactants [135].

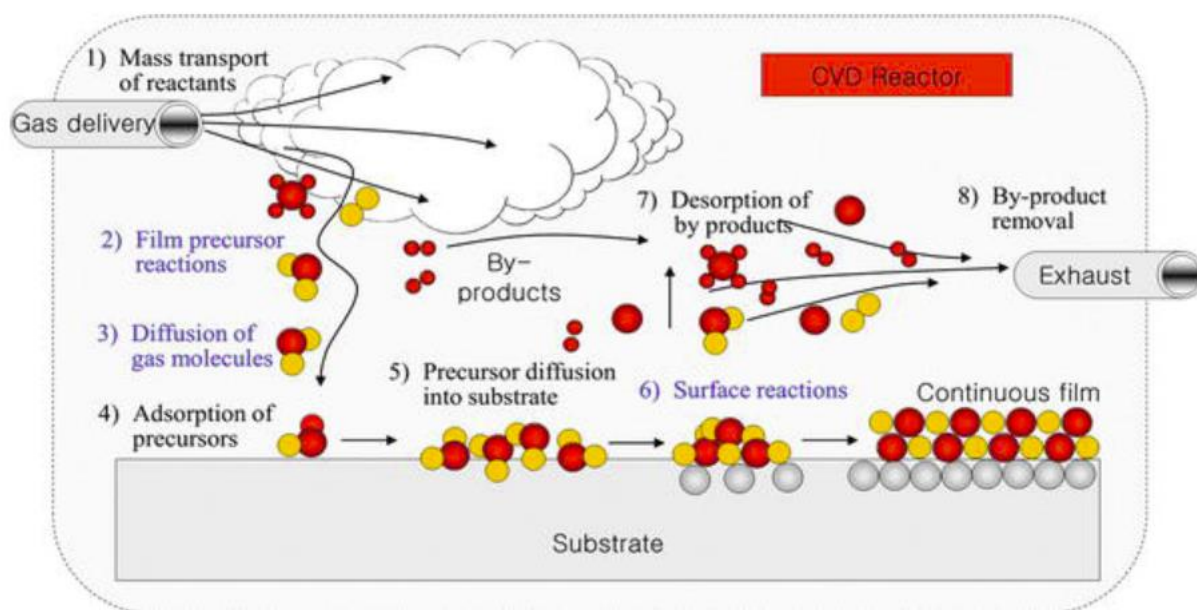


Figure 17. Transport and reaction mechanism of CVD technique.

In this thesis, atmospheric pressure chemical vapor deposition (APCVD) has been used to synthesize bulk layered 2D 2H-WSe₂ nanosheets. This technique was independently developed and scaled up by the laboratory of Prof. G.D. Nessim, Bar-Ilan University, Israel. Several works report the synthesis of WSe₂ by CVD using different precursors as starting materials such as WF₆, H₂Se, W(CO)₆, SeCl₄ [136]. Such precursors generate undesirable products (volatile by-products) from CVD reaction, which are hazardous to human health [137,138]. For this reason, the technique used in this collaboration starts with the evaporation of Se powder supported in argon as a carrier gas for transportation without the need of H₂, which provides a synthesis completely without the formation of hazardous products such as H₂Se.

The experimental setup consists of two furnaces (Figure 18): each one is controlled by a heater to maintain the high temperature (900 °C) needed 1) to evaporate the chalcogen (Se powder) precursor and 2) to activate the chemical reactions on the surface with the substrate (W foil). After evaporating the Se powder, the vapor containing Se is transported using Ar flow and deposited on the top of W foil to carry out the already mentioned reactions. However, some parameters

should be controlled and optimized to achieve good growth, such as Se precursor quantity, reaction time, acid etching, carrier gas flow. The method of synthesis of 2H-WSe₂ has been scaled up further by producing larger quantities of the bulk 2H-WSe₂ powder from the W foil in addition to studying various oxidation parameters on the bulk and exfoliated material, to understand the extent of its usability as a promising robust gas-sensor for NO₂ gas detection. The as-prepared material and its dispersion's stability is studied in detail in this thesis, providing new and exciting insights into the many different properties of this 2D layered material.



Figure 18. APCVD experimental setup.

3.2. Gas sensing setup

The conductometric sensor design is described in Figure 19. The design comprises an alumina substrate acting as support for the semiconductor nanomaterials, Pt electrodes to measure the electrical conductance, Pt heater to induce temperature for gas-surface reaction and pads to provide perfect adhesion between the different sensor elements and the substrate. Firstly, polycrystalline alumina (Al₂O₃) substrates (2mm × 2mm, 99.9% purity, Kyocera, Japan) with a thickness of 250 μm are ultrasonically cleaned for 20 min in acetone, rinsed by distilled water and then dried in pure air. TiW/Pt pads deposition was performed using DC-magnetron sputtering (DC-MS) (3 minutes, 300 °C, pressure 5×10⁻³ mbar, and 75W Ar plasma). The interdigitated Pt

electrodes (IPE) and Pt heater were deposited on top and backside of Al_2O_3 , respectively, utilizing DC-MS at the same conditions. The deposition time was 20 min. The final transducer was mounted on a transistor outline (TO) package using electro-soldered gold wires.

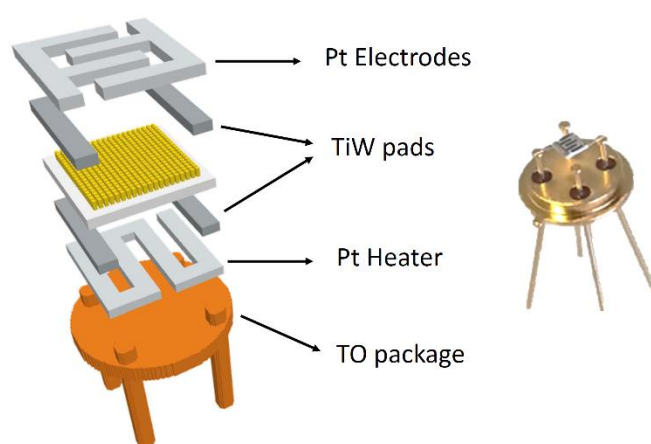


Figure 19. Schematic of conductometric device design.

For functional characterization in the presence of target chemical molecules, the sensors were placed inside a stainless-steel chamber (Angelantoni, Italy, model MTC 120) (Figure 20). This is because our system can host up to eight sensors simultaneously for performing the electrical measurements. The required analyte or gas concentration is obtained by mixing synthetic air with the correct amount of gas from a certified bottle (SOL, Italy). The total flow inside the chamber is fixed at hundreds sccm (in our case we used 200 sccm). The electrical conductance of the sensors is measured continuously by applying 1 V to 10 V (using an Agilent E3631A power supply) and recording the generated current using a picoammeter (Keithley 6485). The electrical behavior of sensors is investigated towards different chemical compounds, including reducing and oxidizing gases. For all measurements, each gas is injected for 30 min, and then a synthetic airflow is restored for 1 h to recover the conductance baseline. The relative humidity can be controlled and it varies from 0% (dry air) to 90%. The climatic chamber temperature is fixed at

20°C. Different working temperatures (generated and controlled by Thurlbly-Thandar PL330DP power supplies) can be applied, ranging from room temperature to 600 °C. Depending on the semiconducting nature of the sensitive material, the gas response is calculated using the formulas:

For n-type semiconductors such as ZnO:

$$\frac{G_{gas} - G_{air}}{G_{air}} = \frac{\Delta G}{G_{air}} \quad \text{For Reducing Gases} \quad \text{Eq 4}$$

$$\frac{G_{air} - G_{gas}}{G_{gas}} = \frac{\Delta G}{G_{gas}} \quad \text{For Oxidizing Gases} \quad \text{Eq 5}$$

For p-type semiconductors such α -Bi₂O₃ and 2H-WSe₂:

$$\frac{G_{gas} - G_{air}}{G_{air}} = \frac{\Delta G}{G_{air}} \quad \text{For oxidizing gases} \quad \text{Eq 6}$$

$$\frac{G_{air} - G_{gas}}{G_{gas}} = \frac{\Delta G}{G_{gas}} \quad \text{For reducing gases} \quad \text{Eq 7}$$

Where G_{air} and G_{gas} are the electrical conductances of semiconductor in the air (conductance baseline) and gas, respectively.

Matlab software (Mathworks Inc, US) has been used to calculate the response values as well as the response and recovery times.

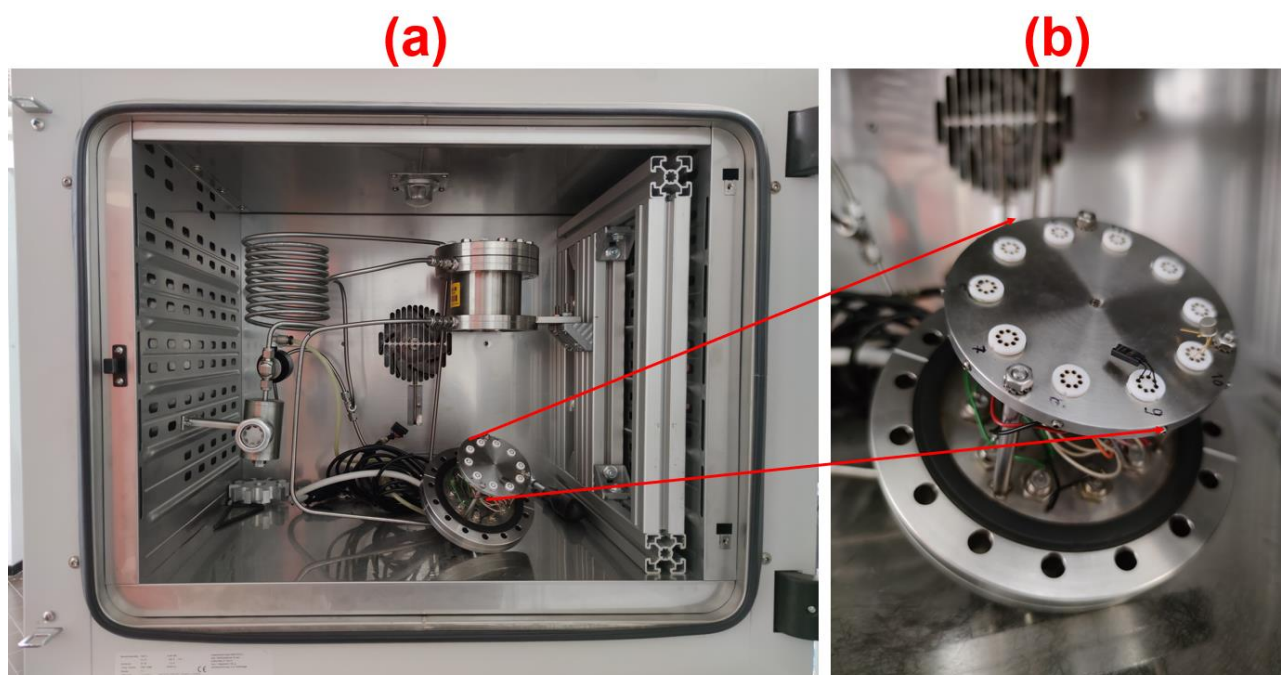


Figure 20. (a) home-made stainless-steel chamber for gas testing. (b) holder of the sensors (can host up to 10 sensors).

3.3. Synthesis of one dimensional ZnO nanostructures

3.3.1. Material preparation

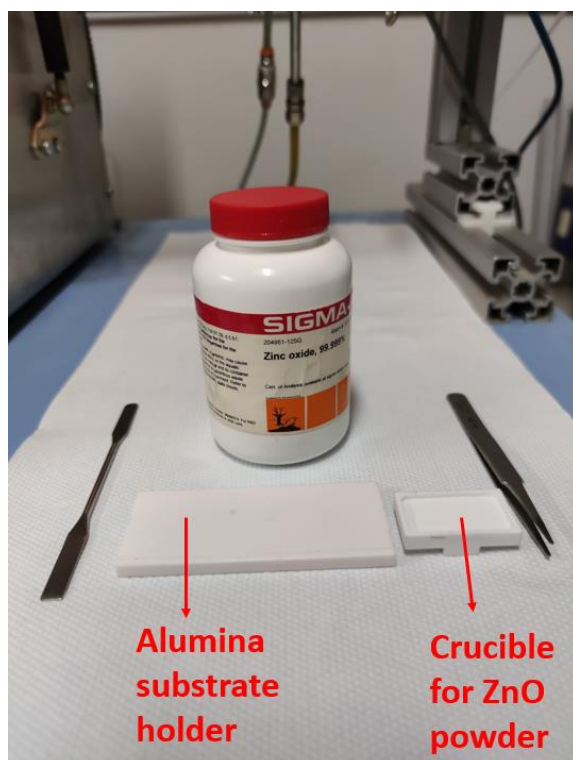


Figure 21. holders and ZnO powder required to perform the vapor phase growth of one dimensional ZnO.

Alumina (99.9% purity, 2 mm × 2 mm, Kyocera, Japan) and silicon substrates were used as support for growing 1D ZnO nanostructures. Alumina was used for the fabrication of chemical sensors, whereas silicon was used for material characterization. Prior the deposition, samples were ultrasonically cleaned in acetone solvent for 15 minutes and then dried in synthetic air to remove any dust or contamination. Magnetron sputtering was used to catalyze the substrates, coating them with ultrathin films of gold, platinum, silver and copper (Au, Pt, Ag, Cu) with thickness values between 2 and 7 nm, according to the experimental conditions reported in Table 6. To the best of our knowledge, this research activity is the first study reporting the use of Cu as a catalyst for the

synthesis of ZnO nanowires. Instead, Ag was used in few previous works [139,140], but the achieved NWs were not exploited for chemical sensing applications. In VLS growth mechanism, catalysts play a major role and behave as nucleation sites for ZnO growth, controlling the diameters of the nanostructures and may enhance the sensing performances.

To synthesize the nanostructures, ZnO powder (99.9% purity, Sigma Aldrich) (Figure 21) was placed in the middle of the alumina tube and heated at 1200 °C, keeping the pressure at 10 mbar to induce the powder evaporation. The ZnO vapor is then transported to a colder region of the furnace using a carrier gas flow (argon, 75 sccm) where it condenses on the substrates covered by catalysts. The deposition process was kept for 15 minutes. Each catalyst used for the 1D ZnO growth is active at a specific temperature, i.e. Au (500 °C and 600 °C) Pt (600 °C), Ag (350 °C) and Cu (400 °C), confirming the temperature role in supersaturation and growth of 1D ZnO nanostructures.

Table 6. Experimental parameters used in magnetron sputtering system for catalyst seed deposition.

Catalyst	Ar flow (SCCM)	Pressure (10⁻³ mbar)	Magnetron Power (W)	Deposition time (s)
Gold (Au)	7	5	75	5
Platinum (Pt)	7	5	75	2
Silver (Ag)	7	5	50	5
Cooper (Cu)	7	5	50	15

3.3.2. Material characterization

The structural properties of ZnO samples were extracted using X-Ray Diffractometer (Empyrean; PANalytical, The Netherlands) with Cu-LFF ($\lambda = 1.54 \text{ \AA}$) tube operated at 40kV-40mA. Morphological analysis was investigated using Field Scanning Electron Microscopy (LEO 1525 model; Carl Zeiss AG, Oberkochen, Germany) operated at 10 KV and Transmission Electron Microscopy (TEM) 200CX (JEOL, Japan).

For the electrical characterization, the conductometric chemical sensors have been prepared using the process previously described, by depositing a heater and electrical contacts on the substrates with the sensing material (ZnO), as shown in Figure 22.

The gas sensing tests were performed inside a stainless-steel chamber at the fixed temperature of 20 °C. Several gases such as hydrogen, CO, ethanol and acetone were tested at 50 % relative humidity. The concentration (in ppm) of each gas was achieved by mixing the gas with synthetic air. The flow was fixed at 200 sccm and the electrical conductance was measured applying 1 V. The samples were tested at different working temperature ranging from 200 °C to 500 °C. Three different samples were prepared for each catalyst in the same conditions. The presented results are the average of the measurements performed on all devices.

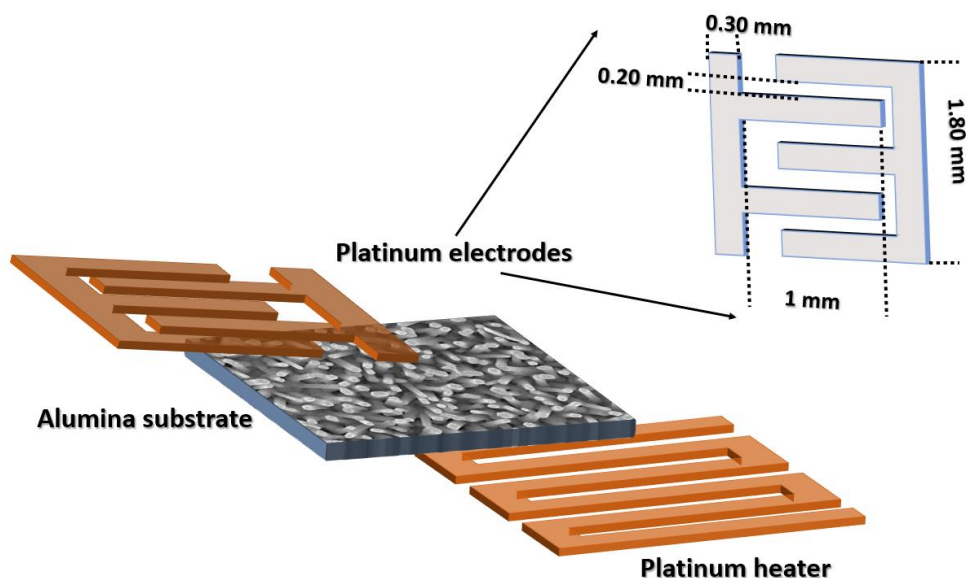


Figure 22. Design of conductometric sensor device.

3.4. Synthesis of α -Bi₂O₃ nanowires

3.4.1. Material preparation

Crystalline α -Bi₂O₃ nanowires were prepared via evaporation method using VLS mechanism. Firstly, alumina substrates (2 × 2 mm, 99.9% purity, Kyocera, Japan) were used as support for α -Bi₂O₃ growth and were ultrasonically cleaned in acetone solvent and rinsed in distilled water. Platinum, copper and gold thin layers of about 7 nm were deposited using magnetron sputtering at room temperature on the top side of Al₂O₃ substrates. Bi₂O₃ powder (99.9 %, Sigma Aldrich) was positioned on an alumina crucible inside the furnace and heated up at high temperatures of about 1000 °C at 10 mbar (Figure 23). Once Bi₂O₃ starts evaporating, it is transported thanks to an argon flow (75 SCCM) and then it condenses on the top of the substrate starting the formation of the nanowires. Bi₂O₃ vapor interacts with catalyst clusters formed from the catalyst layer during the heating step. 550 °C is the optimal temperature that ensures the diffusion of bismuth oxide into the catalyst droplet for the segregation and nanowires formation. This temperature is necessary to activate the nucleation phenomena, diffusion and nanowires crystallization.

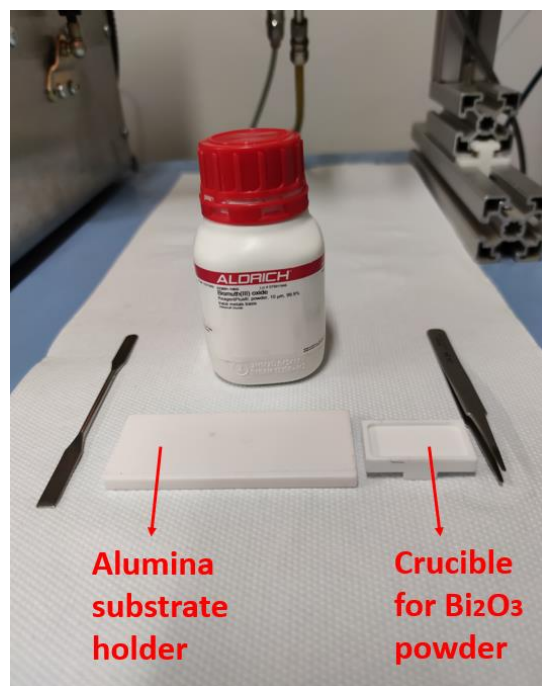


Figure 23. Holders and Bi_2O_3 powder required to perform the vapor phase growth of $\alpha\text{-Bi}_2\text{O}_3$ nanowires.

3.4.2. Synthesis of $\alpha\text{-Bi}_2\text{O}_3$ functionalized with nanoparticles

Prior the deposition of the nanoparticles on the surface of $\alpha\text{-Bi}_2\text{O}_3$ nanowires, these nanoparticles have been prepared separately. Films of Au, Ag and Ti have been deposited on Alumina substrates using magnetron sputtering respecting the conditions listed in **Table 2**. Then, a thermal annealing treatment in the air has been carried out. Note that the thickness of metals, annealing temperature and annealing time have been optimized to get a high quality of metal and metal oxide nanoparticles. The best conditions are shown in **table 7**. Secondly, the nanoparticles have been deposited on the surface of $\alpha\text{-Bi}_2\text{O}_3$ nanowires. The conditions of preparation of the metal and metal oxides nanoparticles have been kept constant when decorating the pristine $\alpha\text{-Bi}_2\text{O}_3$ nanowires. Many samples of nanoparticles functionalized $\alpha\text{-Bi}_2\text{O}_3$ such as $\text{Au-}\alpha\text{-Bi}_2\text{O}_3$, $\text{TiO}_2\text{-}\alpha\text{-Bi}_2\text{O}_3$ and $\text{Ag-}\alpha\text{-Bi}_2\text{O}_3$ have been synthesized to study the enhancement of the chemical response due to the presence of nanoparticles over the pristine material.

Table 7. The experimental parameters to synthesis nanoparticles.

Clusters	Ar flow (SCCM)	Pressure (10^{-3} mbar)	Magnetron power (W)	Deposition time	Thickness (nm)	Annealing temperature ($^{\circ}$ C)	Annealing time (h)
Au	7	5	75	5s	7	500	2
Ti	7	5	75	4 min 7s	15	500	2
Ag	7	5	50	5s	7	400	1

3.4.3. Material characterization

The synthesized α -Bi₂O₃ nanowires were analysed using several techniques; the samples morphology was investigated using Field Scanning Electron Microscopy (LEO 1525 Gemini model; Carl Zeiss AG, Oberkochen, Germany) operated at 10 KV and coupled with an INCAx-act (Oxford, UK) EDX detector. The structural properties were extracted using X-Ray Diffractometer (Empyrean diffractometer; PANalytical (Cu-LFF ($\lambda = 1.54 \text{ \AA}$) tube operated at 40 kV- 40 mA)).

For electrical characterization, the same conductometric design has been used as in the case of ZnO sensor. However, we have chosen low acetone and ethanol concentrations (minimum 2 ppm of acetone and 10 ppm of ethanol) varying the relative humidity from 50 to 90 %, realizing an environment as close as possible to breath to study the suitability of α -Bi₂O₃ sensors for breath analyser. Other gases have been tested such as hydrogen, ammonia, NO₂, CO, CO₂ and O₂ to study the selectivity of the sensors. The applied voltage was 10 V. This voltage is applied in order to measure an appreciable current and get a stable baseline due to the high electrical resistance of the α -Bi₂O₃ devices. In fact, sensors have shown a good long-term stability, even after tests with many different gases at several temperatures and

at relative high humidity level. The samples were tested at different working temperature ranging from 250 °C to 400 °C.

3.5. Synthesis of 2H-WSe₂ nanosheets

3.5.1. Material preparation

The synthetic procedure of growing bulk 2H-WSe₂ on W foil using elemental Se (Alfa Aesar, 99.999 % purity) and W foil (Alfa Aesar, 99.999% purity) in an ambient pressure chemical vapor deposition-assisted process has been achieved. We prepared the pristine W foil after etching it in dilute hydrochloric acid (0.01 M) and sonicating it in isopropanol (for removing the native oxide layer on the exposed W foil's surface). The W foil was introduced into the furnace (F2) at 900 °C. Then, the elemental Se was introduced into the furnace (F1) at 650°C in order to initiate the WSe₂ formation in the W foil surface. In our experiment, we observed that the reaction between the W foil and the elemental Se occurs (in the absence of pressure) at 900 °C (no reaction has taken place between 600 and 850 °C) in F2 while heating the elemental Se precursor at 650 °C in F1. All the experiments were done in Ar atmosphere in the absence of hydrogen (for eliminating the possibility of H₂Se formation). The bulk 2H-WSe₂ formed on the W foil surface was characterized and then was exfoliated into nanosheets following exfoliation in ethanol as a solvent. This 2H-WSe₂ dispersion was utilized for the gas sensing measurements (by modulating the total number of drops of this dispersion). The air-annealing of 2H-WSe₂ is done from 50 °C to 200 °C to observe microstructural changes and changes in the original phase (which determines the stability of the material in ambient and elevated temperatures in the absence of inert atmosphere). The exfoliation parameters for obtaining the 2H-WSe₂ powder from the bulk 2H-WSe₂ grown on W foil were optimized and checked for further stability in the resulting dispersions. The exfoliation times are checked thoroughly to obtain the best quality flakes, and the stability and homogeneity of resulting dispersions were also checked.

3.5.2. Material characterization

X-ray diffraction measurements of bulk tungsten di-selenide (WSe_2) on tungsten (W) foil were performed using a Bruker D8 advanced diffractometer. We analyzed a 2 cm x 2 cm square sample of bulk tungsten di-selenide (WSe_2). The data was collected in the 2θ range from 10° to 80° , with a step size of 0.002° and scanning rate of $0.4^\circ/\text{min}$. The X-ray generator is operated at 40 kV and 30 mA with Cu $K\alpha$ radiation ($\lambda = 1.542 \text{ \AA}$). The bulk tungsten di-selenide (WSe_2) on tungsten (W) foil is further analyzed by X'pert HighScore Plus software to ensure that the product obtained is from a highly repeatable procedure as well as to confirm the effects of air annealing on the material starting from 50°C to 200°C . Similar High-Resolution Scanning Electron Microscopy (HRSEM) of the bulk material and air-annealed material is done using the instrument Magellan 400 FEI. Additional analyses with Atomic Force Microscopy (A.F.M.) measurements were performed. This measurement was done in a Bio Fast Scan scanning probe microscope (Bruker A.X.S.). For image processing, Gwyddion software is used. The "flattening" and "plane fit" functions are also directly applied to each image. Further, HRTEM analysis of the exfoliated WSe_2 sample was carried out in a JEM 2100, JEOL (operating at 200 keV). The T.E.M. images are analysed using Gatan digital Micrograph. X-ray Photoelectron Spectroscopy (XPS) measurements are performed using the Thermo Scientific Nexsa spectrometer. The samples were irradiated with a soft X-ray source ($\sim 1.5 \text{ KeV}$) under Ultra High Vacuum conditions ($\sim 10^{-10}$ - 10^{-9} torr), and their ejected photoelectrons were analyzed.

3.5.3. 2H- WSe_2 device integration

After synthesizing bulk 2H- WSe_2 using AP-CVD on the tungsten (W) foil, a 2H- WSe_2 suspension was prepared by scratching and dispersing a fixed amount of material into 20 ml of ethanol. A properly dispersed 2H- WSe_2 solution was obtained by ultra-sonication of the solution for 8 hours

(with 1h break in between) at maximum power and a high frequency of 59 kHz at room temperature. The dispersion containing 2H-WSe₂ nanosheets was drop-cast on the top of IPE to fabricate the conductometric device, as shown in Figure 24. Three 2H-WSe₂ sensor batches with different droplets number of 2H-WSe₂ (corresponding to a different number of layers) were fabricated herein and labeled as WSe₂ (2D), WSe₂ (8D), and WSe₂ (12D) corresponding to two, eight, and twelve droplets, respectively. All sensors are stabilized by heating them at 150 °C using a power supply for 3 days (72 hours) after device production and before the gas testing. It is important to note that after each drop, devices were kept for 20 min in the hood for the complete evaporation of the solvent. The volume of a drop of the liquid dispersion is equal (approximately) 0.045 cm³.

The electrical conductance of the sensors is measured continuously by applying 1 V. The electrical behavior of sensors is investigated towards different chemical compounds, including reducing (NH₃, H₂S, acetone, H₂) and oxidizing (NO₂) ones. The relative humidity is fixed at 20% at 20°C, and different working temperatures were also additionally investigated, ranging from room temperature (R.T.) to 150 °C.

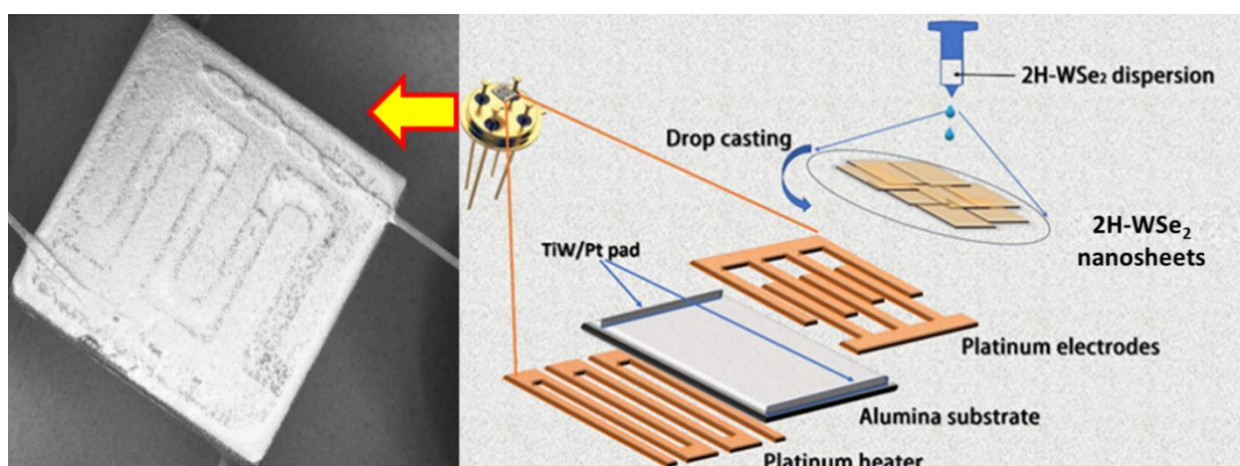


Figure 24. The design of the conductometric sensor and drop-casting fabrication of the 2H-WSe₂ nanosheets sensor.

Conclusion

In this chapter, the instrumentations used and the methodologies performed during the experiments have been described in detail. VLS mechanism has been used to grow 1D ZnO nanostructures and α -Bi₂O₃ nanowires, while APCVD has been used to grow 2D WSe₂, followed by liquid-phase exfoliation and drop-casting onto the transducer. Moreover, the general mechanisms of the growth of these nanostructures have been explained.

Chapter 4. 1D ZnO nanostructures for chemical sensors applications

Introduction

Despite one-dimensional (1D) metal oxide nanostructures, such as nanowires and nanorods, are attracting new possibilities and offering several characteristics for the fabrication of various sensing devices, the control of the growth of these nanomaterials is a hot topic for the scientific committee in the field of material science, In this chapter, 1D ZnO nanostructures are grown using VLS mechanism assisted by several catalysts, and the effect of a catalyst in controlling the growth mechanism is studied, displaying and investigating the sensing results of the these nanostructures.

4.1. Effect of catalysts on the morphology of 1D-ZnO

In this research, the control over the form, shape and morphology of 1D ZnO nanostructure was explained by two mechanisms: catalysts composition and thermodynamic conditions. Each catalyst is active for nanostructure formation at specific temperatures, depending on its specific melting point. Liquid droplets formation and supersaturation are crucial parameters for controlling the nanostructures morphology and explaining the different shapes obtained. In general, the mechanism leading the formation of 1D ZnO structures is based on the nucleation, diffusion and crystallization phenomena [141]. The temperature plays a crucial role in VLS mechanism. Firstly, atoms in the ZnO vapor adsorb on the substrate surface. The substrates were heated from 350 °C to 600 °C for 15 minutes during the deposition, increasing the energy of these atoms and thus enhancing their ability to diffuse onto the substrate surface. Due to the treatment at high temperature, the catalyst particles aggregates forming liquid clusters and promoting the condensation of ZnO vapor. The ZnO vapor molecules reach the droplet catalyst surface and are incorporated as adatoms. The adatoms diffuse into the cluster and, as the supersaturation of the droplet occurs, the segregation will start forming 1 D nanostructures.

Figure 25 shows ZnO nanostructures grown using Au, Pt, Ag and Cu catalysts and their respective size distribution. While the length of all samples is tabulated in Table 8. The NWs obtained using Ag catalysts are dense and homogeneous, covering completely the alumina substrate with an average diameter around 46 nm with a 400 nm length. ZnO NWs obtained using Cu catalyst are quite different in morphology: a kind of ductility of the NWs was observed, with low density. Despite that, on average they are 4 micrometres long and 42 nm in diameter. A good density of small nanowires (≈ 38 nm diameter and ≈ 1000 nm length) was achieved with Pt catalyst. ZnO NWs were obtained with Au catalyst at low temperatures with a high aspect ratio and density (≈ 25 nm diameter and ≈ 1000 nm length). On the other hand, high temperature promotes nanorods formation, which may be explained by the high diffusion of ZnO vapor affecting the supersaturation of ZnO and leading to the formation of ZnO NRs with high quality. The catalyst NPs size controls the diameter of crystallized NRs (≈ 84 nm diameter and ≈ 600 nm length). The morphology transition from NWs to NRs (Figure 26(c) and Figure 26(d) can be also explained by coalescence effect of the catalyst seeds. The final products consist of NPs with different size as shown in Figure 26(a) and Figure 26(b).

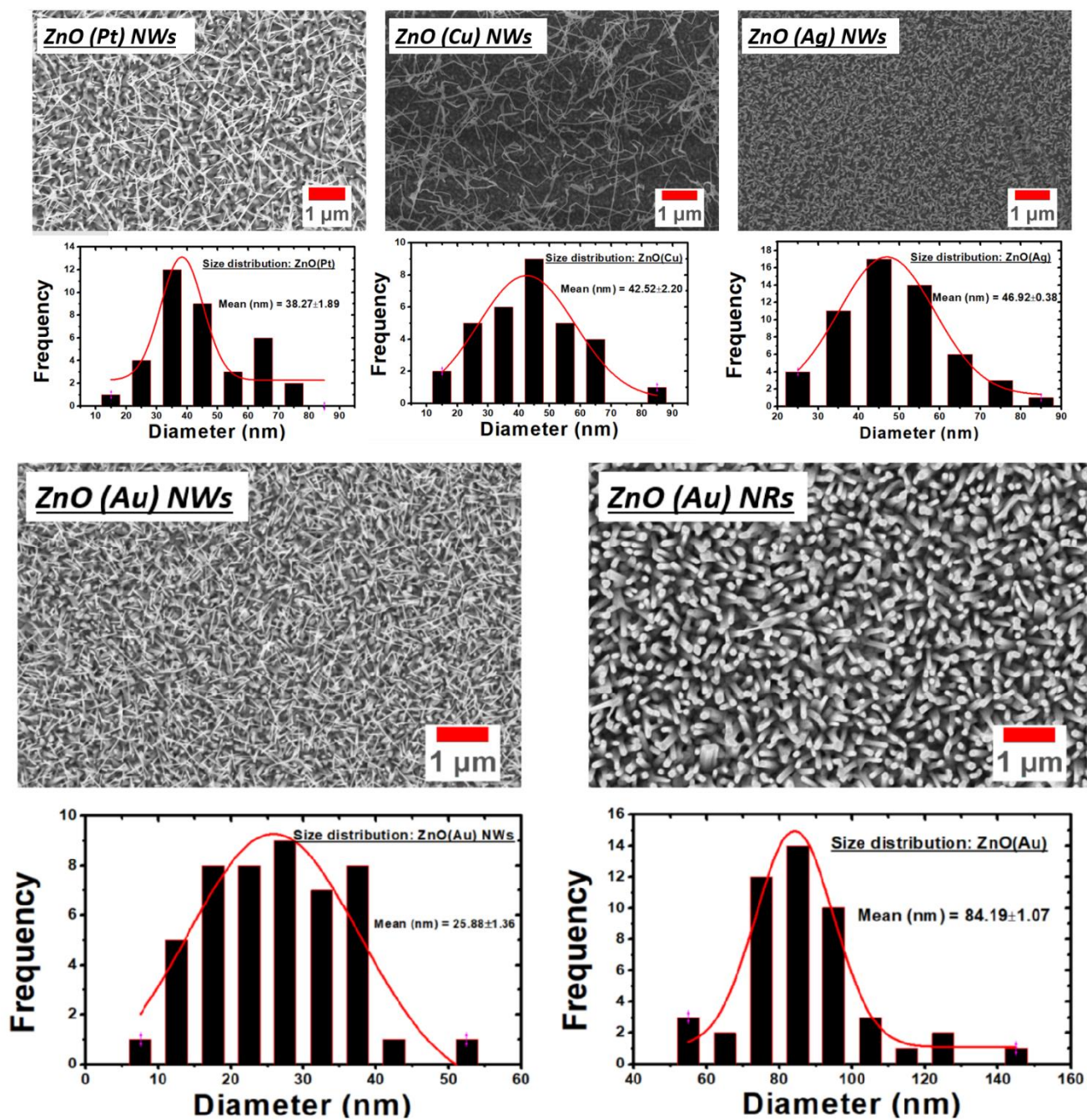


Figure 25. 1D ZnO nanostructures using Au, Pt, Ag and Cu catalysts and its size distribution.

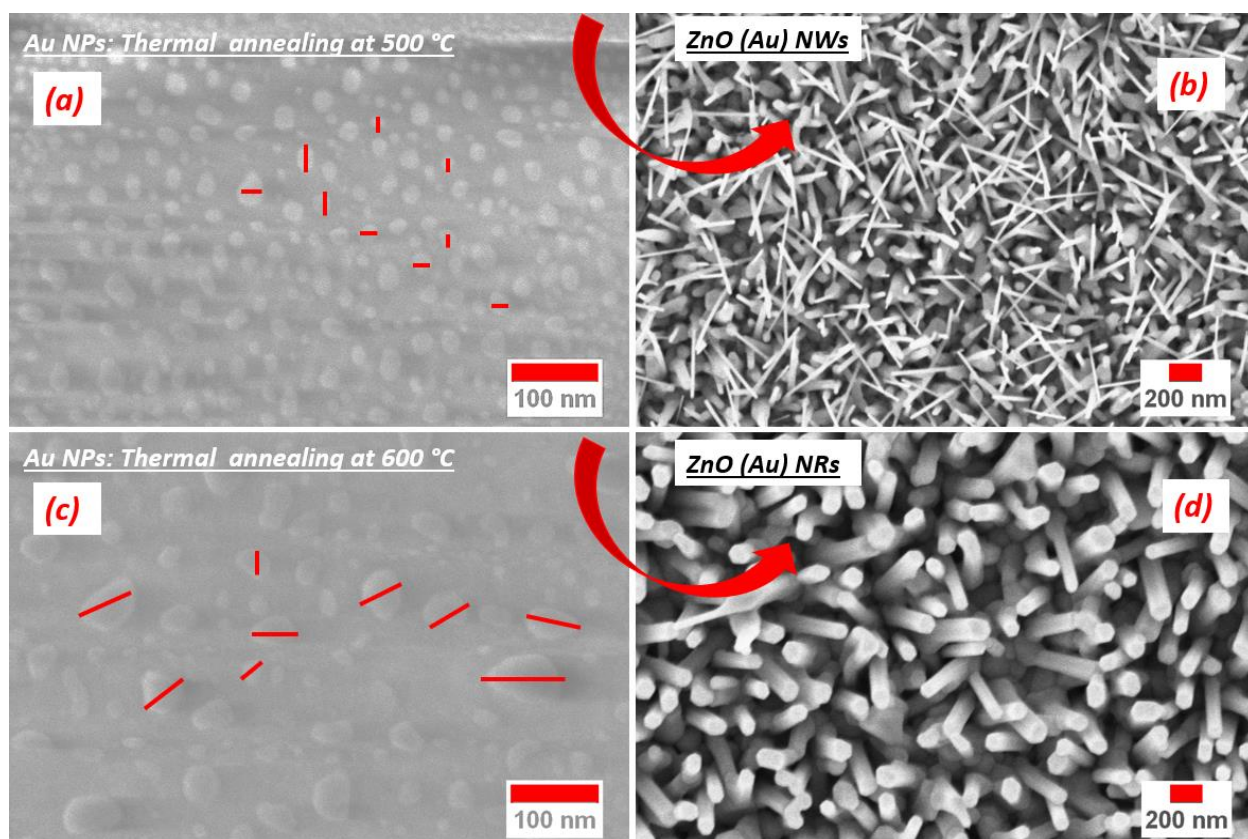


Figure 26. Au seed layer annealed at 500 °C (a) and 600 °C (c) without nano- (wire/rod) growth; High magnification ZnO nanowires (b) and ZnO nanorods (d) after growth.

4.2. Structural properties of ZnO nanostructures

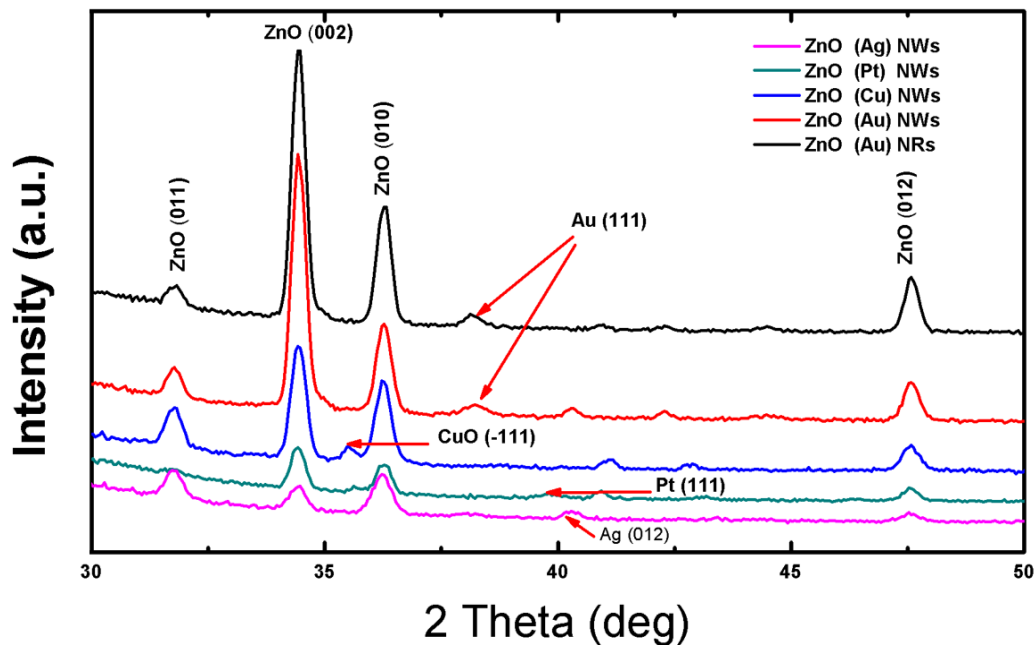


Figure 27. X-ray diffraction patterns of 1D ZnO synthesized using various catalysts.

Figure 27 depicts the X-ray diffraction patterns of 1D ZnO synthesized using various catalysts. All peaks observed for the different ZnO nanostructures agree with standard ZnO (JCPDS 80-1916). The (011) (002) (010) and (012) peaks situated at 31.7° , 34.4° , 36.3° and 47.5° , respectively, show the formation of ZnO crystal belonging to hexagonal structure. The catalysts particles appear in their metallic or oxidized form, depending on the material. The appearance of gold (JCPDS no. b96-901-1614), platinum (JCPDS no. 98-002-1997) and silver (JCPDS no. 98-002-1958) in metallic form is confirmed by their peaks situated at 38.24° , 39.84° and 40.17° , respectively. They remain stable during the deposition even under pressure and high temperature. On the contrary, copper was oxidized into CuO (JCPDS no. 94-003-8482), as

demonstrated by the peak situated at 35.56°. This was expected, considering the low chemical stability of copper. Similar results were observed by Zhang et al.[139], who studied the stability of catalysts nanoparticles before and after NWs growth. They confirmed the chemical stability of platinum and gold, while they observed and discussed the Ag oxidation to AgO, and the formation of Ag₄SiO₄ in case of silicon substrate. The crystallite size (D) was calculated (Table 8) using Debye Scherrer formula defined as $(D = (0.94 \lambda) / (FWHM \cos\theta))$, where FWHM is the full width at half-maximum of an (hkl) peak at θ value, θ is the half of the scattering angle and λ is X-Ray wavelength equals 0.154 nm. The crystallite size is 21.83 nm and 22.06 for ZnO (Au) NWs and NRs, respectively, which are smaller than the crystallite size of ZnO (Cu) NWs (D = 23.81 nm) ZnO (Pt) NWs (D =30.07 nm) and ZnO (Ag) NWs (D =30.15 nm).

Table 8. FWHM, Crystallite size and the length of the 1D ZnO nanostructures using different catalysts.

Sample	2 θ (degree)	FWHM (degree)	Crystallite size (nm)	ZnO length (nm)
ZnO (Au) NWs	34.42	0.398	21.83	1000
ZnO (Au) NRs	34.44	0.394	22.06	600
ZnO (Pt) NWs	34.40	0.289	30.07	1000
ZnO (Ag) NWs	34.43	0.279	31.15	400
ZnO (Cu) NWs	34.43	0.365	23.81	4000

The catalysts affect not only the shape and the morphology of the nanostructure, but also play a major role on the preferred orientation of crystallites. In this context, the texture coefficients of ZnO nanostructures were calculated using the equation below.

$$TC(hkl) = \frac{I(hkl)}{I_0(hkl)} \left(\frac{1}{n} \sum_{i=1}^n \frac{I(hkl)}{I_0(hkl)} \right) \quad \text{Eq 8}$$

Where (hkl) are Miller indices denotes the X-ray diffraction direction plan, $I(hkl)$ is the intensity of CuO measured, $I_0(hkl)$ is the standard intensity taken from the (JCPDS 80-1916) and n is reflection number. Using the texture coefficient, the preferred orientation of crystallites could be established. The texture coefficient values of 1D ZnO nanostructures using different catalysts are tabulated in Table 9. The diffraction peak (hkl) with TC that comprises values between zero and one defines a lack in crystallites orientation hkl. While, when the TC value exceeds one ($TC > 1$), there is a majority of crystallites orientation in (hkl) direction. ZnO (Au) nanowires and nanorods, ZnO (Pt) nanowires and ZnO (Cu) nanowires polycrystalline structure have (002) as preferred orientation. ZnO (Au) NWs samples possess the highest TC (2.18). These results show that the diffraction peak (002) is not only the most intense peak, but also the crystallites preferential direction. As a result, (002) is the predominant orientation. On the contrary, in ZnO (Ag) nanowires (010) and (002) are both considered as preferential direction of due to their almost identical TC values.

Table 9. The texture coefficient values of 1D ZnO nanostructures using different catalysts.

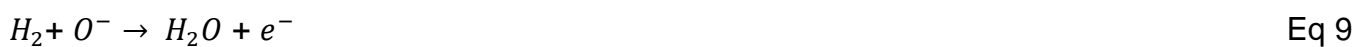
Sample	Diffraction peaks		
	(010)	(002)	(011)
ZnO (Au) NWs	0.41	2.18	0.39
ZnO (Au) NRs	0.67	1.78	0.53
ZnO (Pt) NWs	0.80	1.53	-----
ZnO (Ag) NWs	1.18	1.17	0.64
ZnO (Cu) NWs	0.75	1.67	0.57

4.3. Conductometric sensing: hydrogen (H₂) detection

4.3.1. Working Principle

Despite the simplicity of conductometric sensors design, the gas detection mechanism remains complex and not fully understood. The gas/MOX surface reactions, that transduce the chemical signal into an electrical one, are shortly described hereby. Oxygen is the main reaction precursor involved in conductometric sensors. As air interacts with ZnO (Figure 28 (a)), oxygen atoms adsorb onto its surface [142]. Oxygen adsorption in oxide semiconductor materials involves a carrier charge exchange. Oxygen starts with physical adsorption at low temperatures and ends with ionic adsorption (chemisorption), yielding in the final step an anion oxygen (O^-) at high temperatures as explained by chapter 1 [76,143]. The interaction with oxygen molecules (in air) leads to a change of the electrical conductance caused by electrons transfer from the semiconductor to oxygen ionosorbed due to its high electronic affinity.

During gas injection, various possible scenarios may occur, depending on the semiconducting behavior of the material (n- or p-), the injected gases nature (reducing or oxidizing), electronic affinity, ionization energy and others. When a target gas is injected, electrons exchange according to different processes. In the present work, H₂ and the other tested gases are reducing compounds. As shown in Figure 29 (b), hydrogen molecules react with the adsorbed oxygen to form water molecules, as described by the equations (9) and (10) [144]. Thanks to their small ionization energy, reducing gases behave as electrons-donors. The released electrons generated by the reaction between the reducing gases and the adsorbed oxygen cause a decrease of the thickness of the depletion region (region free of electrons) at the surface of ZnO. As a result the electrical conductance of the sensor increases [143].



Moreover, in specific thermodynamic conditions, hydrogen as a reducing gas is sometimes able to remove oxygen from the ZnO crystal, creating oxygen vacancies that play a crucial role in gas sensing mechanism (equation (11) [145]). However, a fraction of oxygen vacancies formed can ionize and release one or two electrons, enhancing the electrical conduction, as explained by equations (12) and (13).

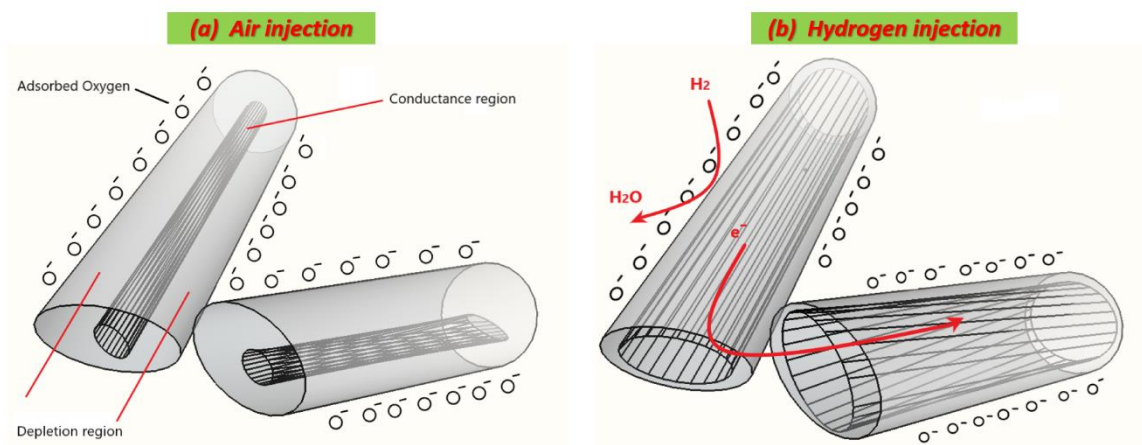


Figure 28. Hydrogen-sensing mechanism model of one dimensional (1D) sensor: (a) charge transfer and air injection; (b) sensing model toward hydrogen.

4.3.2. Catalyst effect on sensing characteristics

Despite the high quality of 1D nanostructures produced by VLS, there is a lack of understanding of the catalyst's role especially on the functional properties. Researchers are trying to explain how the catalysts presence controls the VLS growth, making hypothesis about its distribution along

NWs/NRs during VLS mechanism. It may act as a doping agent, as reported by Chen et al. who have considered the catalysts as additives or contamination explaining its substitution within the crystal [146]. These catalysts particles may be distributed around/decorating the NWs sidewalls, as reported by Hannon et al. who have explained in detail the migration (by diffusion) of the catalyst particles from droplets to the sidewalls until the NWs growth is completely terminated [147]. In all cases, the catalyst has a crucial role in enhancing conductometric sensors characteristics. In the present work, we have analysed all the possibilities, thanks to TEM mapping of ZnO grown by gold catalysts illustrated in Figure 29 and SEM image in the inset of Figure 30 (b). Au is decorating ZnO and the sensing response can be enhanced based on chemical sensitization as described in Figure 30. Gold distribution around the NWs improves gas sensing via spill-over effect, by dissociating gas molecules and activating the chemical reaction on the MOX surface [148]. Gold and in general noble metals provide active sites for chemical adsorption, such as O₂ adsorption (Figure 30 (a)). At the same time, H₂ is dissociated into fragments (atomic H) at specific temperature, and spills over ZnO surface to interact with pre-adsorbed oxygen, creating H₂O and therefore releasing electron back to ZnO, affecting its conductance (Figure 30 (b)). Most important, spill-over effect occurs without transferring electrons from gold to ZnO. Same principle may occur for Pt and Ag, even if the latter may oxidize during the gas testing at higher temperatures. Cu interaction with the gas phase, on the contrary, may be described by electronic sensitization due to the formation of stable oxide CuO. More discussions about electronic sensitization are found in literature [149]. Moreover, spill-over effect does not change the gas sensing mechanism, enhancing only the rate of the chemical interaction processes.

On the other hand, many reports investigated the metallic cluster decoration which can be highly beneficial for chemical sensors applications. Furthermore, bimetallic clusters have been found to be even more effective than monometallic clusters. In this context, Bahariqushchi et al. investigated

free carrier enhanced depletion in ZnO nanorods decorated with bimetallic AuPt nanoclusters [150]. In comparison with ZnO NRs, the mono- and bi-metallic decorated ZnO showed high sensitivity. This is due to the increase of depletion of free carriers because the bimetallic effect occurs an enhancement of gas adsorption, and provokes a stronger electron spill-over from the ZnO surface to the bimetallic nanoclusters.

Chen et al. investigated Au/Pd-NPs decorated ZnO nanowires for NO₂ sensor [151]. Indeed, the enhanced sensing performances towards NO₂ are attributed to oxygen vacancies that have been increased in Au/Pd@ZnO sample as well as the chemical sensitization that provides more active sites for NO₂ adsorption.

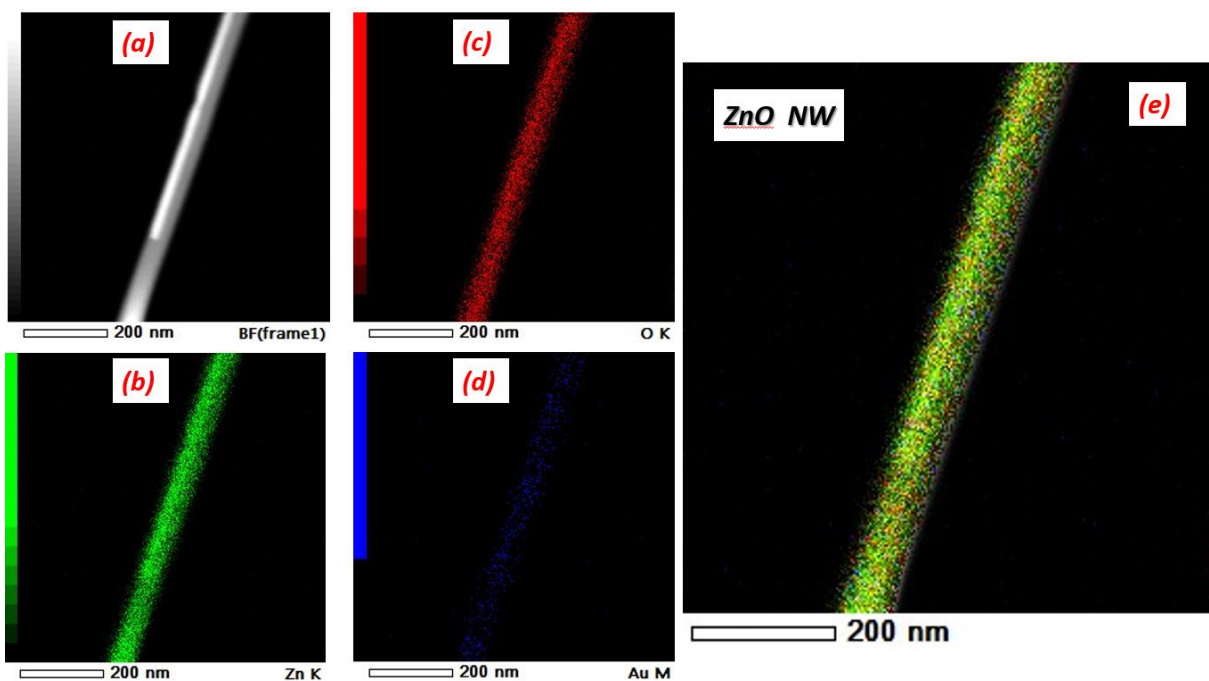


Figure 29. (a) shows ZnO nanowire TEM image. TEM-EDS elemental mapping image of; (b) Zn, (c) O, (d) Au and (e) represents the EDS mapping of single ZnO nanowire.

As mentioned before, the incorporation of gold into nanowires cannot be excluded, especially considering the solubility of Au in ZnO that may be achieved in specific conditions such as deposition at high pressure and temperatures, annealing at high temperature and gold content [152,153]. However, the solubility and the chemical state of ZnO (Au) are still not clear according to the few reports in literature [153]. In some cases, it could form a ternary alloy, if additive exceeds specific concentration (not expected in the present work). Instead, at low concentrations of additives, it may be a substitute in the host materials, affecting the charge carrier transfer. The impact on sensing properties is justified by the Fermi level shift due to the existence of deep donor levels within ZnO band gap energy, which can enhance the density of ionized oxygen in ZnO surface, reinforcing the reaction with reducing gases and affecting the charge depletion layer.

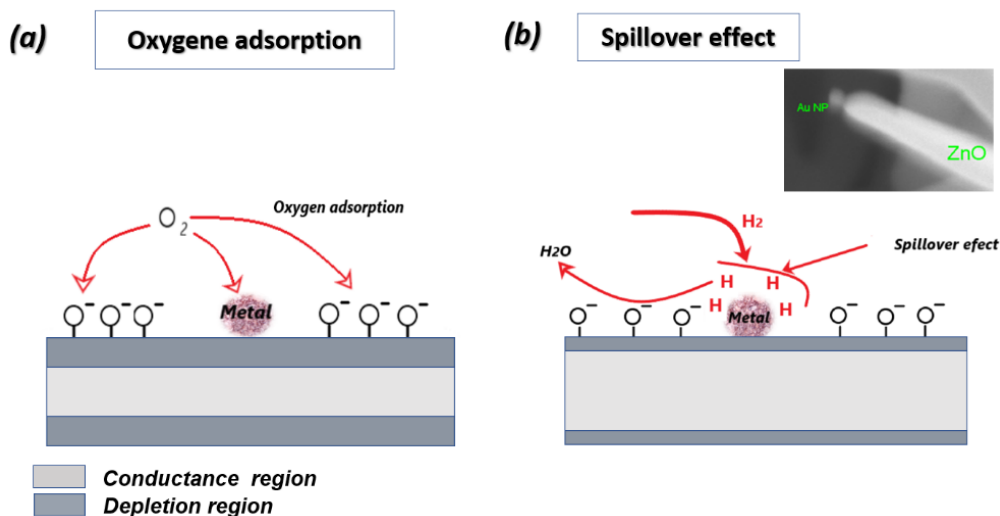


Figure 30. Schematic diagram exemplifying the chemical sensitization mechanism for ZnO/metal under (a) Oxygen; (b) H_2 gas.

4.3.3. Sensing properties

In the present research, H₂ sensors based on 1D ZnO were investigated with particular attention to the sensing characteristics such as gas response, sensors kinetic, stability and selectivity. Figure 31 shows the response of ZnO nanostructures synthesized using different catalysts towards H₂ at several working temperatures: 200 °C, 300 °C, 350 °C, 400 °C and 500 °C. For each ZnO sensor corresponding to specific catalyst, there is a precise temperature corresponding to the optimum response. High response was observed for H₂ at 350 °C for all samples, but ZnO (Au) nanowires and nanorods showed the best one. However, ZnO (Cu) and ZnO (Pt) showed higher response at 300 °C and 200 °C, respectively. ZnO (Ag), instead, gives an appreciable response to H₂ also at elevated temperatures (400 °C and 500 °C). The high sensitivity of ZnO towards H₂ was reported by Akash Katoch et al. who proposed a sensing mechanism that considers the surface metallization of ZnO to Zn in the presence of H₂ [154]. Indeed, the progressive ZnO -to- Zn transition at its surface enhances electrons transport from the surface of metallic Zn to ZnO. This process affects the electrical conductance and improve the sensing properties.

Figure 32(a) and (b) reveal the dynamic response of ZnO (Au) nanowires and nanorods under exposure to 50, 200 and 500 ppm of H₂. ZnO has an n-semiconducting nature, which explain the observed increase of the conductance. As reported in Figure 32(c), ZnO response improves with the increase of hydrogen concentrations, and a high sensors response of about 300 for ZnO (Au) NWs and 50 for ZnO (Au) NRs was observed. Moreover, the signal is stable and recovering perfectly to the baseline level. These results are very interesting, compared to some studies reported in Table 10. This high response of ZnO (Au) NWs is attributed to the expected high specific area compared to bulk material and other morphologies. The sensors speed (sensors kinetic) was discussed by extracting the response/ recovery time from the prepared samples. As explained in the first chapter, the response time is the time for the sensor to reach and respond

to 90% of final conductance toward the gas (G_{gas}). Conversely, the recovery time is taken for a sensor to reach 10 % of the preceding response following exposure to air. The response time was found to be similar for ZnO NWs and NRs (about 1200 s), while ZnO NWs showed a short recovery time of about 100 s. The short-term stability of ZnO (Au) NWs is reported in Figure 32(d), where the same concentration of H_2 (50 ppm) is introduced twice and a stable H_2 response is obtained. Furthermore, the capability of detection of low concentration of H_2 (50 ppm) with stable baseline is verified. The selectivity of the sensors fabricated using all catalysts is displayed in Figure 33, showing that ZnO (Au) nanowires is a highly selective material toward H_2 over CO, ethanol and acetone. It has been shown that ZnO decorated with Au shows high response towards H_2 at high temperature (300 °C and 400 °C) while the sensing performance were poor at lower temperature which is maybe due to the high thermal energy that H_2 needs to react with the pre-adsorbed oxygen through Au [155]. Instead, Pt decorated ZnO has shown good sensing capability toward H_2 at 200 °C and 300 °C. These results are consistent with our work. Moreover, it has been reported previously that Ag oxidizes to Ag_2O with p-type conductivity after an annealing treatment at 500 °C [156]. Therefore, the high response observed for ZnO (Ag) at high temperature (500 °C) may be attributed to the p- Ag_2O /n-ZnO heterojunction formation at the interface. Similarly, p-CuO-n-ZnO heterojunction is formed in case of ZnO (Cu) sample, Cu catalyst was oxidized during the ZnO growth forming CuO. However, more elucidation is still needed to correlate the sensing performances with the nature of catalyst, since many factors such as the content (wt %) of catalyst on the surface (tip of the wire in our case), the shape, the aspect ratio and the possible oxidation of catalyst at high temperature should be taken into account [157].

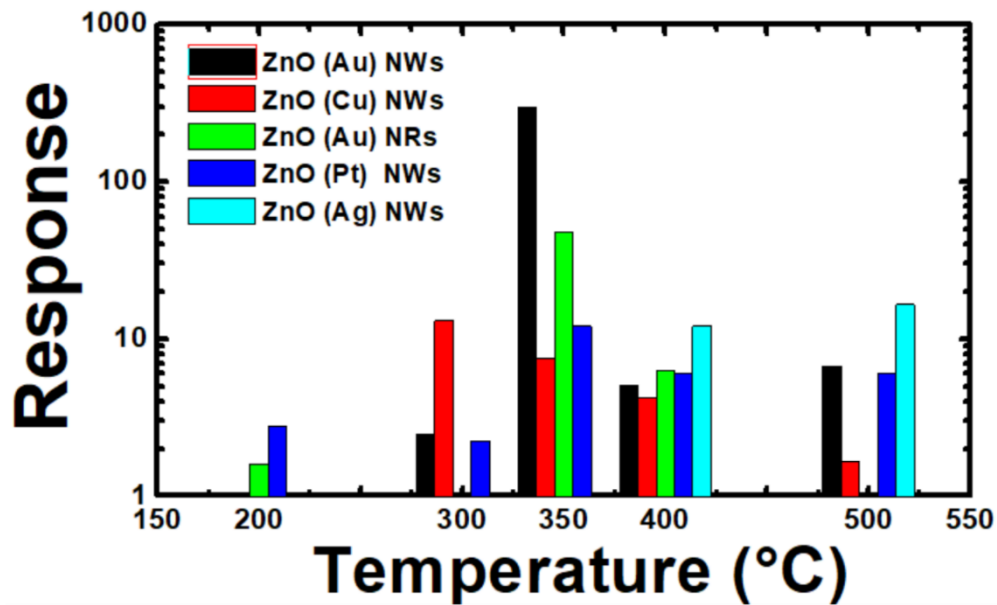


Figure 31. Sensors response under hydrogen injection (500 ppm) of 1D ZnO nanostructures using different catalysts as a function of temperature. The relative humidity was 50%.

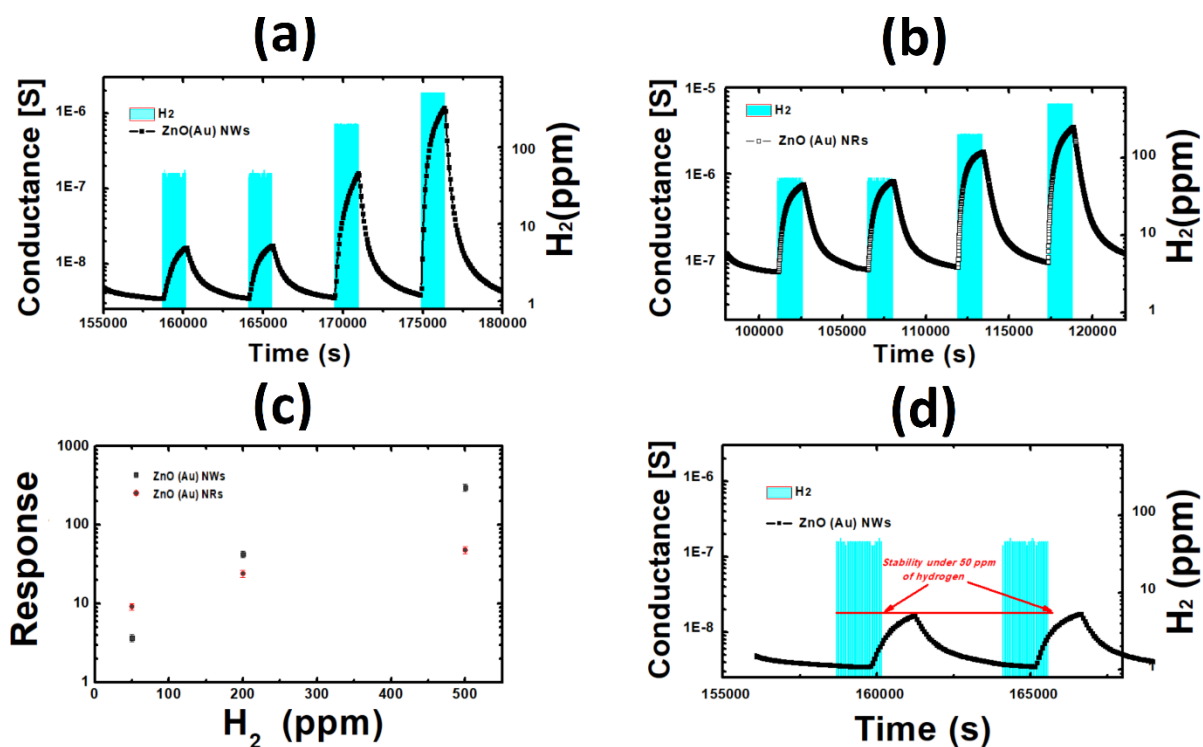


Figure 32. (a) Dynamic response ZnO NWs at 350 °C; (b) Dynamic response of ZnO NRs at 350 °C; (c) Calibration curves; (d) Stability of ZnO NWs under 50 ppm of hydrogen injection.

Table 10. Studies reporting hydrogen sensor based on ZnO nanomaterial.

Material	Technique	Temperature (°C)	Response/H ₂ (ppm)	Ref.
1D ZnO nano-assemblies	PE-CVD	400	13/5000	[158]
1D ZnO NWs	VLS process	400	90/300	[159]
ZnO Nanowires	Ultra-fast Microwave	250	0.95/500	[160]
Pd-decorated ZnO “nanosponge”	Supersonic cluster beam deposition (SCBD)	UV illumination, 20 °C	85/2%	[161]
ZnO nanobundles	nano- templating technique	350	20%/-	[162]
ZnO nanowires	electrochemical anodization	400	11.26/1000	[163]
Vanadium- doped ZnO thin film	Spray pyrolysis	300	55/500	[164]

ZnO two-dimensional nanostructures	thermal oxidation	175	5.37/200	[165]
Nanopillar ZnO	Two-step solution approach	350	28/2500	[166]
NPs-decorated networked ZnO NWs	Chemical vapor deposition (CVD)	Room temperature	4,6 (460%)/1000	[167]
ZnO NWs @ZIF-8	Vapor phase growth + Solvothermal	300	1.44/50	[168]
ZnO nanorods	facile one-pot galvanic-assisted technique	Room temperature	33/2000	[145]
p–n junction of ZnO thin films	D.C. sputtering technique+ CVD	400	1.2/1000	[169]

ZnO thin films	Magnetron sputtering	350	98 %/200	[170]
ZnO thin films	e-beam evaporation	400	59/40	[171]
Ni-doped ZnO thin film	RF sputtering	150	~69%/10000	[172]
Co:ZnO nanorods	hydrothermal method	150	53.7 %/3000	[144]
ZnO nanowires	VLS	350	300 (30000 %)/500	This work

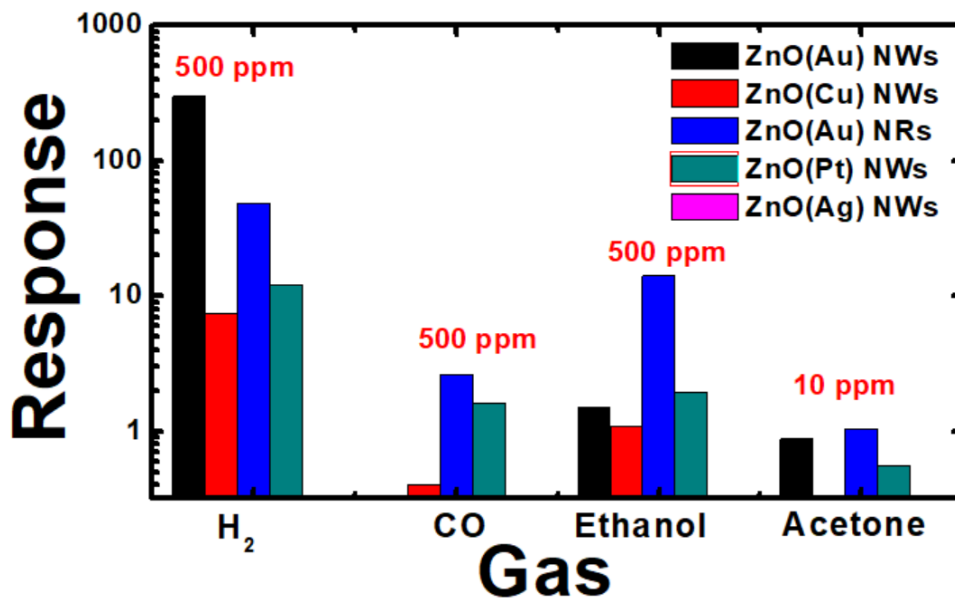


Figure 33. Selectivity histogram of 1D ZnO nanostructures using different catalysts.

Conclusion

The effect of the catalysts (Au, Pt, Ag and Cu) in the VLS growth of 1D ZnO nanostructures, together with their effect on chemical sensors performances, has been investigated. Different form, geometry, size and nanowires/nanorods abundance of ZnO were obtained. H₂ sensors based on 1D ZnO nanostructures were investigated with particular attention to the sensing characteristics. In summary, ZnO nanowires grown using Au catalyst has shown the best performance towards hydrogen at 350 °C showing high response (300 towards 500 ppm), short response and recovery time, high stability and high selectivity towards H₂ over CO, ethanol and acetone.

Chapter 5. 1D α -Bi₂O₃ nanowires and nanoparticles - functionalized α -Bi₂O₃ for chemical sensors applications

Introduction

The detection of volatile organic compounds (VOCs) has a huge importance in many application fields, such as controlling food quality control and health care. In particular, acetone and ethanol are considered as the most common examples of VOCs. In this context, the detection of acetone and ethanol in exhaled breath provides a new tool to monitor easily and non-invasively diabetics, which requires the development of novel sensors with high performances for detecting and monitoring these chemical. This chapter reports the synthesis of p-type $\alpha\text{-Bi}_2\text{O}_3$ nanowires using VLS mechanism. Moreover, they are tested and its sensing properties are explained for future applications as a novel breath analyzer.

5.1. Morphological and structural properties of $\alpha\text{-Bi}_2\text{O}_3$ nanowires

Figure 34 shows $\alpha\text{-Bi}_2\text{O}_3$ nanomaterial grown using different catalysts such as Au, Pt and Cu. Nanowires deposited with Au catalyst have the highest aspect ratio, with Au nanoparticles remaining on the top of the nanowires. Micropillars were observed for Pt catalyst with small density and irregular shape. Cu catalyst allows the formation of few microrods at an early nucleation stage, which maybe is attributed to the insufficient temperature to reach the $\text{Bi}_2\text{O}_3/\text{Cu}$ eutectic point (EP). The differences observed confirm that the growth is controlled by the catalyst, and that its activity is strongly depending on the thermodynamic condition such as precursor gas pressure, growth temperature and nature of catalyst [173]. Moreover, considering that Cu oxidizes easily, its catalytic properties may change in presence of an oxidizing environment and in turn the diffusion rate may be reduced compared by metallic Au and Pt. In this context Nassim et al. studied the effect of iron oxidation state in the carbon nanotube (CNT) growth by heating the samples in different atmospheres (Ar and H_2 , O_2 and mixture of gases). It was highlighted that the catalytic activity of metallic iron results much higher than iron oxide

[174]. Concerning Au catalyst, during the heating and Bi_2O_3 vapor injection, the film transformed to Au droplet allowing incorporation, diffusion and crystallization of nanowires.

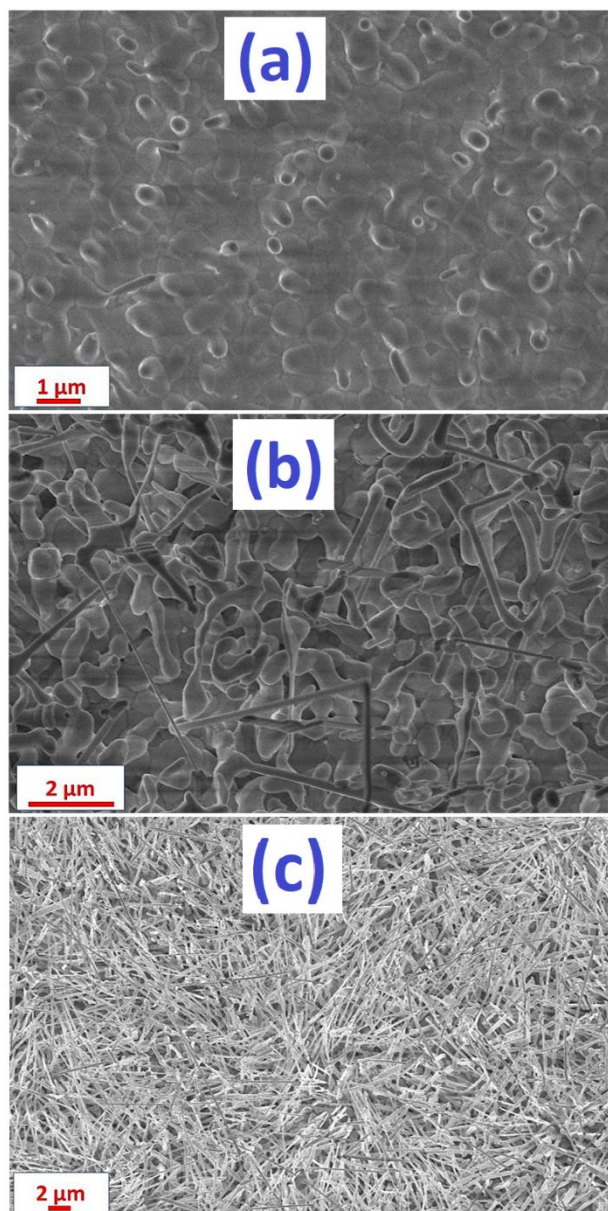


Figure 34. $\alpha\text{-Bi}_2\text{O}_3$ nanomaterial growth using different catalysts. (a) Cu, (b) Pt and (c) Au.

The key point in VLS growth mechanism is that the catalyst droplets form a liquid alloy with the desirable material at specific thermodynamic conditions. In our case, bismuth oxide nanowires growth is controlled by eutectic point (EP) of Au/Bi₂O₃. Exceeding the EP_{Au/Bi₂O₃}, Bi₂O₃ will reach the segregation limit for the liquid nanoparticles and α-Bi₂O₃ nanowires will start growing.

VLS growth mechanism occurs by following four steps as shown in Figure 35. First, Bi₂O₃ powder evaporates, then the vapour containing Bi and O atoms is transported by Ar flow. The adsorbed molecules may diffuse and reach the specific Au droplets. Third, as the concentration of these atoms increases (more Bi₂O₃ vapor) the supersaturation of Au droplet occurs. Finally, bismuth oxide precipitates and the crystallization of α-Bi₂O₃ nanowires occurs at Liquid - Solid interface. As shown in Figure 36, bismuth oxide nanowires were synthesized, and VLS growth mechanism was confirmed by the presence of Au nanoparticles at the top of nanowires. The size distribution shows that nanowires were produced with an average diameter of approximately 100 nm and 6 μm as length. The proposed growth mechanism is supported by the EDX mapping of a single nanowire as reported in Figure 37. The nanoparticle at the tip of the nanowire is composed mostly by gold, while the core of nanowire is composed by bismuth and oxygen, as it is expected for α-Bi₂O₃. The C, Cu and Al peaks detected in the EDX spectrum are due to the TEM grid used for the high-resolution analysis.

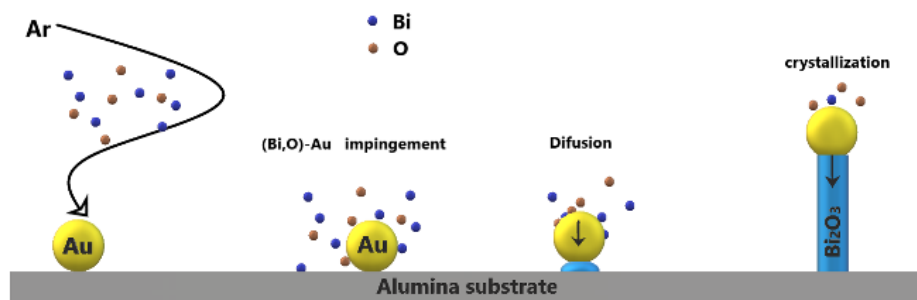


Figure 35. VLS growth mechanism of α - Bi_2O_3 nanowires.

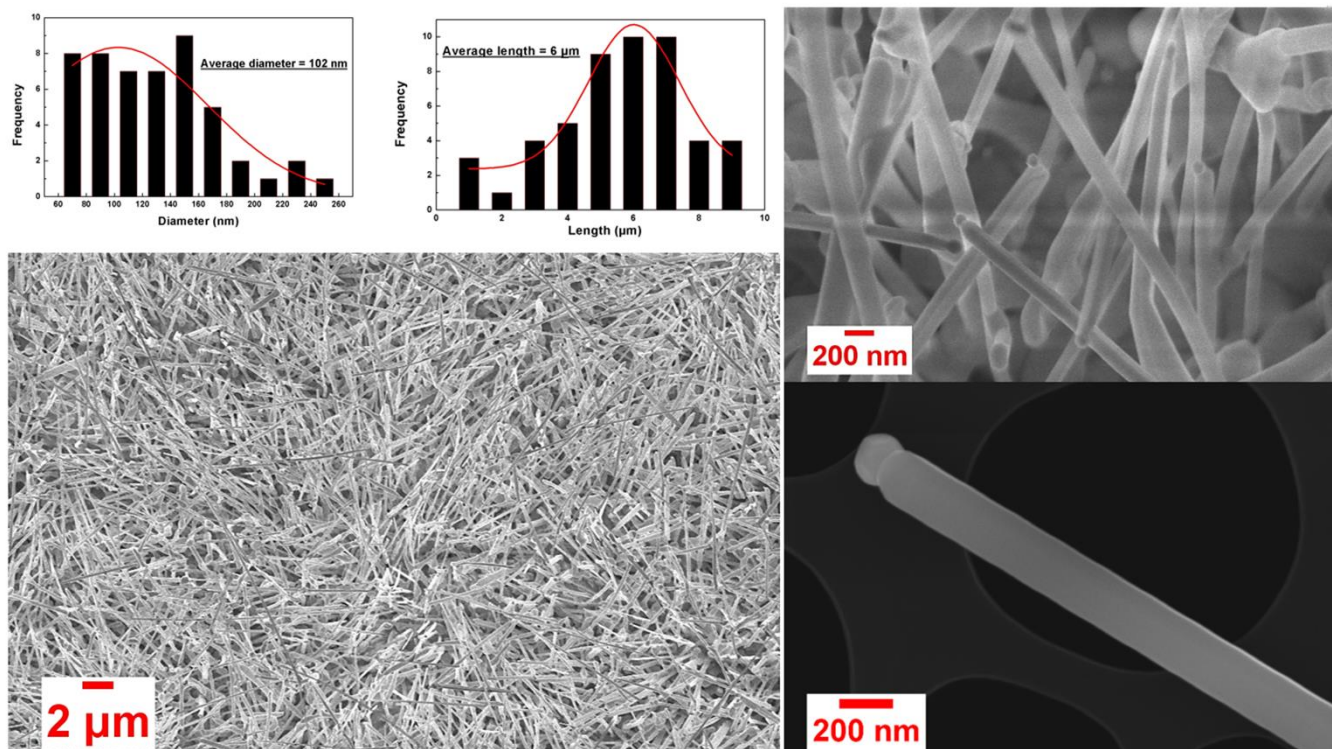


Figure 36. Different magnifications SEM images of α - Bi_2O_3 nanowires growth using Au catalyst, with their diameter and length distribution.

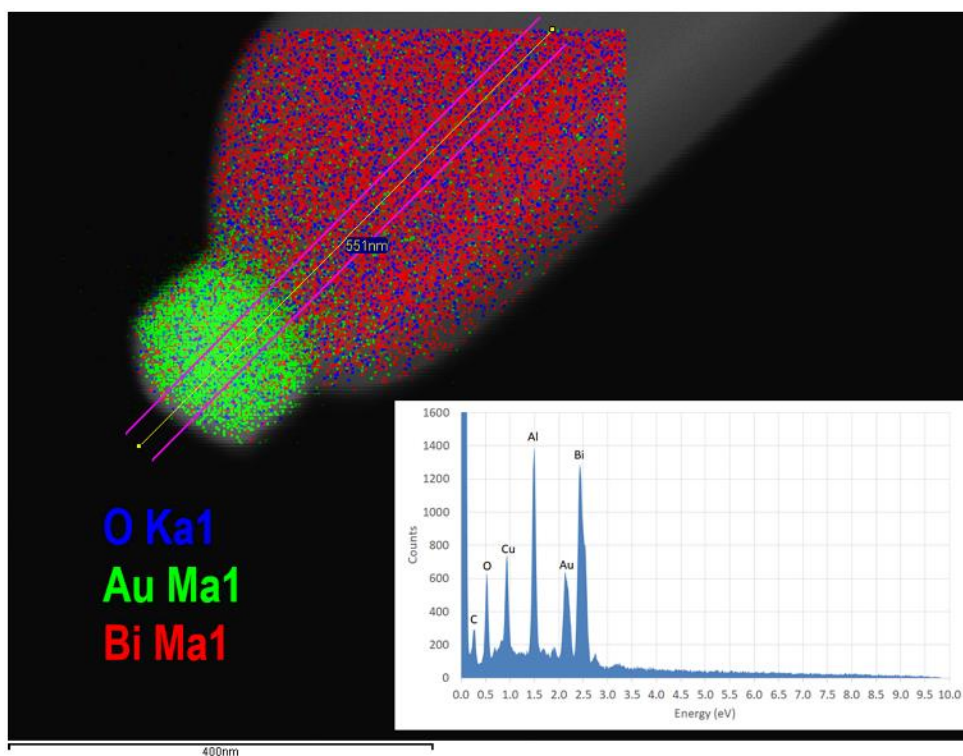


Figure 7. EDX mapping of a tip of α - Bi_2O_3 nanowire. (inset) EDX sum spectra of the nanowire.

In conclusion, for α - Bi_2O_3 (Cu) samples the morphology was not satisfying. Cu catalyst only allows the formation of few microrods at an early nucleation stage, with less connectivity between the rods. Indeed, α - Bi_2O_3 micropillars were observed for the samples grown by Pt catalyst with small density, but each micropillar is isolated from the other one. Instead, in the case of α - Bi_2O_3 (Au) the size of the nanowires obtained was in the nanometre range, and the inter-wires connectivity is assuring a reasonable conductance compared to α - Bi_2O_3 (Pt) and α - Bi_2O_3 (Cu). Moreover, the presence of gold nanoparticles at the wire top may enhance the sensing performances.

Figure 38 shows the XRD pattern of α - Bi_2O_3 , in which the peaks match the standard JCPDS data of bismuth oxide (Reference code .98-000-6262). The phase was confirmed by the presence of significant peaks of α - Bi_2O_3 with monoclinic structure ($a \neq b \neq c$, $\alpha = \gamma = 90^\circ$ and $\beta \neq 90^\circ$) belonging to space group symmetry $P 2_1/c$. Peaks ascribed to Au phase

are attributed to the Au nanoparticles on the top of the NWs. The high chemical stability is demonstrated by the appearance of metallic cubic Au described by (111) and (002) peaks matched the JCPDS (Reference code. 98-002-1528). The non-oxidation of gold catalyst has a crucial role in explaining the sensing mechanism of α -Bi₂O₃ (see next section). All peaks belong to α -Bi₂O₃, showing a phase formation without impurities. The diffraction peaks at 26.83°, 27.22° and 33.08° correspond to the most significant low intensity (111), (01 $\bar{2}$) and (121) peaks respectively, while (120) at 27.24° is considered as preferential orientation. The lattice parameters could be extracted using Bragg law (equations (14) and (15)) that links the lattice parameters of monoclinic structure with the d_{hkl} [164]. In these formulas, (hkl) are Miller indices denoting the X-ray diffraction direction plan, $\lambda=1.54$ Å corresponds to wavelength of the X-rays and the inter-reticular distance d_{hkl} is the shortest distance between two (hkl) plans. Cell refinement was carried out on the measured spectrum, calculating the lattice parameters of the unit cell: $a= 5.86$ Å, $b= 8.15$ Å, $c= 7.54$ Å and $\beta = 113.66^\circ$ in good agreement with those of the standard JCPDS.

$$2d_{hkl} \sin(\theta) = n \lambda \quad \text{Eq 14}$$

$$\frac{1}{d_{hkl}^2} = \frac{h^2}{a^2 \sin^2(\gamma)} + \frac{k^2}{b^2 \sin^2(\gamma)} - \frac{2hk \cos(\gamma)}{a^2 \sin^2(\gamma)} + \frac{l^2}{c^2} \quad \text{Eq 15}$$

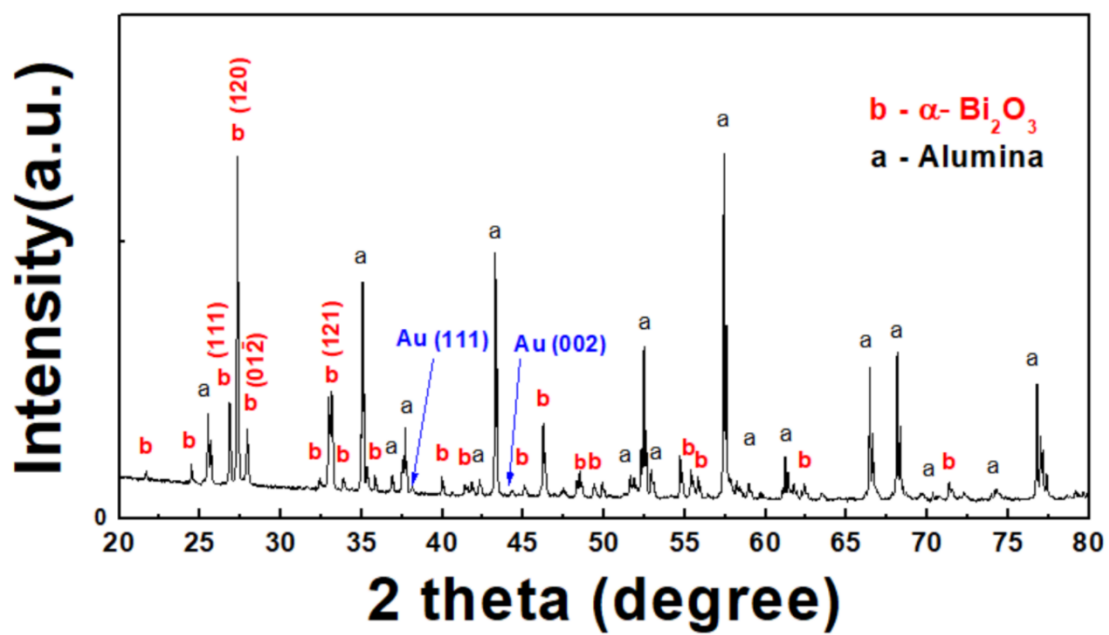


Figure 38. XRD pattern of α - Bi_2O_3 .

5.2. Gas sensing properties

5.2.1. Gas sensing mechanism

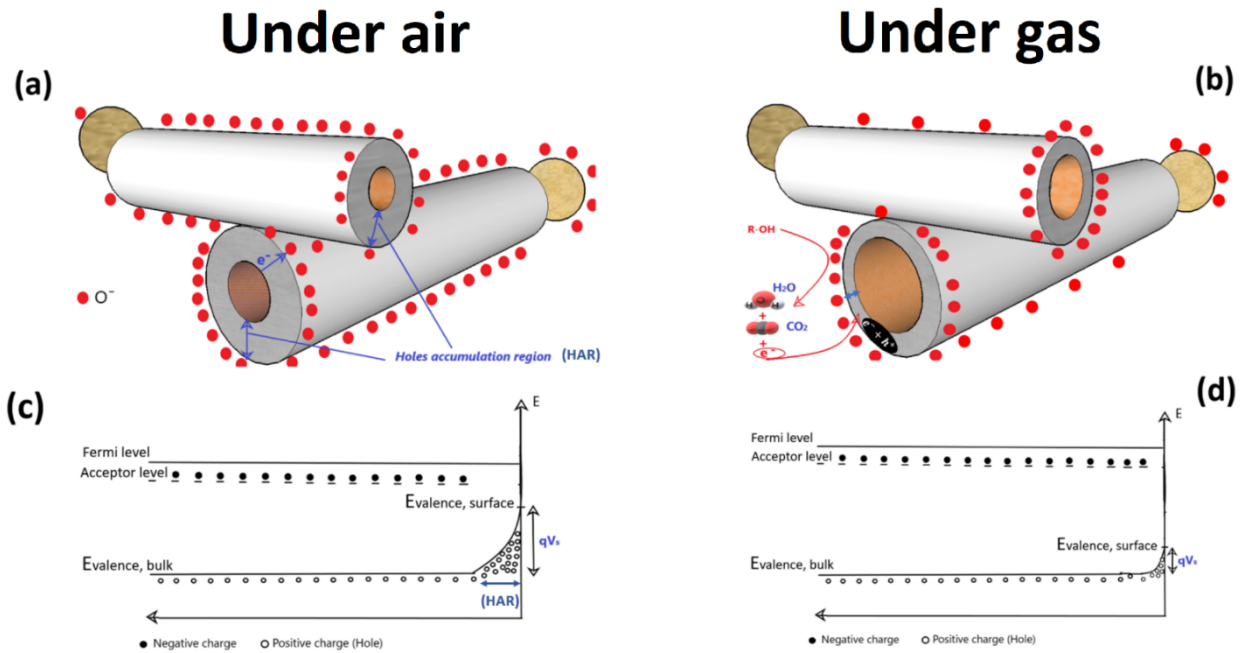
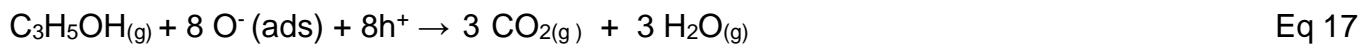
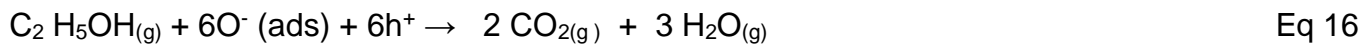


Figure 39. Schematic showing gas sensing mechanisms p -type α - Bi_2O_3 . (a) Under oxygen and (c) its band diagram, while (b) Under reducing gas and (d) its band diagram.

As explained in chapter 1, MOX chemical sensing mechanism is based on; (1) oxygen adsorption (from air) onto MOX surface and (2) surface reactions with the surrounding environment [37]. As α - Bi_2O_3 is a p -type semiconductor, the majority charge carriers are holes. The adsorption of oxygen results in an increase of holes concentration in the valence band (electrons trapped by oxygen ionosorption) [19,27], creating a holes accumulation region (HAR) and thus increasing the conductance of bismuth oxide under exposure to air, as shown in Figure 39(a). Figure 39(b) and equations (16) and (17) report that under exposure to reducing analytes, such as ethanol and acetone [175], there is a reaction with the adsorbed oxygen and electrons are re-inject back into the valence band, decreasing the HAR region and thus decreasing the electrical conduction of bismuth oxide [176].



To further understand the change of electrical behaviour of bismuth oxide gas sensor, the energy band diagram is illustrated in Figures 39(c) and 39(d). The chemisorption of oxygen generates a barrier $q \cdot V_s$ by trapping electrons from the valence band, creating a band bending on the surface of the semiconductor associated to holes accumulation [45]. If we consider the catalytic property of noble metals in enhancing the chemisorption reactions of oxygen by increasing its rate as well as the reaction kinetics, Au catalyst clusters used for growing bismuth oxide nanowires may play an important role in the detection mechanism, increasing oxygen adsorption probability. The small clusters of gold in contact with $\alpha\text{-Bi}_2\text{O}_3$ NWs shown in Figure 40 participate in enhancing the sensing performances without changing the type of chemical interaction [177]. Gold works as a bridge or pathway in chemisorption phenomena via chemical sensitization or spillover effect. This phenomenon occurs when we use catalyst with high chemical stability like Au [178]. The fact that gold remains chemically stable even at 350 °C (best working temperature) or more, reduces the probability of direct electrons exchange (electronic sensitization) between Au and $\alpha\text{-Bi}_2\text{O}_3$. The catalytic property of gold facilitates oxygen ionosorption deepening the holes accumulation region. Considering that the oxygen adsorption rate increases due to Au sensitization, the presence of target compounds (R-OH) such as ethanol and acetone may affect further the hole accumulation region during the interaction with Bi_2O_3 surface, which may improve the sensing properties more than in the case of nanowires without the presence of gold.

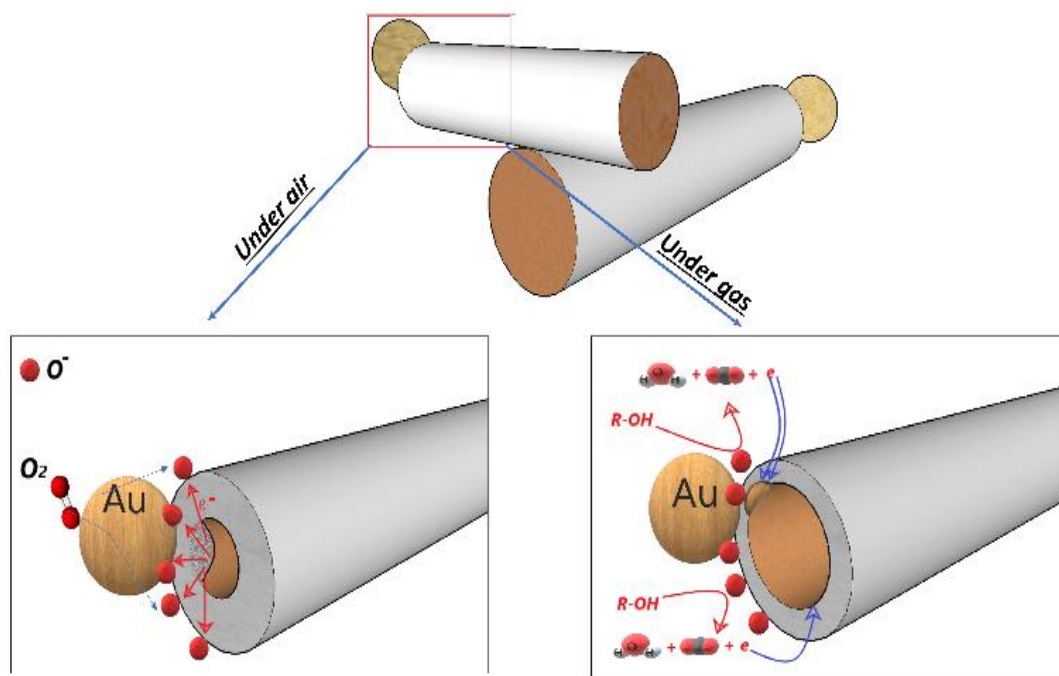


Figure 40. Schematic showing gas sensing mechanisms p-type $\alpha\text{-Bi}_2\text{O}_3$ in contact with Au nanoparticle under air (oxygen) and under reducing gas (R-OH).

5.2.2. Response towards acetone and ethanol.

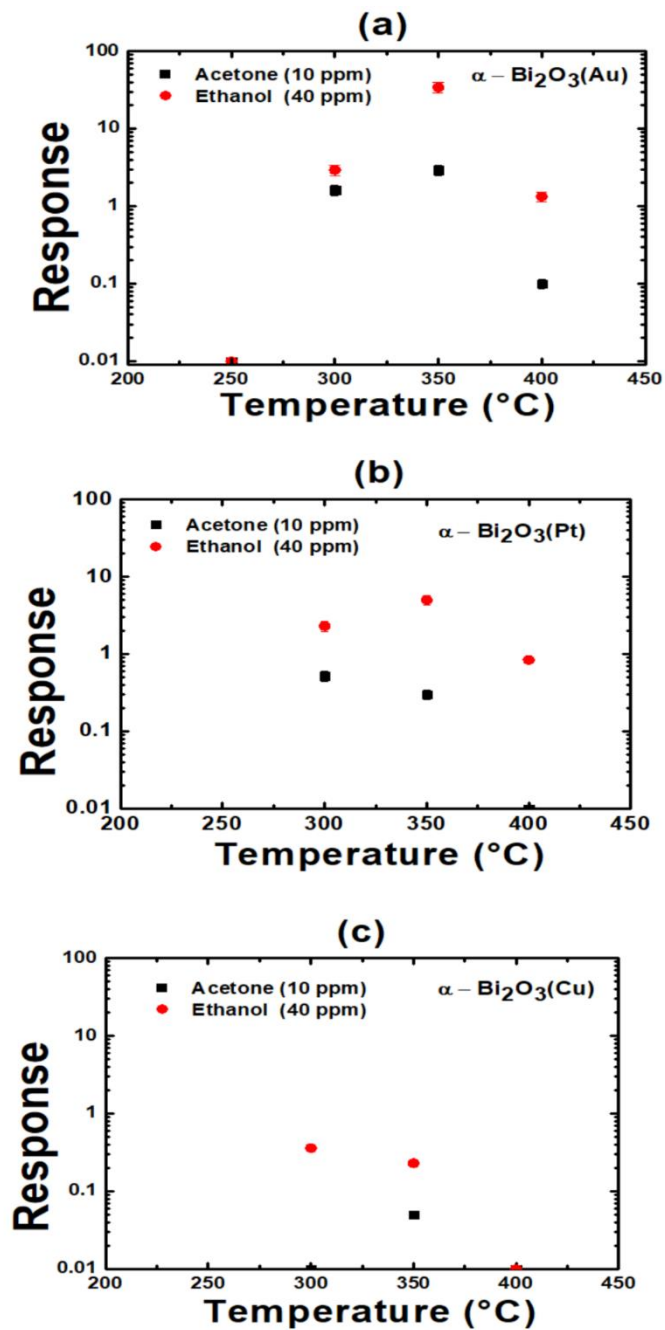


Figure 41. The response of (a) $\alpha\text{-Bi}_2\text{O}_3$ (Au) nanowires, (b) $\alpha\text{-Bi}_2\text{O}_3$ (Pt) micropillars and (c) $\alpha\text{-Bi}_2\text{O}_3$ (Cu) microrods under 10 ppm of acetone and 40 ppm of ethanol against working temperatures at 50% relative humidity.

The sensing performances of bismuth oxide nanowires were investigated, and optimal results using the three catalysts are shown in Figure 41. Bi_2O_3 (Au), Bi_2O_3 (Pt) and Bi_2O_3 (Cu) sensors have been tested towards acetone and ethanol at different working temperatures. Compared with the Bi_2O_3 (Au), Bi_2O_3 (Pt) and Bi_2O_3 (Cu) showed low response. At the best working temperature (350 °C), the responses of Bi_2O_3 (Pt) sensor are 0.29 and 5.15 to 40 and 10 ppm of ethanol and acetone, respectively, while Bi_2O_3 (Cu) shows negligible responses: 0.04 and 0.22 towards acetone and ethanol, respectively. The difference in the sensor response observed for the samples of different catalysts is strongly attributed to the final morphology of nanostructures. Bi_2O_3 (Cu) has a microrods-like structure isolated from each other with a low aspect ratio, and such characteristics are not promising for high performances chemical sensors because the size particles and the connectivity between the particles hugely control the adsorption phenomena and the conductance mechanism in gas sensors. Bi_2O_3 (Pt) sample has a better structure compared Bi_2O_3 (Cu), as it exhibit a pillar-like structure with high length and better connectivity. $\alpha\text{-Bi}_2\text{O}_3$ (Au) shows the best sensing performances compared to $\alpha\text{-Bi}_2\text{O}_3$ (Pt) and $\alpha\text{-Bi}_2\text{O}_3$ (Cu). For this reason, detailed investigations were focused on $\alpha\text{-Bi}_2\text{O}_3$ (Au) nanowires mainly. The samples were tested towards low concentrations of acetone (4 to 10 ppm) and ethanol (10 to 40 ppm) at several temperatures (250 °C, 300 °C, 350 °C and 400 °C). The best operating temperature was 350 °C (as can be seen in Figure 41 (a, b and c)). The dynamic response of bismuth oxide nanowires at 350 °C towards acetone and ethanol is shown in Figure 42. The variation of electrical conductance with air and gas injection is consistent with p-type conductivity of $\alpha\text{-Bi}_2\text{O}_3$, as represented in Figure 39 and explained in last section. The calibration curves of $\alpha\text{-Bi}_2\text{O}_3$ sensors toward ethanol and acetone are presented in Figure 43, showing an increase of the response with the concentration due the increase of the carrier charge exchange by increasing the amount

(quantity) of reducing molecules. The responses of the bismuth oxide are 34.14 and 2.93 to 40 and 10 ppm of ethanol and acetone, respectively. Compared with results already reported in literature on Bi_2O_3 , the present work shows very good responses to low concentrations. There are few studies on chemical sensing properties of Bi_2O_3 : for example, pure $\alpha\text{-Bi}_2\text{O}_3$ showed 1.5 and 1.8 under 100 ppm of ethanol and acetone, respectively [179]. Bi_2O_3 nanoparticles were also used as catalyst to functionalize In_2O_3 , showing a response of 17 and 1.7 towards 200 ppm of ethanol and acetone, respectively [180]. Further comparison with other metal oxides nanomaterials-based acetone and ethanol sensors is shown in Table 11. $\alpha\text{-Bi}_2\text{O}_3$ nanowires show good sensing performance compared to some reports on metal oxides, even if the comparison in some cases is not straightforward considering the different condition and parameters used, such as the humidity level, the gas concentration and the working temperature. Wang et al. synthesized a bamboo raft-like Co_3O_4 by facile one-step room temperature solution process for acetone detection [181]. Good response (10.5@200 ppm of acetone) has been achieved at 180 °C operating temperature. Hongsith et al. prepared Au-doped ZnO nanowires by oxidation reaction for ethanol sensing [182]. The optimum operating temperature resulted 240 °C and the response towards 100 ppm of ethanol was found to be 6. Both these works report a lower operating temperature (180 °C and 240 °C), which is advantageous for reducing the power consumption of the sensors. However, the injected concentrations are 200 ppm for acetone and 100 ppm for ethanol, limiting the utilization of these sensors in some applications such as breath analysis. Another factor that should be taken into account is the humidity level. Recently, Au/ WO_3 macroporous film produced by Zhang et al. showed a good response (35@ 100 ppm of acetone) even at ppb- level with high stability [183]. This sensor has shown the best performances at 410 °C at 20% humidity. Teimoori et al. investigated acetone sensing performances using ZnO thin films prepared by post-annealing of e-beam evaporated Zn thin film [184]. Good response (30@100 ppm of acetone at 280 °C)

was achieved, but in dry air. Indeed, the humidity has a huge impact on the sensing performances of metal oxides based conductometric sensors, since the sensor response is often lower at high humidity level. Therefore, and based on results found in the present work, $\alpha\text{-Bi}_2\text{O}_3$ with high stability at high humidity levels and the ability to detect low concentrations of acetone and ethanol, seems a good alternative material to some conventional metal oxides such as ZnO, SnO₂, NiO and TiO₂ in chemical sensors applications.

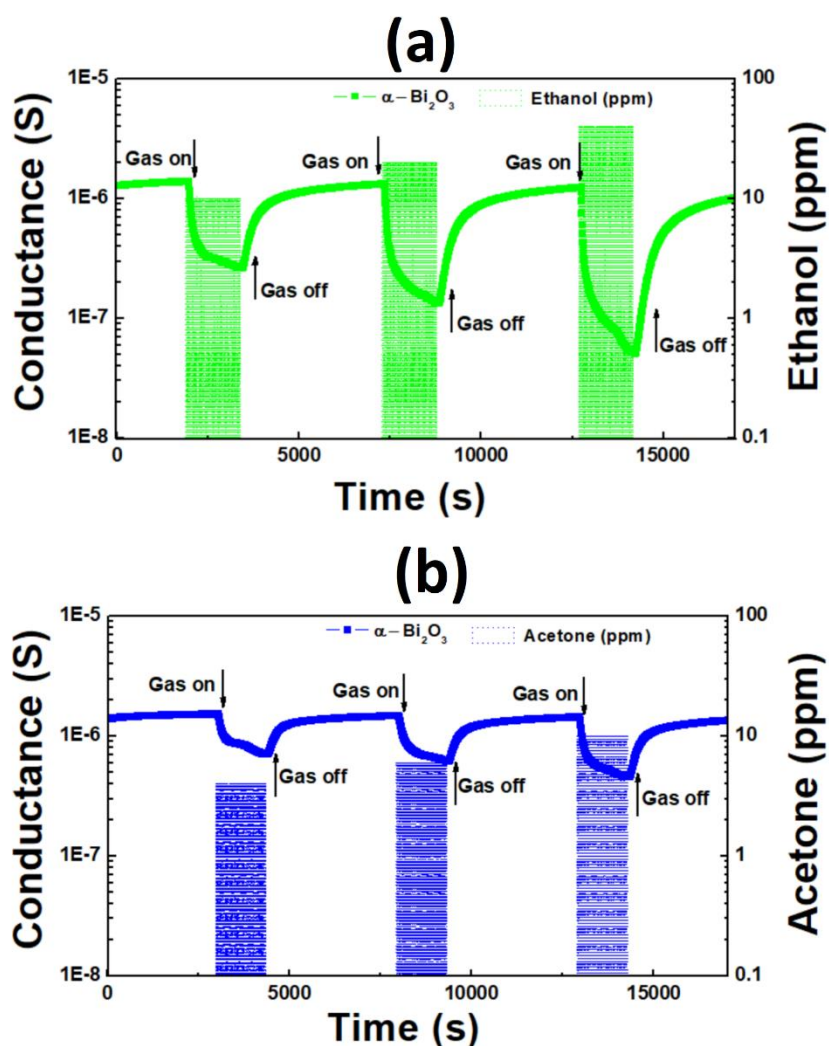


Figure 42. Dynamic response of $\alpha\text{-Bi}_2\text{O}_3$ under (a) ethanol and (b) acetone exposure at 50 % relative humidity.

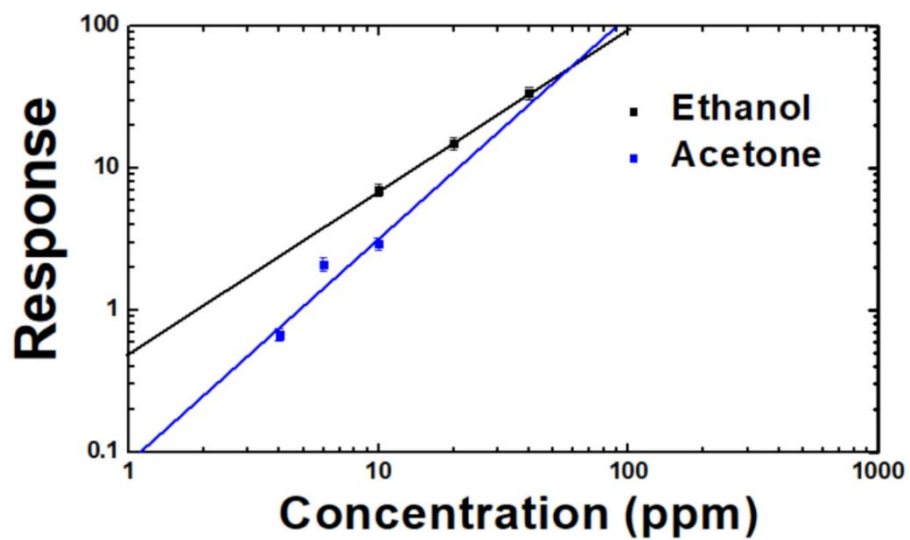


Figure43. Calibration curve of α - Bi_2O_3 under and ethanol and acetone exposure at 50 % relative humidity.

Table 11. Acetone and ethanol sensing performances of metal oxide semiconductors.

Material	Structure	Gas	Temperature (°C)	Humidity	Response /ppm	Ref.
NiO	Nanowires	Acetone	400	50 %	3.6/100 ^{b)}	[185]
CuO	Thin film	Acetone	300	40 %	0.33/16 ppm ^{b)}	[18]
ZnO	Nanoflowers	Acetone	330	NA	7.2/ 100 ppm ^{a)}	[186]
NiO	Nanoparticles	Acetone	330	NA	3/ 100 ppm ^{a)}	[186]
Co ₃ O ₄	bamboo raft- like structure	Acetone	180	NA	10.5 / 200 ppm ^{a)}	[181]
ZnO	Thin film	Acetone	280	Dry air	30/ 100 ppm ^{a)}	[184]
Au/WO ₃	macroporous film	Acetone	410	22 %	35/ 100 ppm ^{a)}	[183]
Nb doped TiO ₂	Nanotubes	Acetone	500	40%	10/ 50 ppm ^{b)}	[187]

NiO/ZnO	Nanowires Heterostructure	Acetone	400	50%	10/ 100 ppm ^{b)}	[185]
Fe ₂ O ₃	Nanoparticles	Acetone	300	42%	26.3 / 100 ppm ^{a)}	[188]
ZnO	nanowires	Acetone	300	NA	0.61/ 1500 ppm ^{a)}	[189]
NiO	Thin film	Ethanol	350	40%	6/ 100 ppm ^{a)}	[190]
Pr doped In ₂ O ₃	Nanoparticles	Ethanol	240	30%	106/ 50 ppm ^{a)}	[191]
Nb doped TiO ₂	Nanotubes	Ethanol	300	40%	1.5/ 50 ppm ^{b)}	[16]
NiO	Nanowires	Ethanol	400	50 %	2.9/ 50 ppm ^{b)}	[185]
ZnO	Nanowires	Ethanol	240	NA	5/100 ppm ^{a)}	[182]
Au doped ZnO	Nanowires	Ethanol	240	NA	6/100 ppm ^{a)}	[182]

Au/SnO ₂	Hierarchical structure	Ethanol	340	20%	18/ 100 ppm ^{a)}	[192]
WO ₃ /SnO ₂	Nanofibers	Ethanol	280	30%	5.09 /10 ppm ^{a)}	[193]
NiO/ZnO	Nanowires heterostructure	Ethanol	400	50%	7.6/ 50 ppm ^{b)}	[185]
α -Bi ₂ O ₃	Nanowires	Acetone	350	50%	2.93/ 10 ppm ^{b)}	Our work
α -Bi ₂ O ₃	Nanowires	Ethanol	350	50%	34.1/40 ppm ^{b)}	

Note: a) Response = G_{air}/G_{gas} or = G_{gas}/G_{air} ; b) Response = $(\Delta G/G)$; NA = not available.

5.2.3. α -Bi₂O₃ for breath analysis application: Humidity effect, sensor kinetic, repeatability and selectivity

α -Bi₂O₃ was tested under the exposure to low concentrations of acetone in presence of very high relative humidity, typical of normal human breath (90%), to study its suitability as new material in breathing test analysis. Moreover, sensor kinetic (response and recovery time), repeatability and selectivity were analysed, as can be seen in Figure 45 and Figure 46 that display the dynamic response of α -Bi₂O₃ under 2 ppm of acetone in the presence of different relative humidity levels ranging from 50 to 90%. The conductance baseline remains stable and is not affected by humidity, which is remarkable and not so frequent concerning MOX. In fact, humidity

dependence is considered one of the main issues that limits the application of conductometric MOX sensors in breath analysis. To the best of our knowledge no previous article has reported the effect of humidity on bismuth oxide gas/chemical sensing properties. However, some studies were carried out explaining how humid air affects the resistance baseline as well as sensor response in MOX. Banerjee et al. explained the change in resistance baseline of ZnO decorated Pd as well as the sensitivity variation in presence of low and high relative humidity percentages [194]. They found that the hydroxyl ions and mobile protons generated by the dissociation and adsorption of water molecules on the surface (active sites) of ZnO are responsible for resistance change. The OH is bonded to the metal cation while mobile proton (hydrogen ion) attach to the oxygen at the MOXs surface, generating other hydroxyl ions. Such process could affect the electrical conductance baseline depending on the coverage of hydroxyl ions and oxygen molecules in the network [195]. At high relative humidity levels, the amount of adsorbed H₂O molecules should increase. However, all active sites on the MOX surface are fully occupied by the primary chemical adsorption of water molecules occurred at low humidity levels. Therefore, water molecules will adsorb on the surface forming a physisorption water layer in contact with the chemisorbed one. This results in formation of a continuous physisorbed water layer with increasing the humidity level. H₂O molecules in these layers are attracted by H⁺ due to the strong electric field and form H₃O⁺. The protons transfer by hopping between two neighbouring water molecules and forms new H₃O⁺. Such proton conductance which is known as Grotthuss mechanism affects the electrical conductance at high relative humidity levels [36,37]. Moreover, taking into account that water at high humidity level can compete with target gas like acetone, the sensor response will automatically be affected [198]. In the present work, α-Bi₂O₃ has been tested at 350 °C. The stability of electrical conductance baseline, as

demonstrated by Figure 45 and Figure 46, may be attributed to the working temperature (350 °C) used to activate the adsorption phenomena, which may favour the desorption of water molecules. Moreover, as shown in Figure 44, the little change in acetone response observed when we increase the humidity from 50 to 90 % may be due to further active sites generated by gold catalyst, which further promote the chemisorption on the surface of the α -Bi₂O₃.

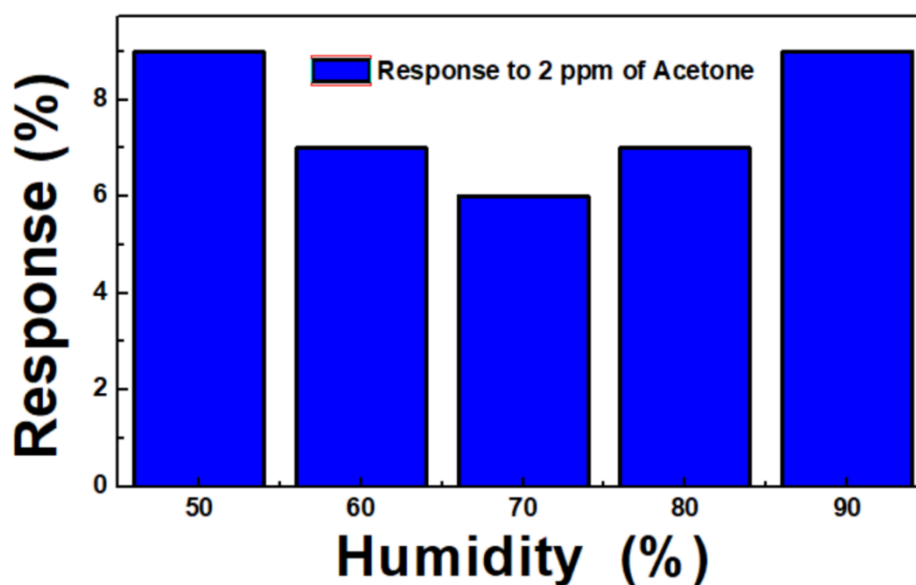


Figure 44. Response (%) ($\Delta G/G \times 100$) of α -Bi₂O₃ nanowires to 2 ppm of acetone in the presence of different humidity (%) levels (50, 60, 70, 80 and 90%).

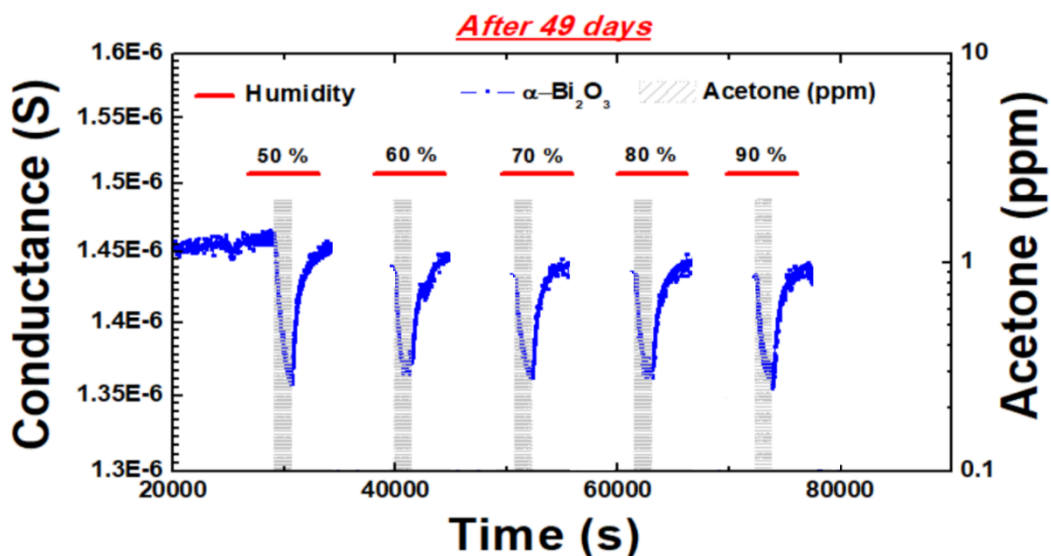


Figure 46. Dynamic response of $\alpha\text{-Bi}_2\text{O}_3$ nanowires after 49 days under 2 ppm of acetone in the presence of different relative humidity (%) levels (50, 60, 70, 80 and 90%).

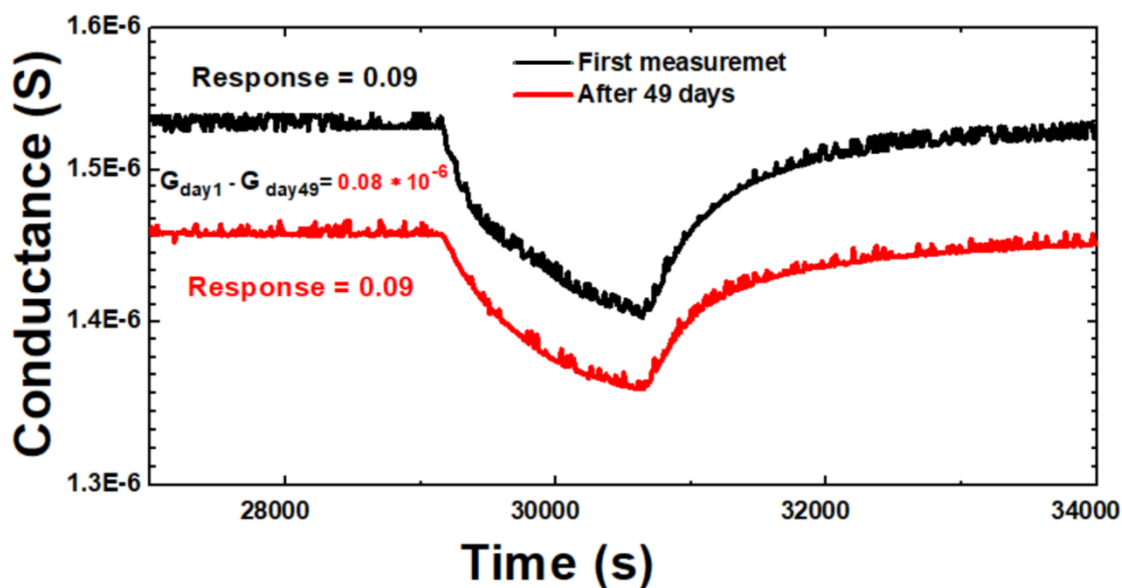


Figure 47. Comparison of electrical conductance baseline of $\alpha\text{-Bi}_2\text{O}_3$ nanowires between the first measurement after 49 days under 2 ppm of acetone.

The limit of detection (LOD) of a chemical sensor refers to the minimum concentration of the target gas that can be reliably distinguished from the absence of the same gas [199]. To estimate the LODs of the sensors, the experimental data are fitted using the power law [200]. LOD of acetone is approximately 680 ppb and 995 ppb for ethanol. Sensor kinetic was studied and response and recovery times were analysed. In particular, **Figure 48** reports the values for 2 ppm of acetone, resulting in a response and recovery times of 130 s and 212 s, respectively. The response and recovery times of the sensors are limited by the filling time of the test chamber, as we need at least 5 min to fill it completely considering the 200 SCCM gas flow used. This means that our sensors are reacting fast even without filling completely the chamber. Sensor response was studied for almost 50 days (**Figure 47**), and it resulted that the responses are the same within 0.09 (9 %) for the two tests with a $0.08 \times 10^{-6} [\Omega^{-1}]$ change in electrical conductance baseline. Moreover, the dynamic responses at different humidity level are incorporated in **Figure 45** and **Figure 46**, demonstrating a good repeatability and stability even at high humidity level. **Figure 25** presents the selectivity histogram of $\alpha\text{-Bi}_2\text{O}_3$: the sensor exhibits high selectivity towards low acetone and ethanol concentrations (10 ppm) compared to NO_2 (10 ppm), NH_3 (10 ppm) and even to high concentration of H_2 (200 ppm) and CO (200 ppm). In the context of breath analysis, the composition of the air slightly changes during the exhalation and inhalation. The difference is the reduction of the amount of oxygen (16%) and a little increase of water vapor as well as an increase of the percentage of carbon dioxide (CO_2) from 0.04 to 5.3 % during exhalation [201]. For this reason, selectivity studies of $\alpha\text{-Bi}_2\text{O}_3$ over CO_2 and O_2 have a huge importance in breath analysis application. Indeed, $\alpha\text{-Bi}_2\text{O}_3$ has shown no response towards moderate concentration of O_2 (21%) and towards CO_2 (1000 ppm, corresponding to 0.1%).

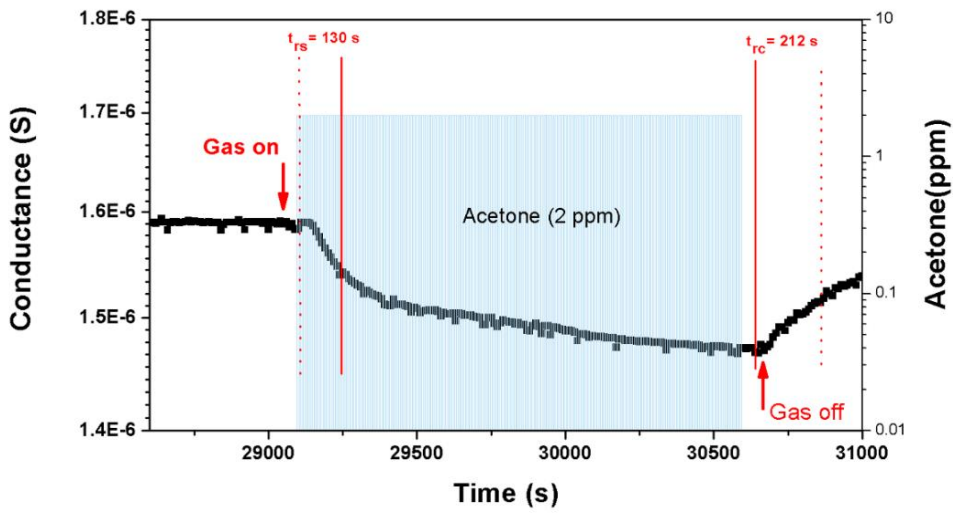


Figure 48. Response and recovery times of α - Bi_2O_3 nanowires under 2 ppm of acetone.

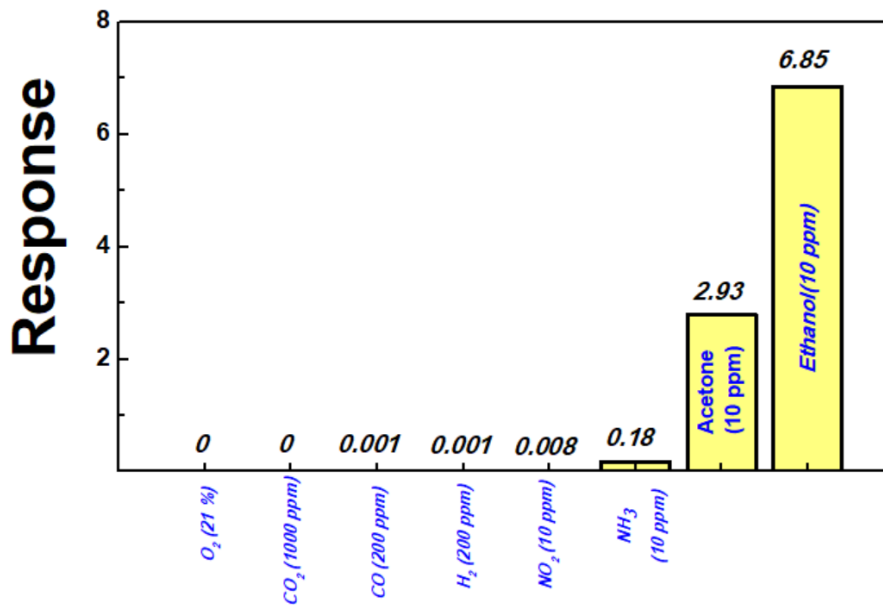


Figure 49. Selectivity study of α - Bi_2O_3 nanowires toward several gases.

5.3. Au, TiO₂ and Ag Functionalized α -Bi₂O₃ NWs

5.3.1. Morphological analysis

Au, TiO₂ and Ag nanoparticles have been synthesized using two steps: 1) deposition of nanofilms (metallic nanoclusters) on alumina substrates, 2) thermal annealing in air using a furnace at specific temperature and annealing time as described in the next section. Figure 50 (a, b and c) shows the nanoparticles morphologies of the films. The nanoparticles of gold and silver have a spherical shape with uniform size and without any kind of agglomeration. Instead, an island-like shape has been observed for TiO₂ which is maybe attributed to the porous alumina substrate together with the high melting point of titanium.

Figure 50 (d, e and f) show α -Bi₂O₃ decorated with Au, TiO₂ and Ag nanoparticles. As shown, the nanoparticles are well distributed on the surface of the nanowires giving a good quality loaded sample. Moreover, the quality of the pristine α -Bi₂O₃ nanowires keep good without big changes, in terms of diameter, homogeneity and density, even after being decorated with nanoparticles and the following annealing treatment for several hours at high temperature.

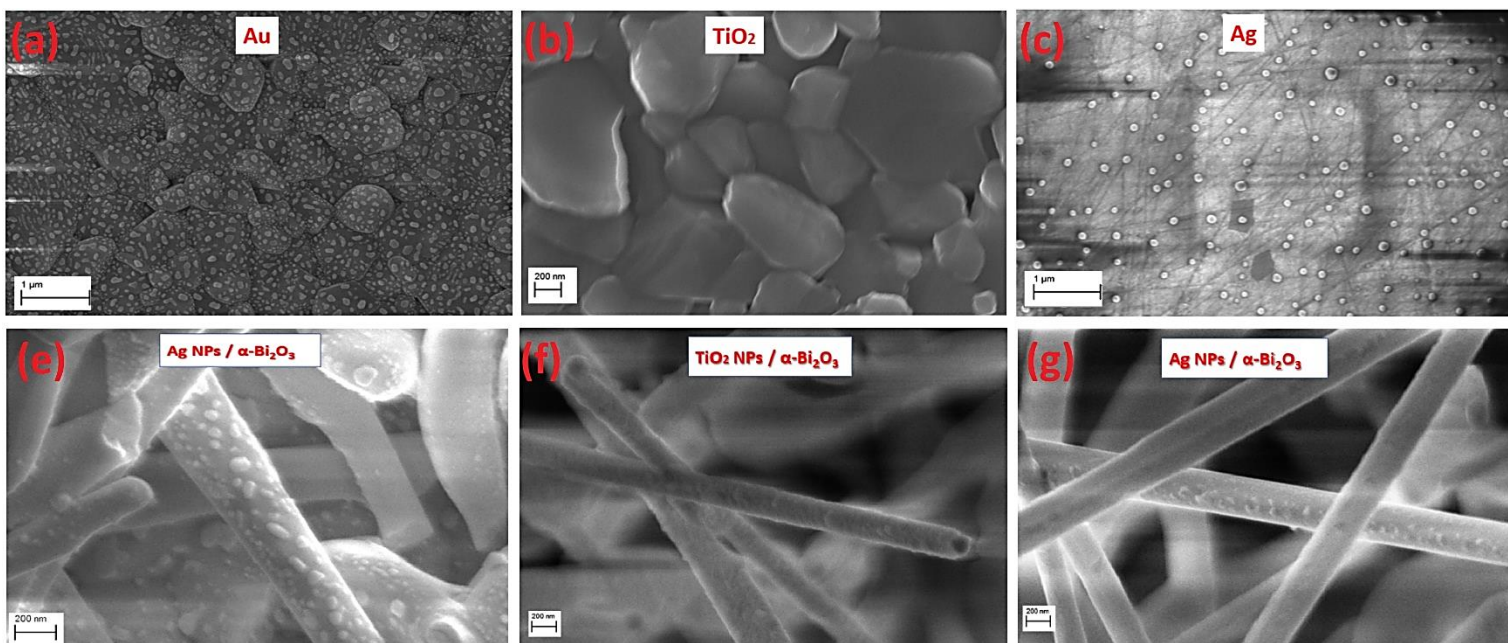


Figure 50. α -Bi₂O₃ decorated with Ag, TiO₂ and Au nanoparticles.

5.3.2. H₂ response improvement using nanoparticles - functionalized α -Bi₂O₃ NWs sensors

Functionalized α -Bi₂O₃ NWs samples have been tested towards hydrogen (H₂) (Figure 51). The idea of choosing hydrogen as target gas came from the selectivity study that has been performed in the previous section. It has been observed that pristine Bi₂O₃ showed a weak response towards H₂.

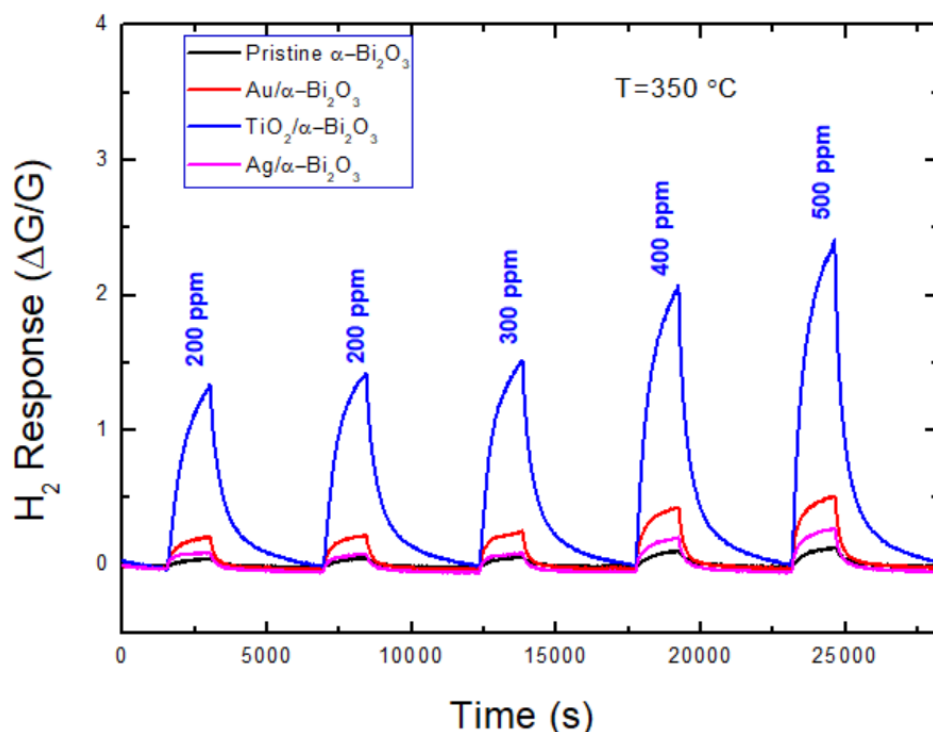


Figure 51. Response of α -Bi₂O₃ decorated with Ag, TiO₂ and Au nanoparticles towards hydrogen.

The gas sensing properties of the NPs-functionalized α -Bi₂O₃ has been investigated. Taking Figure 49 as a reference, we can observe that the pristine α -Bi₂O₃ nanowires showed good selectivity towards acetone and ethanol against the other gases such as H₂. The functionalization of the MOXs nanowires with metal or metal oxide nanoparticles is required

to speed up the reaction and creating new heterojunction in order to enhance the sensitivity and the selectivity of the sensor.

The functionalized α -Bi₂O₃ NWs samples have been tested towards different concentrations of H₂ (200, 300, 400 and 500 ppm) at 350 °C and their responses are shown in Figure 51. The samples show same response towards 200 ppm of H₂, which demonstrate the good repeatability. The response increased by increasing the concentration of the H₂. The response is significantly increased after functionalizing the α -Bi₂O₃ nanowires with other nanoparticles. In particular, TiO₂ nanoparticles lead the highest effect and the greatest response among them, exhibiting a great enhancement toward 500 ppm of H₂ at 350 °C with a 25-fold higher response compared with α -Bi₂O₃. This can be explained by the formation of p-n junction (α -Bi₂O₃ – TiO₂) at the interface that can affect the hole accumulation layer and increase the response of the sensor. Since the Au is chemical stable and does not oxidize easily at highest temperature, the enhanced response observed for Au-Bi₂O₃ is attributed to spillover effect (chemical sensitization) [100]. Gold nanoparticles on the surface of α -Bi₂O₃ NWs catalytically stimulate the dissociation of molecular oxygen and atomic products obtained during this process to the α -Bi₂O₃ NWs [17]. The high response observed after modifying the α -Bi₂O₃ nanowires by Ag nanoparticles is maybe attributed to the formation of p-p junction (Ag₂O- α -Bi₂O₃) at the interface specially, if we consider the formation of Ag₂O (a p- type semiconductor) after the annealing treatment. In this context, it has been reported previously that Ag oxidizes to Ag₂O with p-type conductivity after an annealing treatment at 500 °C [156], which is in agreement with our work.

Conclusion

In this chapter, α -Bi₂O₃ nanowires have been grown using different catalysts, i.e. Au, Pt and Cu. However, Au catalyst showed the best morphology with the highest aspect ratio. The

sensing properties has been investigated, showing a good response towards low concentrations of acetone and ethanol, long-term stability (up to 50 days), high selectivity over other gases, excellent stability at high humidity level (up to 90 %) and short response and recovery time. This study could be a starting point for the possible production of a real-time sensor based on p-type α -Bi₂O₃ nanowires as an efficient new material for diabetes monitoring.

Chapter 6. 2H-WSe₂ nanosheets for chemical sensors applications: NO₂ detection at room temperature

Introduction

The health hazards caused especially by NO_2 emission, which is considered as one of the dangerous pollutants, are widely acknowledged by the World Health Organization (WHO) in air pollution guidelines. Recently transition-metal di-chalcogenides (TMDC) are considered as a novel class of materials that can be used as nano-conductometric sensors, due to their unique chemical and physical properties. This chapter investigates in detail the synthesis, the characterization and the efficiency of WSe_2 nanosheets as NO_2 sensors at room temperature.

6.1. Structural and morphological properties of 2H- WSe_2 grown using APCVD

A comparison of the X-ray diffractogram (XRD) analysis of exfoliated tungsten di-selenide in Argon atmosphere synthesized at 1h reaction time in the air (at 300 °C) is shown in Figure 52(a). The results indicate that the pristine material is a pure phase material with a hexagonal crystal system of space group $P6_3/mmc$ and space group no. 194. All the diffraction peaks are correlated and indexed to the ICDD no: 00-038-1388 of 2H- WSe_2 , according to literature. The peaks of pristine 2H- WSe_2 are: (100), (103), (006), (105), (008), (107), (108), (203), (0010), and (205) at around 31.4° , 37.8° , 41.7° , 47.3° , 56.6° , 59.4° , 66.2° , 69.4° , 72.7° , and 76.2° respectively. Different oxidation parameters were varied to understand the thermal stability of the pristine 2H- WSe_2 . The XRD spectra were recorded to understand the extent of oxidation and the air-stability of the bulk as-prepared 2H- WSe_2 . Previous reports on monolayer WSe_2 (synthesized by a bottom-up approach [202,203]) have indicated that the single layer 2H- WSe_2 is highly prone to oxidation because of air-induced protrusions at its edges. However, the oxidation with air exposure occurs mostly at step edges after the exposure of 2H- WSe_2 in air for 9 weeks, while it is not detected on the internal terraces; therefore, the oxidation of the step edges in WSe_2 appears to be a self-terminating process.

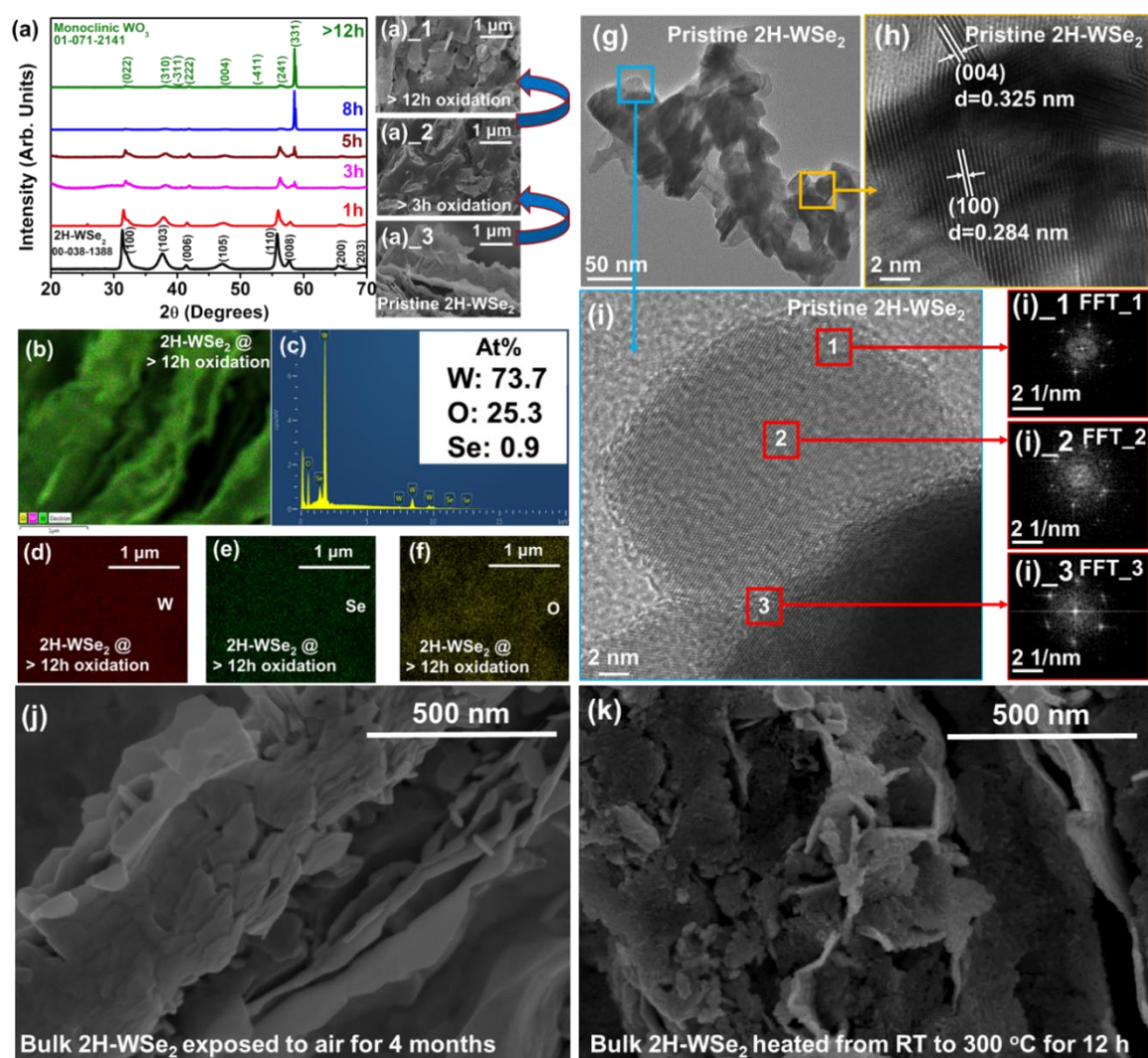


Figure 52. (a) Changes in X-Ray Diffraction (XRD) due to heat treatment of exfoliated 2H-WSe₂ (at elevated temperatures of 300 °C) in air, resulting in partial incorporation of oxygen, (a)₁ HRSEM of 2H-WSe₂ at >12 h oxidation in air, (a)₂ HRSEM of 2H-WSe₂ at >3 h oxidation in air, (a)₃ HRSEM of pristine 2H-WSe₂, (b) Elemental mapping of 2H-WSe₂ at >12 h air oxidation, (c) Qualitative E.D.X. of 2H-WSe₂ at >12 h air oxidation, (d) Elemental map of W in 2H-WSe₂ at >12 h air oxidation, (e) Elemental map of Se in 2H-WSe₂ at >12 h air oxidation, (f) Elemental map of O in 2H-WSe₂ at >12 h air oxidation, (g) BF-TEM image of pristine 2H-WSe₂, (h) Lattice fringes in pristine 2H-WSe₂, (i) HRTEM of pristine 2H-WSe₂ with corresponding FFT patterns in position 1 indicated by (i)₁, position 2 shown by (i)₂ and position 3 indicated by (i)₃.

Our studies, on the other hand, are involved as a combination of bottom-up bulk synthesis of 2H-WSe₂ with a top-down exfoliation method in ethanol and isopropanol as solvents. First, we investigated the effects of the ambient conditions towards our bulk material (i.e. the 2H-WSe₂ synthesized on the W foil). Although no in-situ reduction was used for our synthesis,

the bulk material when exposed to air at room temperature showed no visible or morphological changes. The bulk 2H-WSe₂ after 4 months of being kept in the ambient conditions remains the same without any changes in its phase, indicating that our process is very reliable and prevents ambient oxidation of the material. In order to understand the effects of oxidation, we varied two reaction parameters, namely the temperature and the total oxidation time. For a variation in the reaction temperature, the oxidation of the pristine 2H-WSe₂ is started from room temperature till 300 °C. Each of these oxidations at different temperatures were carried out for 12h (maximum time limit for each oxidation temperature). As evident from Figure 53, the bulk material is intact and the incorporation of oxygen is not recorded in the qualitative EDS spectrums for the material oxidized at 50 °C, 100 °C, 150 °C and 200 °C. However, at 300 °C, we see an almost complete oxidation of the 2H-WSe₂ into WO₃ (after 1h oxidation of the bulk). For a variation in the total reaction time, we kept the oxidation temperature fixed at 200 °C. This is because the gas-sensing measurements were carried out starting from room temperature till 150 °C. Figure 52 (a) depicts the change in the XRD peak intensities starting from 1 h. At 200 °C for 1h, the material is still in the pristine 2H-WSe₂ form and the peaks can be easily correlated to the ICDD no.: 00-038-1388. The anisotropic line broadening of 2H-WSe₂ is also evident till 5h of the total reaction time. But around 5h of the oxidation, we see the formation of a tiny hump around 58.59 °, which is the clear indicator of the formation of the (332) plane of monoclinic WO₃. At 8h and 12h oxidation times, the (332) plane of WO₃ is very intense, suggesting a preference in growth towards that crystallographic plane. The other crystallographic planes can then be easily identified (for 5h, 8h and 12h) which are: (022) at 31.96 °, (310) at 38.19 °, (-311) at 40.57 °, (222) at 41.98 °, (004) at 47.65 °, (-411) at 52.6 °, (241) at 56.26 °; all of which are consistent with the formation of the monoclinic phase of WO₃ (ICDD: 071-2141). The material heat treated beyond 12 h of oxidation at 200 °C, shows in its qualitative E.D.S. measurements in the HRSEM shows the presence of O, W and Se, indicating that some WSe₂ might still be un-

converted. The morphology of the monoclinic WO_3 heated at 300 °C for 12 h shows that the flake like morphology is still maintained but it consists of tiny particulates growing as an aggregation on the surface of the bulk. At temperatures of 300 °C, there is partial incorporation of oxygen into the system when being annealed in air at reaction times greater than 12 h. Still, the stability of the pristine material is well maintained both at room temperature and till 150 °C. Figure 52(a) _1 to Figure 52(a) _3 show the changes associated with the gradual evolution in morphology, where the flake-like or sheet-like structure is maintained for 2H- WSe_2 . Transmission Electron Microscopy (TEM) measurements helped to identify the morphology and to confirm the structure of the as-synthesized pristine 2H- WSe_2 . The bright-field (BF) TEM images help us estimating the average sizes of the 2H- WSe_2 sheets (ranging between 50-80 nm). The lattice fringes, as shown in Figure 52(h), is calculated to be around 0.284 nm (for (100) plane) and 0.325 nm (for (004) plane) corresponding to the ICDD database no.: 00-038-1388 for 2H- WSe_2 . High-Resolution Transmission Electron Microscopy (HRTEM) measurements of the WSe_2 nanosheets helped us to identify honeycomb-like lattices, which are very typical of the 2H-variant of WSe_2 . Corresponding Fast Fourier Transforms (FFTs) of the three selected areas highlighted in red (marked as 1, 2, and 3) in the flakes also confirm the crystal structure of our pristine 2H- WSe_2 . The EDS measurements obtained from TEM/HRTEM, as well as from HRSEM imaging, show a repeated deviation in the stoichiometry of 1:2 (W: Se) indicating that the material probably contains Se vacancies. A long-running study on the air-annealing of 2H- WSe_2 at temperatures starting from 50 °C till 200 °C (at 1h) shows little to almost no incorporation of oxygen into the system, as shown in Figure 53. However, as indicated above, the heat treatment of 2H- WSe_2 at 300 °C evidently leads to the formation of monoclinic WO_3 which is also ascertained by the qualitative EDS spectra as shown in Figure 53(w).

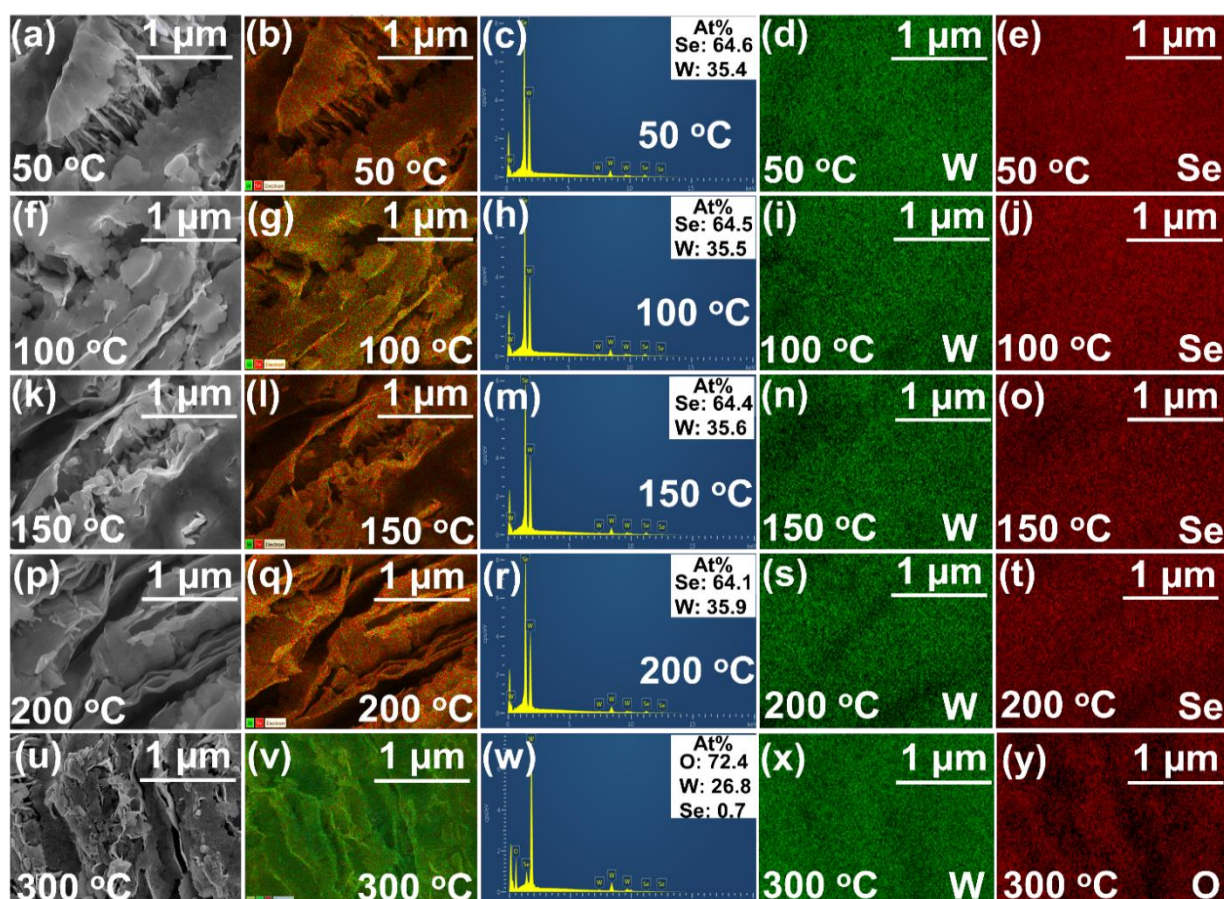


Figure 53. High Resolution Scanning Electron Microscopy (HRSEM), EDS and Elemental Mapping of air-annealed tungsten di-selenide ($2H-WSe_2$) at different temperatures starting from (a) 50 °C, (b) 100 °C, (c) 150 °C, till (d) 200 °C.

6.2. The stability of $2H-WSe_2$ dispersion at different sonication frequency

Since both ethanol and isopropanol proved to be ideal low-boiling solvents for our exfoliation experiments, further analyses in ethanol dispersions were carried out. The main idea was to find out the optimal stability of the dispersions obtained after exfoliations because it would help in subsequent simple integration of the $2H-WSe_2$ flakes into the sensor-based system. The ethanol-based dispersions were prepared by a similar method as described before (1h sonication at 80 kHz and 37 kHz, respectively). The stability and homogeneity of these ethanol-based dispersions were checked for extended periods (starting from Day 1 till Day 60), as shown in Figure 54 (a) to 3 (f). Observing digital photographs of the dispersion, very

little change was observed in color or the homogeneity of the original as-synthesized bulk 2H-WSe₂ on W foil dispersed in ethanol. From day 40 onwards, the 2H-WSe₂ dispersions start to show a very slight difference in their color, indicating that the larger flakes of the as-exfoliated material have started to settle down. At day 60, a slightly transparent portion of the ethanol-based dispersion of 2H-WSe₂ was observed. We can see the W foil used during the exfoliation optimization procedure (which came into focus once the 2H-WSe₂ flakes started to settle down in the dispersion). Atomic Force Microscopy (AFM) image in Figure 54 (g), along with the height profile, shows the clear presence of layers or sheets of WSe₂ after drop-casting on Si/SiO₂ substrate [204]. These observations indicate that a lower sonication frequency (at 100% power output) coupled with a higher sonication time is another reliable method to obtain few-layered flakes of 2H-WSe₂ without any severe changes in its final morphology. The stability of the dispersions of 2H-WSe₂ prepared at 37 kHz and 80 kHz frequencies were also compared after letting them sit for 60 days to understand the extent of dispersibility in either case. After 60 days, we observe that the 80 kHz dispersion is still homogenous, while the 37 kHz dispersion has started to settle down, as shown in (Figure 55).

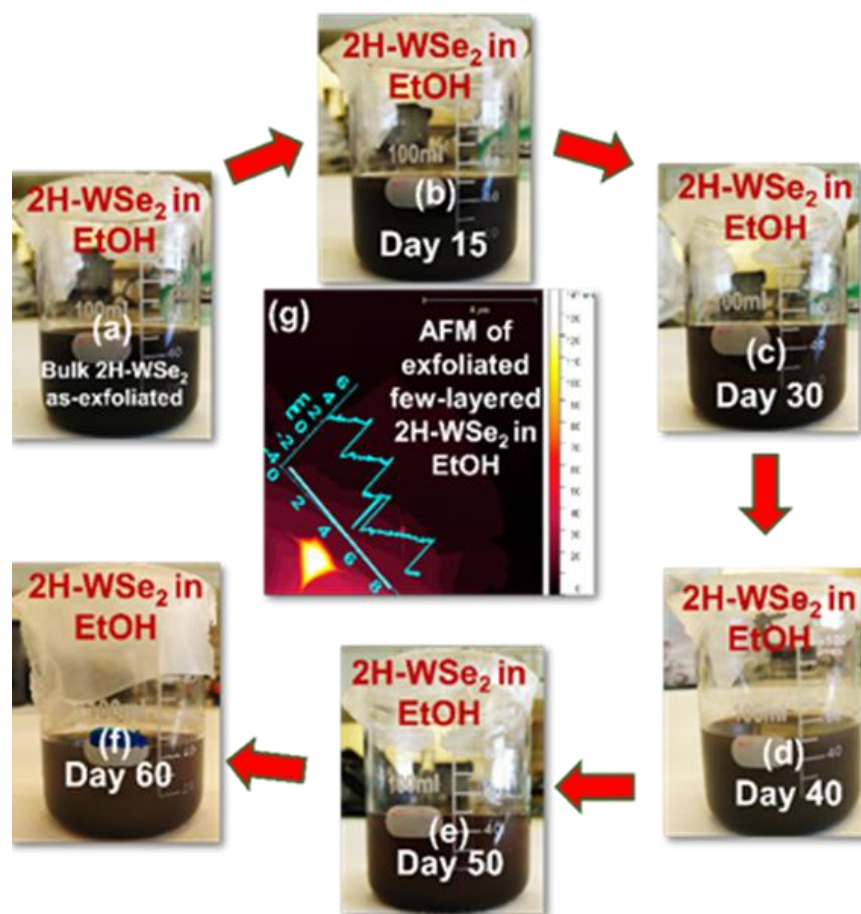


Figure 54. Inspecting the stability of 2H-WSe₂ dispersions (prepared in ethanol at 80 kHz starting from (a) Bulk 2H-WSe₂ on W foil sonicated in EtOH, (b) 2H-WSe₂ dispersion in EtOH on day 15, (c) 2H-WSe₂ dispersion in EtOH on day 30, (d) 2H-WSe₂ dispersion in EtOH on day 59 (with a slight change in the color and consistency of the dispersion), (e) 2H-WSe₂ dispersion in EtOH on day 50, (f) 2H-WSe₂ dispersion in EtOH on day 60 (where the dispersion has started to settle down as indicated by the appearance of bulk 2H-WSe₂ grown on W foil), and (g) Atomic Force Microscopy (AFM) measurement of 2H-WSe₂ in ethanol (height profile shows many-layered flakes ($\sim 5.5 \pm 0.3$ nm in height for an eight-layers).

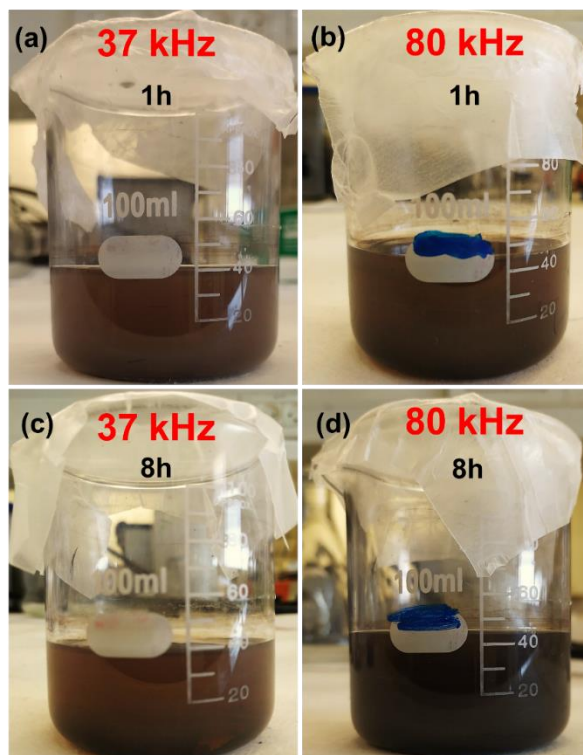


Figure 55. Stability of ethanol-based 2H-WSe₂ dispersions prepared at (a) 37 kHz (1h), (b) 80 kHz (1h), (c) 37 kHz (8h), and (d) 80 kHz (8h).

6.3. X-ray Photoelectron Spectroscopy (XPS)

The optimization of frequency and output power is, therefore, crucial in our experiments because it is a significant indicator of the resulting stability and the final morphology of the flakes. The X-ray Photoelectron Spectroscopy (XPS) measurements of the exfoliated 2H-WSe₂ at 80 kHz and 37 kHz (1h sonication) are also compared. We observe the presence of only W and Se in **Figure 56** where W can be resolved into W 4f_{7/2} and W 4f_{5/2} at 32.5 eV and 34.63 eV, and the doublet peaks at 54.5 eV and 55.3 eV corresponding to selenium in the freshly exfoliated material.

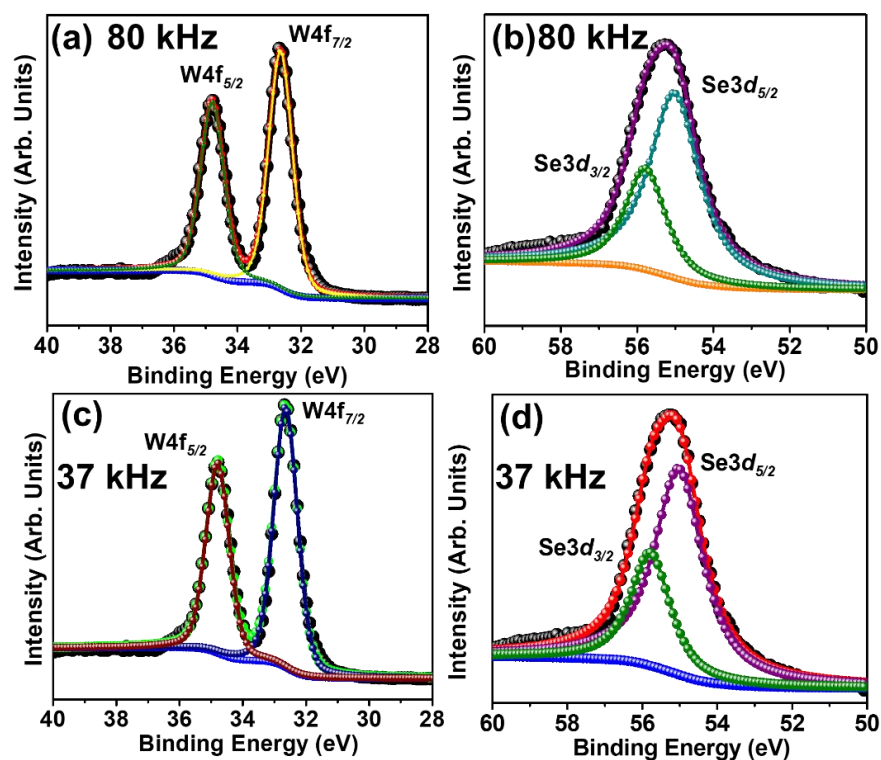


Figure 56. X-Ray Photoelectron Spectroscopy (XPS) measurement of exfoliated 2H-WSe₂ indicating the oxidation states and the presence of both W and Se in (a) at 80 kHz, (b); at 37 kHz (1h sonication).

6.4. Effect of modulating the number of droplets on the number of layers

The effect of modulating the number of droplets on the number of layers is also investigated.

Figure 57 shows us an evident variation in the total number of layers concerning the number of droplets. We drop-casted the ethanol-based solution of 2H-WSe₂ on Si/SiO₂ substrate to observe if we obtain a lesser number of layers for lesser droplets and more number of layers for a greater number of droplets. Starting from 2 droplets, we obtained 2 layers of 2H-WSe₂ ($\sim 1.7 \pm 0.3$ nm). Increasing the number of droplets to 8 and 12 gave us consecutive height profiles of $\sim 5.5 \pm 0.3$ nm (indicating $\sim 6L$) and $\sim 11 \pm 0.3$ nm (indicating $\sim 13L$), respectively. We also performed a similar measurement for exfoliation and drop-casting of 2H-WSe₂ at

37 kHz, which provided us a similar variation. For 1h sonication of 2H-WSe₂ in ethanol at 37 kHz showed 14.0 nm (indicating ~16L) for only 2 droplets of the drop-casted 2H-WSe₂. This supported the fact that at lower frequencies and lower exfoliation times, the layers of 2H-WSe₂ are still quite agglomerated. Higher sonication times of ~8h provided the corresponding values of: ($\sim 1.003 \pm 0.3$ nm for 2 droplets (indicating ~ 2L), $\sim 4.0 \pm 0.3$ nm for 8 droplets (indicating ~5L) and $\sim 15 \pm 0.3$ nm for 12 droplets (indicating ~ 17L) for 2H-WSe₂ (as shown in Figure 58). So, we can assume that at the workable frequency of 59 kHz and ~8h exfoliation led us to approximately 2L for 2 droplets, ~5-6L for 8 droplets, and ~13-17L for 12 droplets in our gas-sensing experiments. This helps us assume that a variation in the number of droplets will lead to an almost controllable variation in the total number of WSe₂ layers drop-casted onto the substrate. Such a variation in the resulting gas-sensing measurements are discussed further in the following sections.

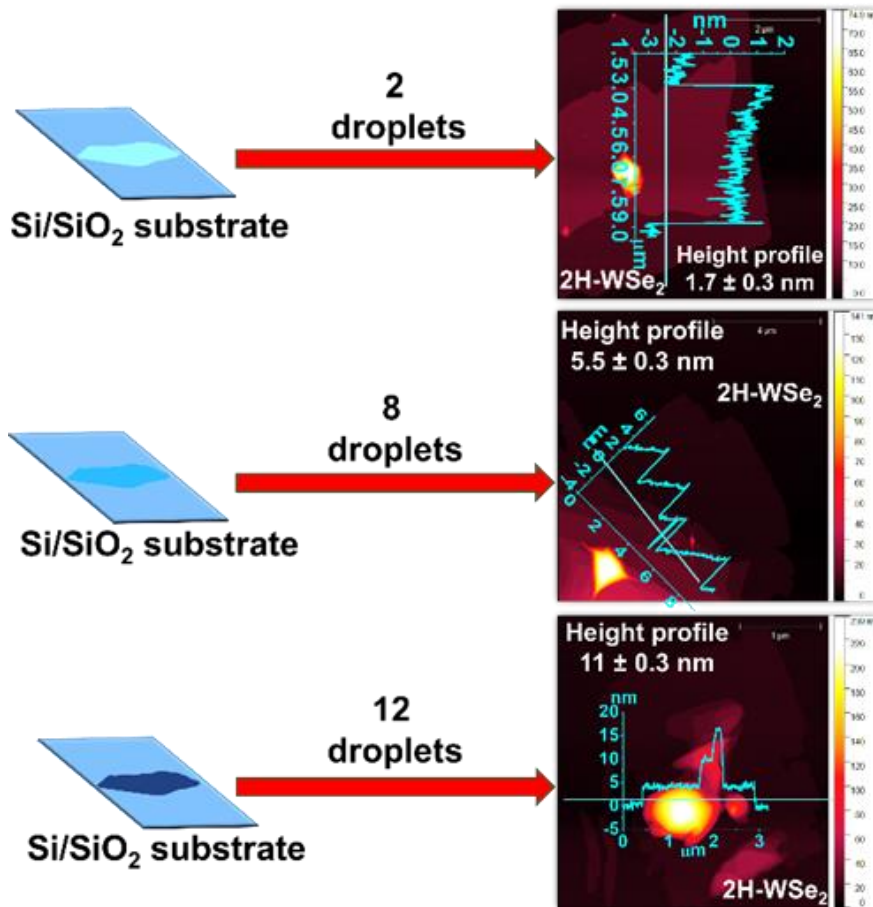


Figure 57. Variation in droplet size starting from 2 droplets to 12 droplets producing variable layers on liquid-phase exfoliation of 2H-WSe₂ in ethanol at 80 kHz.

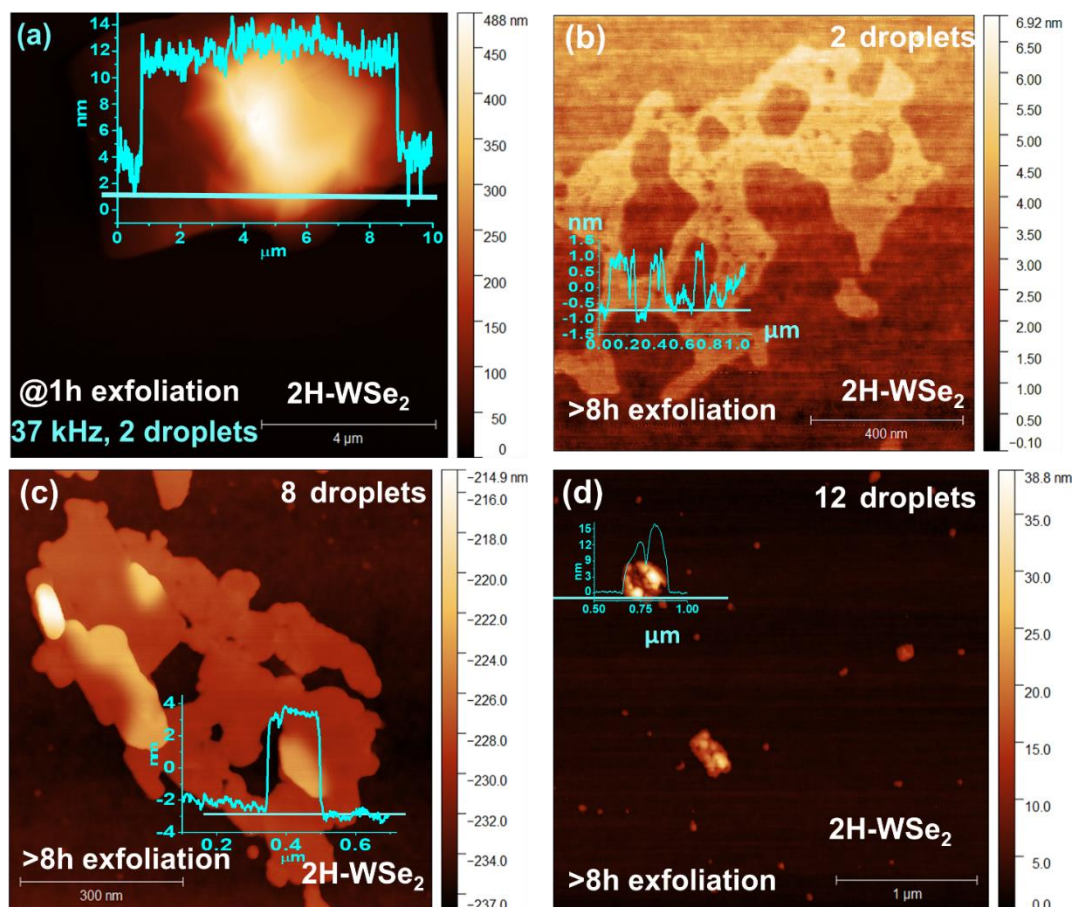


Figure 58. AFM images of 2H-WSe₂ flakes/sheets with variation in (a) 2 droplets, WSe₂ sonicated for 1h at 37 kHz (Height profile: 14.0 nm), (b) 2 droplets, WSe₂, 37 kHz, 8h, (Height profile: 1.0 nm), (c) 8 droplets WSe₂, 37 kHz, 8h, (Height profile: 4 nm) and (d) 12 droplets, WSe₂, 37 kHz, 8h, (Height profile: 15 nm) all at 100 % power representing ~ 16L, ~2L, ~5L and ~17L in each case respectively.

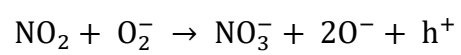
6.5. Gas sensing properties

6.5.1. Sensing mechanism towards NO₂ gas

The sensing mechanism of the 2H-WSe₂ based conductometric sensors can be explained by the surface reaction induced charge transfer through gas molecules adsorption. This induced charge transfer leads to a change in the sensor's conductance. The charge transfer characteristics is mainly controlled by factors such as donor/acceptor characteristics of gas molecules regarding their oxidizing or reducing property and the inherent conductivity type of the semiconducting material (n-or p-type) used for such studies. The sensing mechanism

of p-type WSe₂ semiconductors under NO₂ exposure is described in Figure 59. This mechanism explicitly consists of two consecutive surface reactions, starting with oxygen adsorption coming from ambient air and followed by NO₂ molecules adsorption. Adsorption of oxygen molecules usually takes place on the exposed surface. Oxygen takes electrons from the valence band of WSe₂, creating a hole accumulation region (HAR- positive charge carriers) as represented by equation (18) and described by Figure 59(b) [42,205]. We should note that the sensors are tested at working temperatures below 200 °C, ranging from RT to 150 °C. Therefore, the O₂ that was absorbed was similar to a molecular species (O₂⁻) [205]. The injection of the NO₂ modifies the HAR. due to combined effects such as electron affinity of NO₂, physisorption/chemisorption rate, and 2H-WSe₂ defect sites, mostly Se vacancies. As an oxidizing gas with high electronic affinity, NO₂ is an electron-acceptor that could capture more electrons from the 2H-WSe₂ surface (equation (19) and Figure 59(a)) as well as interact with pre-adsorbed oxygen to form NO₃⁻ (equation (20) and Figure 59(c)) [42]. In both cases, as the NO₂ adsorption process continues, the holes' density increases, and HAR. becomes more concentrated in holes, thereby increasing electrical conductance. In transition metal di-chalcogenides, especially in transition metal di-selenides, defects such as Se vacancies (usually denoted as V_{Se}) have a critical fundamental rule in sensing mechanism towards gas molecules species contribute to carrier charge transfer. It is confirmed from previous reports that the adsorption of NO₂ on the 2H-WSe₂ surface is considered to be unfavorable without the existence of chalcogen vacancies (V_{Se}) [206]. Therefore, V_{Se} behaves as active sites and provides a high chemical activity to the adsorbed molecules such as NO₂, which can tune further HAR, impacting the electrical conductance and the final response [207].





Eq 20

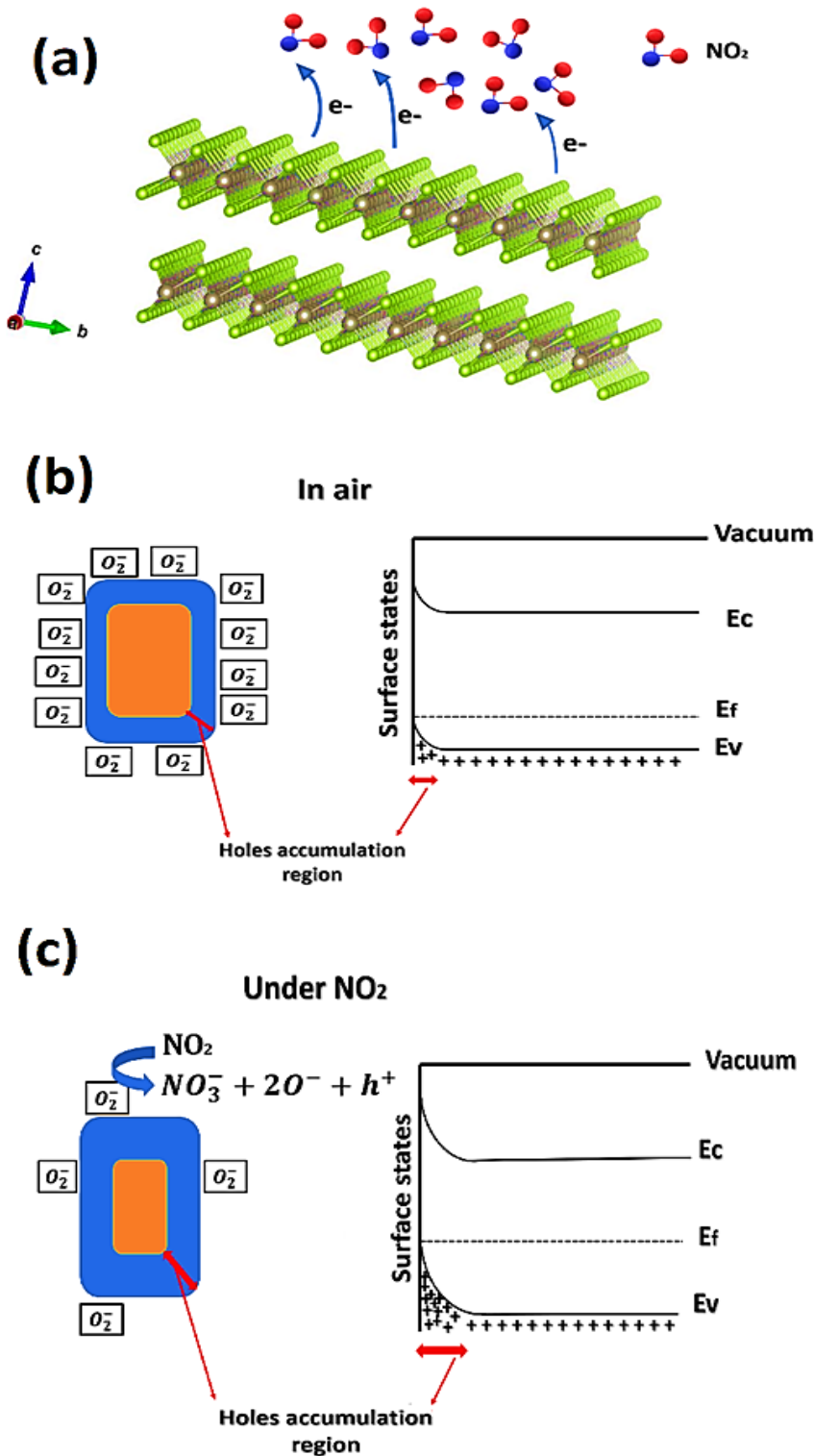


Figure 59. The gas sensing mechanism of p-type 2H-WSe_2 semiconductor nanosheet; (a) the reaction of NO_2 with 2H-WSe_2 at the surface. (b) Diagram energy describes the adsorption of oxygen (in the air) on a 2H-WSe_2 nanosheet. (c) Diagram energy describes the adsorption of NO_2 on 2H-WSe_2 nanosheet, where E_c is the conduction band, E_v is the valence band, and E_f is the Fermi level.

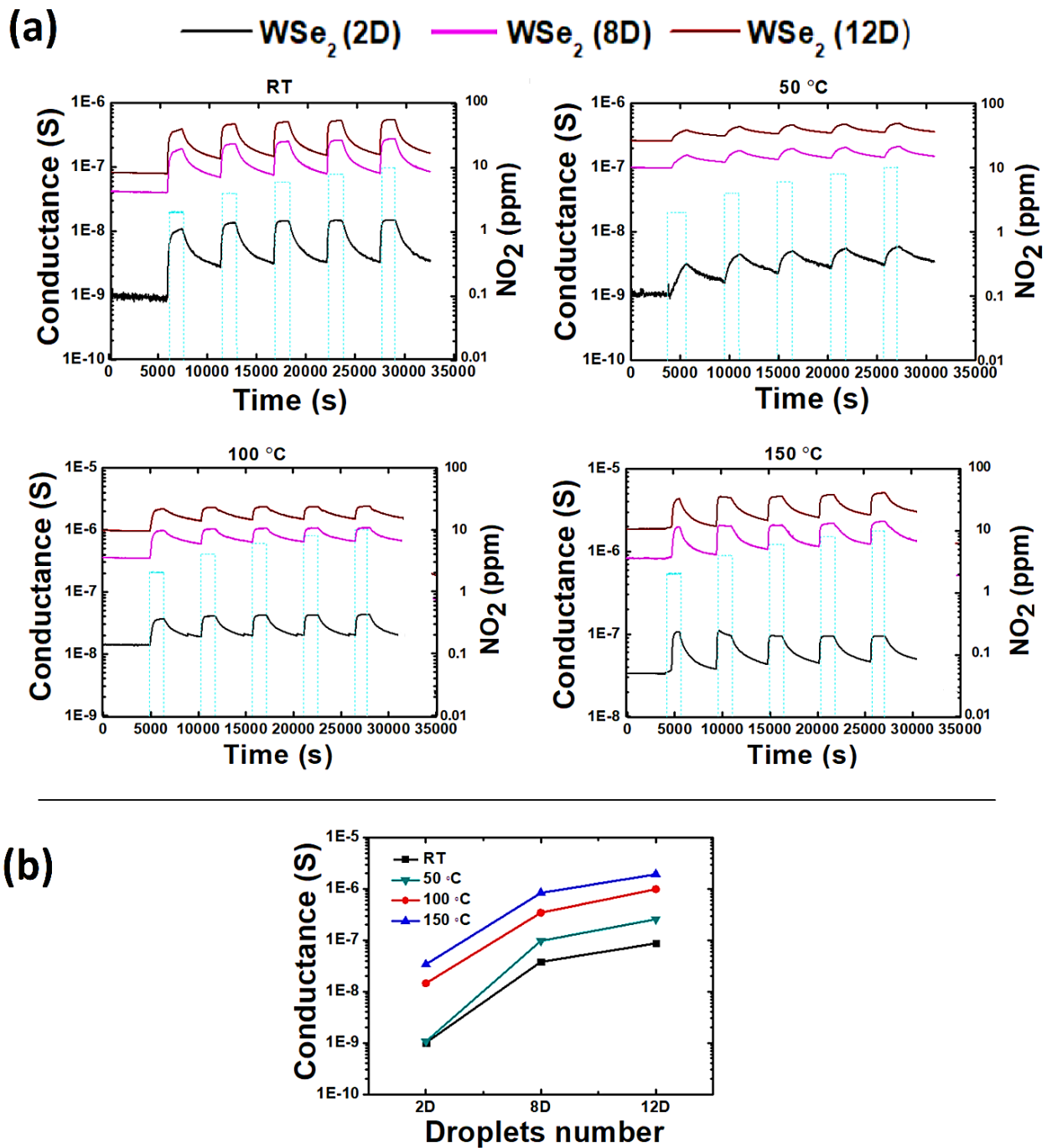
6.5.2. The response towards NO_2 

Figure 60. (a) Dynamic response of 2H-WSe_2 (2D), 2H-WSe_2 (8D) and 2H-WSe_2 (12D) sensors at different temperatures (RT, 50 °C, 100 °C, and 150 °C); (b) The evolution of electrical conductance of the three sensors versus droplets number.

As already explained before, tungsten di-selenide is not thermally stable at temperatures beyond 200 °C and longer oxidation times (>12h) due to the ambient oxidation of 2H-WSe₂. Therefore, all sensors were tested at lower temperatures, which is advantageous for developing low power consumption devices. Figure 60(a) and Figure 60(b) exhibits the dynamic response towards NO₂ and the electrical conductance of WSe₂ (2D), WSe₂ (8D), and WSe₂ (12D) at working temperature (WT) ranging from RT to 150 °C. The three as-fabricated sensors' conductance increases with the working temperature, which confirms the semiconducting nature of the synthesized 2H-WSe₂ nanosheets. After NO₂ exposure, the sensors electrical conductance increased up to a maximum value. After switching off NO₂, the sensors return to the initial value as airflow is restored regardless of the thickness (or the number of layers) formed by drop-casting. This behaviour is consistent with the sensing mechanism of p-type semiconductors towards oxidizing gases. The electron-acceptor property of NO₂ upon interacting with p-type semiconductor causes electrons extraction from the valance band, enhancing the holes carrier concentration and leading to high electrical conductance, as explained in the previous sections. There is incomplete recovery of WSe₂ sensors at RT. Indeed, after increasing the temperature from 50 °C to 150 °C, the recovery rate of the sensors becomes faster. The conductance recovers the baseline in response to the thermal energy that increases the reaction's kinetics (desorption /adsorption rate), which allows full desorption of the NO₂ molecules, and in turn, drastically improves the recovery of these sensors [208].

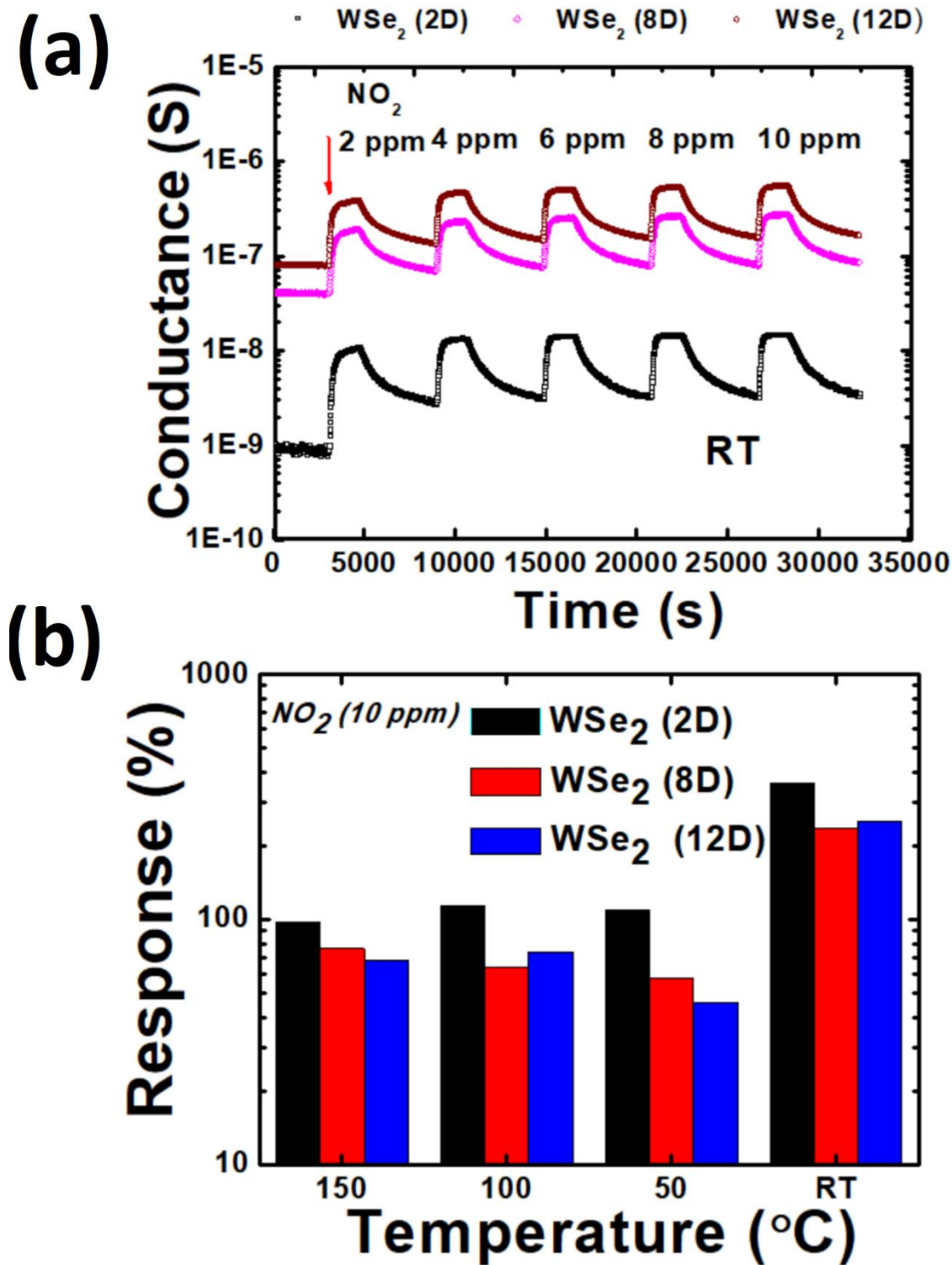


Figure 61. (a) Dynamic response of 2H-WSe₂ (2D), 2H-WSe₂ (8D) and 2H-WSe₂ (12D) sensors at room temperature; (b) The responses of the three sensors towards 10 ppm of NO₂ at different temperatures (RT, 50 °C, 100 °C and 150 °C).

The role of the total number of droplets (number and the total thickness of the layers) used while conducting experiments on sensing properties are investigated. Figure 61(a) shows the dynamic responses of the different 2H-WSe₂ layers towards 10 ppm of NO₂ at RT, while Figure 61(b) shows their responses. The responses increased as the working temperature decreased from 150 °C to RT. The response of the bilayer 2H-WSe₂ (2D) sensor upon 10 ppm of NO₂ was 361 %, 114 %, 113 % and 97.9 % when it was tested at RT, 50 °C, 100 °C and 150 °C, respectively. The high response obtained at RT are attributed to possible selenium vacancies. This happens because, on a broader note, the defect sites created in metal di-chalcogenide, such as in the case of di-sulphides or di-selenides (S or Se), participate primarily in gas molecules adsorption reactions. Previous DFT studies confirmed that the adsorption of N₂ molecules on MoS₂ is negligible in the absence of di-sulphides vacancies (VS₂) [209]. Thus, these defects are essential at low temperatures as N₂ molecules deplete the material carrier charge through the VS₂ and change the electronic conduction.

6.5.3. The response towards NO₂, NH₃ and H₂S

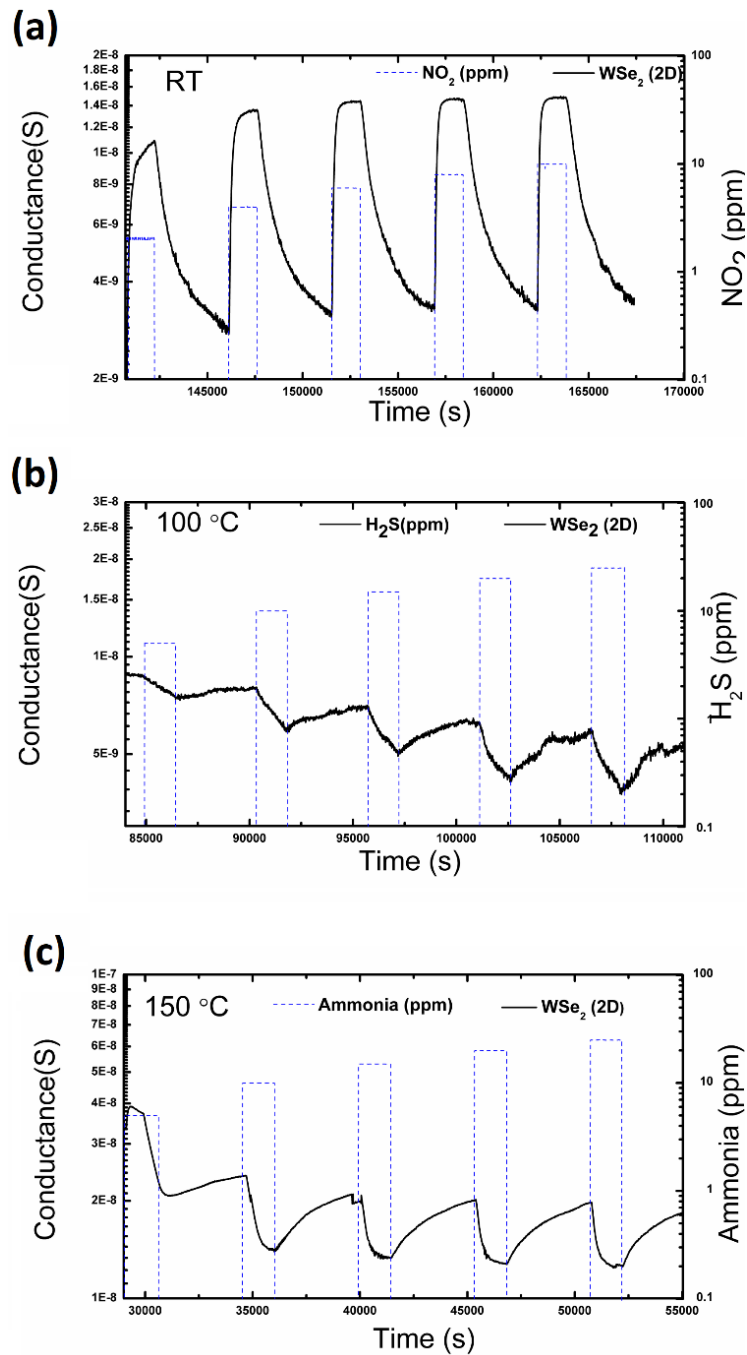


Figure 62. (a) (b) (c) Dynamic response of 2H-WSe₂ (2D) towards NO₂ (2 ppm to 10 ppm) at RT, H₂S (5 ppm to 25 ppm) at 100 °C, H₂S (5 ppm to 25 ppm) at 150 °C, respectively.

The three sensors (WSe_2 (2D), WSe_2 (8D), and WSe_2 (12D)) shows the highest responses at room temperature. Especially, bi-layered 2H- WSe_2 based sensor (WSe_2 (2D)), which has a thickness of around 1.7 nm (thereby indicating 2 flakes or 2 sheets), shows the highest response compared to the sensors containing a greater number of layers (5.5 nm for eight droplets and 11 nm for twelve droplets). Therefore, it can be inferred that the electronic properties in 2H- WSe_2 are thickness dependant. Decreasing the overall thickness leads to the higher surface to volume ratio, which increases the gas molecule adsorption leading to a higher response. Indeed, the high surface to volume ratio of the WSe_2 (2D) sample is due to the bilayer formed by drop-casting two droplets.

In contrast, eight and twelve droplets probably lead to a bulk-like formation (more than eight layers) with a low surface to volume ratio [77,210,211]. Such observations were reported previously by Qiyuan He et al., who investigated the effect of the thickness of MoS_2 on the NO_2 response in a flexible transistor, showing a sensitivity improvement towards NO_2 when the thickness decreased from 18 to 2 nm due to the increase in surface area at low thickness [212]. Late et al. reported synthesizing different MoS_2 layers (L) ranging from 3L to 5L, corresponding to the thickness ranging from 1.4 to 3.3 nm. The high response towards both reducing and oxidizing gases such as NO_2 and NH_3 was achieved for 5L MoS_2 [210]; therefore, a direct link connecting the thickness (number of the layers) of the two-dimensional material and sensing mechanism is still under consideration and needs further investigation and development. The dissimilarity of thickness/response dependency is attributed to two factors that can affect sensor functionality: 1) without taking into account the thickness of the multilayers constructed, increasing the layers is prominent for a high response since the creation of more interspaces provides higher gas molecules intercalation between the layers leading to high sensitivity, as the gas is likely to be intercalated in the layer-layer interface [213], and 2) single or bilayer promote high surface to volume ratio, which increases the adsorption rate resulting in a higher response. However, if we rely on

the second factor in the case of bilayer 2H-WSe₂, even the interlayer spacing is considered as a sub-factor for sensor functionality [214].

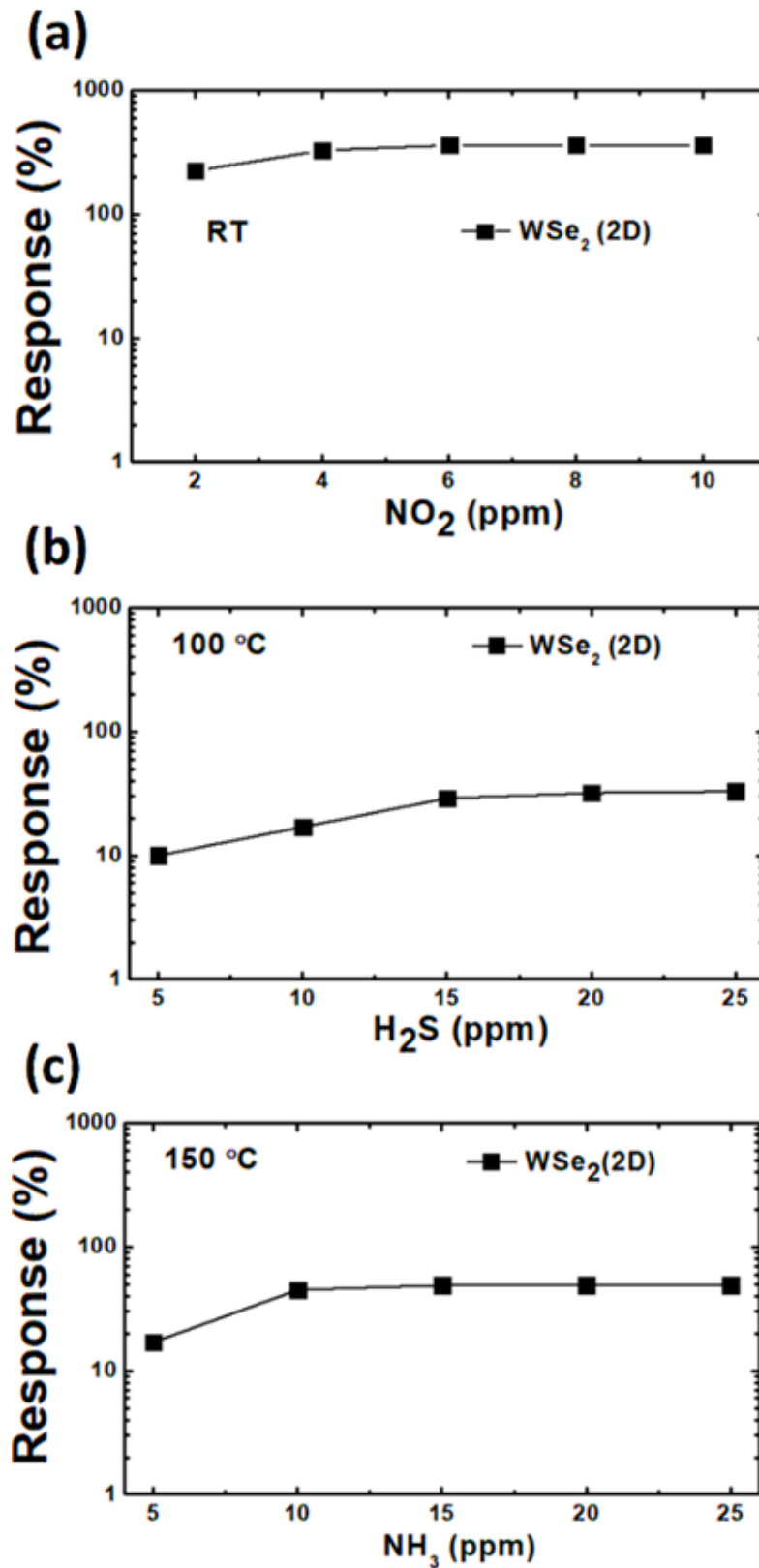


Figure 63. (a), (b), (c) Response (%) of the WSe_2 (2D) sensor towards NO_2 at RT, H_2S at 100 °C, and NH_3 at 150 °C, respectively.

In addition to the above investigations, the sensing performance of 2H-WSe₂ was also studied towards other gases such as NH₃ and H₂S. These gases are also of particular interest in our case because of the many devastating effects they pose on human health and the environment. Figure 62 shows the dynamic response of the 2H-WSe₂ (2D) sensor towards NO₂ (2 ppm to 10 ppm), H₂S (5 ppm to 25 ppm) and NH₃ (5 ppm to 25 ppm), respectively. The best working temperatures for high detection of NH₃ are 150 °C, whereas 100 °C is optimal for H₂S, and, as already discussed, RT for NO₂. It is worth noting that even the working temperature of 150 °C satisfies the low power consumption of 2H-WSe₂ nanosheets-based sensors. As shown in the dynamic response, the electrical conductance decreases on NH₃ and H₂S exposure. This behavior is primarily due to the electron-donor nature of reducing gases such as NH₃ and H₂S. During the interaction of these gases with p-type material, the reducing compounds provide or re-inject the electrons into materials instead of extracting the latter as with NO₂. The injected electrons recombine with holes reducing the density of holes carriers and decreasing the electrical conductance of p-type material [215,216]. The electrons transfer induced by reducing gases oppositely affects the holes-carriers concentration compared to oxidizing gases. Figure 63(a) shows the response against NO₂ concentrations. The response upon NO₂ exposure increased stepwise from 250 % to 361 % when the concentration was increased from 2 to 6 ppm, reaching the maximum response at the critical concentration (8 ppm) and creating an enhanced sensor surface interaction. Followed by increasing the NO₂ concentration at 10 ppm, the surface was fully covered with NO₂ molecules, which excludes new NO₂ molecules' possibility of reacting with the surface due to the saturation level [217]. Therefore, the response remained stable (unchangeable) upon exposure to 10 ppm. The response saturation is also investigated in many reports. This usually happens when the sensor is operating at low temperature (as per our RT investigations), and it is attributed to the molecular adsorption, which sometimes leads to a poisoning effects in the sensor if no kinetic energy (UV or heat)

is applied to overcome the issue of the gas molecules detaching from the surface [218,219]. The high response towards 2 ppm and the response stability at/from 6 ppm of NO₂ shows the ability to detect NO₂ at lower concentration (even at ppb level). As shown in Figure 64, the bilayer 2H-WSe₂ can sense even 200 ppb (0.2 ppm) of NO₂ gas. Ideally, 200 ppb is considered as the experimental detection limit as well as the threshold exposure limit of NO₂ recommended by American Conference of Governmental Industrial Hygienists [220,221]. In fact, an ideal NO₂ sensor should have a practical limit of detection (LOD) equal to or lower than this value. Our results hold a high significance in many medical applications, such as utilizing chemical gas sensors in breath analyzers of the human exhaled breath where NO₂ is considered a biomarker for early diagnosis of asthma prediction and its associated risks. In the case of asthma detection from human exhaled breath, monitoring the exhaled breath requires detecting an extremely low concentration of NO₂ in the presence of a high relative humidity level (higher than 70%), which makes our study very important, utilizing exfoliated 2H-WSe₂ as a promising NO₂ sensing TMDC.

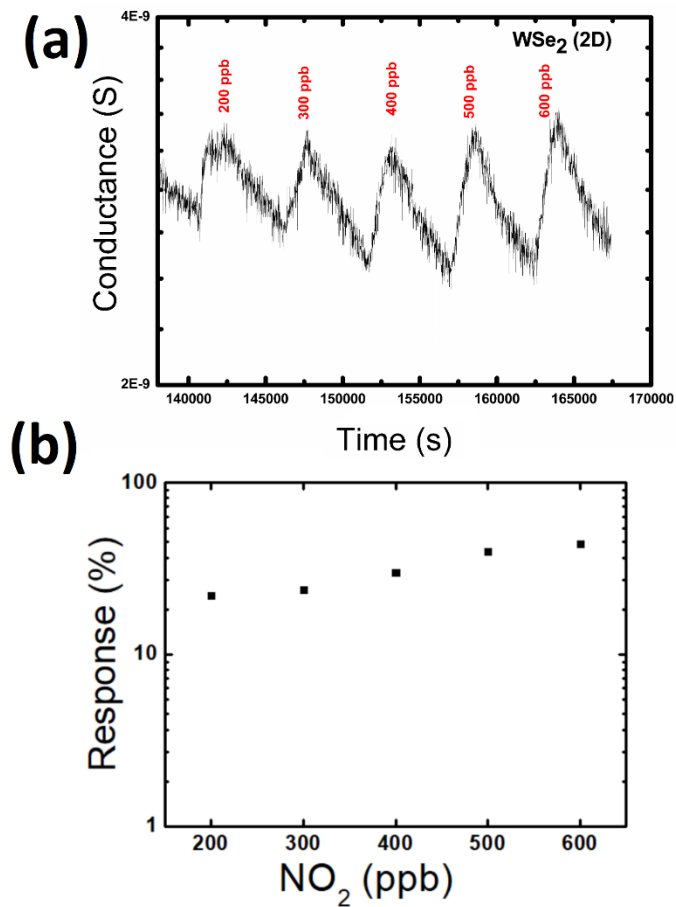


Figure 64. Dynamic response of the 2H-WSe₂ (2D) sensor towards a low concentration of NO₂ (200 ppb, 300 ppb, 400 ppb, 500, and 600 ppb) at RT.

6.5.4. Selectivity, humidity effect and long-term stability studies towards NO₂ at room temperature.

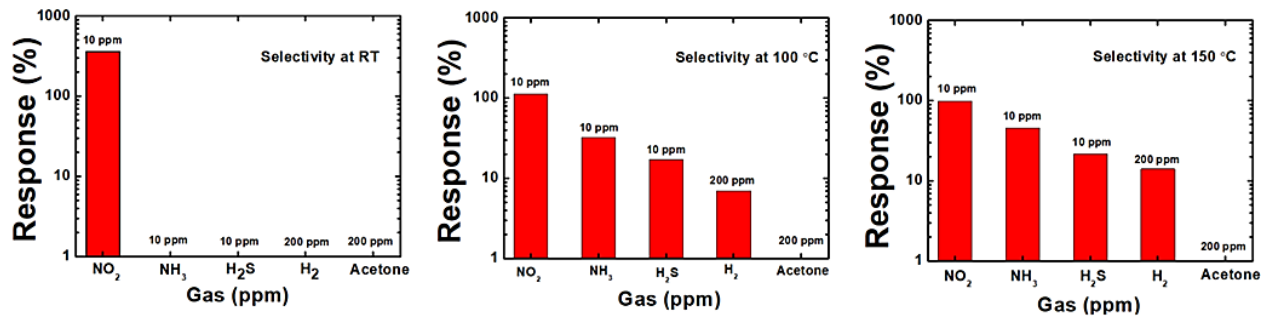


Figure 65. Selectivity of 2H-WSe₂ (2D) sensor towards NO₂ (10 ppm) over H₂ (200 ppm), acetone (10 ppm), NH₃ (10 ppm), and H₂S (10 ppm) at different temperatures (RT, 100 °C and 150 °C).

The response towards H₂S increased from 10 % to 33 % when the concentration increased from 5 ppm to 25 ppm and increased from 17 % to 49 % upon NH₃ exposure maintaining the same NH₃ concentration range as H₂S (Figure 63(b) and Figure 63(c)). Moreover, the limit of detection (LOD) was also calculated. To estimate the LOD of the sensor, the experimental data are fitted using the power law. LODs towards NO₂, H₂S and NH₃ are about 100 ppb, 4829 ppb and 1561 ppb, respectively.

A comparison of obtained sensing performance toward some studies reported in the literature on 2H-WSe₂ based NO₂ sensor is summarized in Table 12.

Table 12. NO₂ sensing performances of 2H-WSe₂

Material	Structure	NO ₂ (ppm)	Temperature (°C)	Response	Ref.
WSe ₂	Porous 3D WSe ₂	10	150	150% ^a	[222]
NbSe ₂ /WSe ₂	Film	5	NA	34% ^b	[223]
Au/WSe ₂	Film	5		10% ^b	[223]
WSe ₂	Nanosheets	10	RT	1101% ^a	[221]
WSe ₂	3 layers	10	RT	162% ^b	[224]
WSe ₂	Films	5	RT	0.4 % ^b	[225]
WSe ₂	Nanolayer	10	RT	1000% ^{NA}	[226]
2H-WSe ₂	<i>Bilayer</i>	<i>6 ppm</i>	<i>RT</i>	<i>361%^b</i>	<i>This work</i>
	<i>Nanosheets</i>	<i>4 ppm</i>		<i>328%^b</i>	
		<i>2 ppm</i>		<i>265%^b</i>	

Note: a) Response (%) = $R_{air}/R_{gas} \times 100$, or; b) Response (%) = $(\Delta/I \times 100, \Delta R/R \times 100, \text{ or } \Delta G/G \times 100)$; NA = not available

To investigate the selectivity of the 2H-WSe₂ sensor, we tested the bilayer 2H-WSe₂ (2D) towards fixed concentrations of different gases such as H₂, NH₃, acetone, and H₂S. The selectivity was studied at three temperatures: 150 °C, 100 °C, and RT, as shown in Figure 65. The 2H-WSe₂ (2D) showed a full selectivity towards NO₂ at room temperature. Indeed 2H-WSe₂ is entirely insensitive to the other gases. By heating the sensor at 100 °C and even

at 150 °C, the response was slightly increased towards other gases, especially NH₃ and H₂S. Despite this, the 2H-WSe₂ sensor remains selective to NO₂. Moreover, the long-term stability of 2H-WSe₂ (2D) was also investigated, as shown in Figure 66. The sensor offers good stability towards low concentration of NO₂ even after 9 months. It is worth noting that many measurements towards several gases at different temperatures are performed as a long-term study, all of which show the high stability of 2H-WSe₂ in detecting low NO₂ concentration (2 ppm). Besides, the estimated response and recovery times of bilayer 2H-WSe₂ (2D) towards NO₂ concentrations (2, 4, 6, 8, 10 ppm) is calculated and illustrated in Figure 67. The sensor also shows a fast response and fast recovery time (220 s and 1700 s, respectively) at RT, based on the fact that the response and recovery times of sensor are limited only to the filling time of the test chamber (approximately 4–5 min to fill the 1L test chamber). Finally, the effect of humidity on the NO₂ (2 ppm) response are also studied by changing the relative humidity (RH) from 20% to 90 % at room temperature (Figure 68). As can be seen, the sensor is sensitive even at a high humidity level (90 %), which also proves the sensors' suitability for diagnostics in exhaled breath analysis, where real-time applications often require high humidity near the normal exhaled breath (80 % to 90 %).

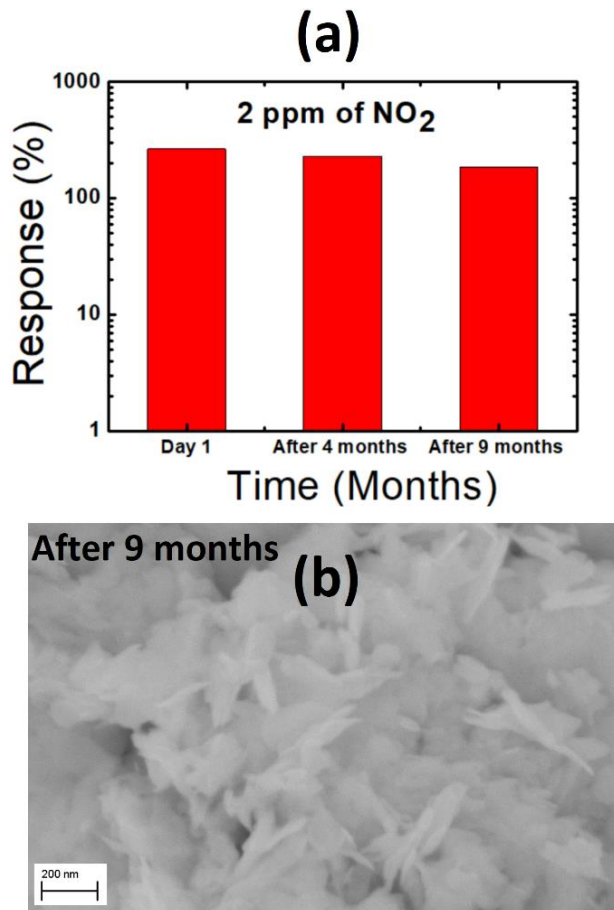


Figure 66. (a) Long-term stability of the 2H-WSe₂ (2D) sensor towards NO₂ (2 ppm) at RT, (b) Scanning Electron Microscopy (SEM) image of 2H-WSe₂ flakes after 9 months.

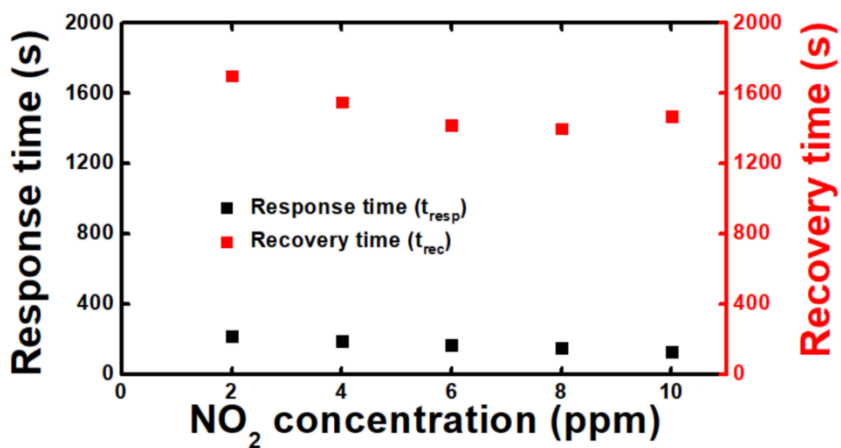


Figure 67. Response and recovery times of the 2H-WSe₂ (2D) sensor towards NO₂ (2 ppm to 10 ppm) at RT.

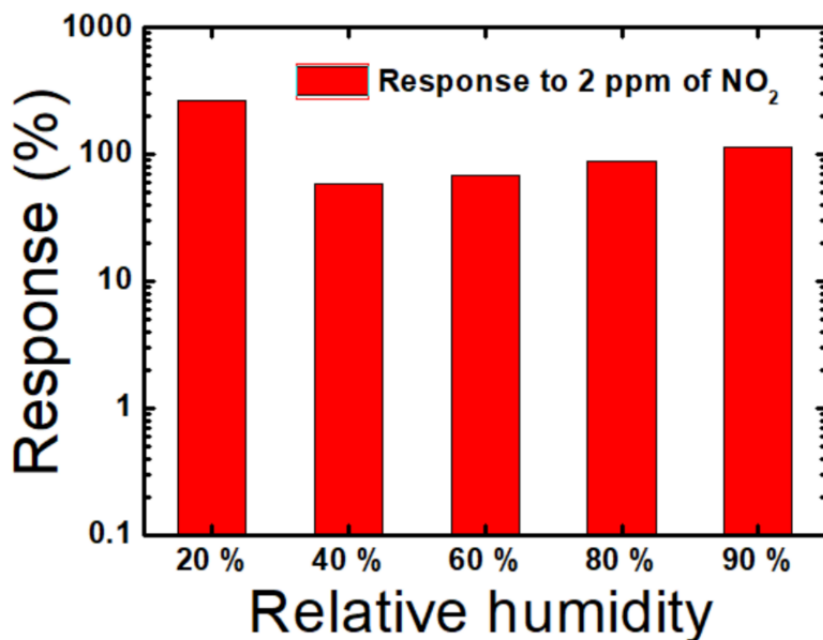


Figure 68. The effects of relative humidity on the NO₂ response of 2H-WSe₂ (2D) sensor (ppm).

Conclusion

This chapter investigated a room temperature sensor based on WSe₂ nanosheet as an example of a new class of semiconductor TMDC materials. A simple liquid-assisted exfoliation of 2H-WSe₂ was prepared using ambient pressure chemical vapor deposition (APCVD). The stability of 2H-WSe₂ in different solvents has been proved. The gas sensing mechanism of 2H-WSe₂ nanosheets was investigated. Two-layer WSe₂ nanosheets deliver the best gas sensor performances compared to 6 layers and 13 layers. The sensor showed nearly the same response toward low NO₂ concentration even after 9 months of testing, confirming its remarkable long-term stability. High stability at high relative humidity levels has been observed. A selectivity study, performed at three working temperatures (RT, 100, and 150 °C), shows high selectivity at 150 and 100 °C. Full selectivity toward NO₂ at RT

confirms that 2H-WSe₂ nanosheet-based sensors are ideal candidates to detect this chemical compound.

Conclusions

The main objectives of this PhD research were to fabricate nano-conductometric gas sensors with enhanced sensing performances such as good response, high stability good selectivity and short response and recovery times, based on 1D metal oxides (1D MOX) and 2D transition metal dichalcogenides (2D TMDC) nanomaterials using vapor phase growth. These objectives have been achieved by synthesis 1D ZnO nanostructures, high quality of Bi₂O₃ nanowires and well-controlled layered 2H-WSe₂ nanosheets with high purity and good morphological properties. Indeed, the overall work can be summarized as follow:

In the first study, we investigated the effect of the catalyst in the Vapor Liquid Solid (VLS) growth of one-dimensional ZnO (1D ZnO) together with its effect on chemical sensors performances. The 1D ZnO nanostructures were successfully prepared using a vapor phase growth and catalyst (Au, Pt and Ag and Cu) supported growth following VLS mechanism. The morphological, structural and electrical properties of the 1D nanostructures were studied. Depending on catalyst nature, different geometry, size and nanowires/nanorods abundance of ZnO were obtained. A morphology transition from nanowires to nanorods was observed using Au catalyst by increasing the deposition temperature and maybe explained by the coalescence effect of the Au catalyst seeds. ZnO crystallizes in hexagonal phase, while catalysts particles were shown in its metallic (Au, Pt and Ag) or oxidized (CuO) form. ZnO (Au) nanowires and nanorods, ZnO (Pt) nanowires and ZnO (Cu) nanowires structure have (002) as preferred orientation. While, for ZnO (Ag) nanowires, both (010) and (002) are considered as the preferential direction of due to their almost identical TC values. The 1D ZnO nanostructures were tested under several reducing gases at several working

temperatures. ZnO nanostructures synthesized using different catalysts towards H₂ at several working temperatures: 200 °C, 300 °C, 350 °C, 400 °C and 500 °C. ZnO (Au) nanowires and nanorods showed the best response to H₂ at 350 °C. ZnO (Au) showed high response, good stability and selectivity to H₂ with small response and recovery time, demonstrating its possible use for low-cost fabrication of high-performance chemical sensors. The signal is stable and recovering perfectly to the baseline level showing good stability. Moreover, the ZnO (Au) nanowires was able to detect low H₂ concentration (50 ppm) with good repeatability. The response time was found to be similar for ZnO NWs and NRs (about 1200 s), while ZnO NWs showed a short recovery time (100 s). Selectivity has been observed towards hydrogen over other reducing gases. Most importantly, the effect of catalysts (Au, Pt, Ag and Cu) used in VLS for the growth on gas sensor mechanism was discussed. Moreover, a new approach explaining the role of catalysts in enhancing conductometric sensors characteristics was presented, such as the chemical sensitization (spillover effect) due to the gold nanoparticle on the tip of the ZnO.

For α -Bi₂O₃ nanowires, we followed the same VLS mechanism as for ZnO, but the main aim is to get pure as well as high quality of nanowires to study their capability for breath analysis applications. Indeed, we have described the synthesis of p-type α -Bi₂O₃ nanowires, tested and explained its sensing properties. VLS mechanism was confirmed by the formation of Au nanoparticles on the top of nanowires. Pure α -Bi₂O₃ without impurities were achieved, the synthesized nanowires showed an average diameter of 100 nm and 6 μ m as length. The effect of gold nanoparticles on sensing performances and the mechanism of α -Bi₂O₃ was investigated. In this study, we proposed a new approach linking synthesis mechanism with improvement in sensing performances. It was proposed by considering VLS as (1) the growth mechanism of p-type α -Bi₂O₃ and (2) promoting an extra chemical sensitization (spillover effect) by means of Au catalysts. The detection capability of α -Bi₂O₃ toward low concentrations of acetone

and ethanol was proved, humidity effect, stability, repeatability, sensor kinetic and selectivity were investigated. The responses of bismuth oxide were 34.1 and 2.9 to 40 and 10 ppm of ethanol and acetone, respectively. Stable response of α - Bi_2O_3 under 2 ppm of acetone in the presence of different relative humidity levels ranging from 50 to 90 % was achieved. This is a remarkable result, not so common as MOX are concerned. The sensors also showed response and recovery times of 130 s and 212 s, respectively, towards 2 ppm of acetone at high humidity level (90%). Very good long-term stability (50 days) and good selectivity to acetone and ethanol over ammonia, hydrogen, carbon monoxide, NO_2 and CO_2 were achieved. Finally, α - Bi_2O_3 nanowires show excellent conductometric sensor performances proving their potentialities in the development of breath sensors for diabetes diagnosis. In fact, real-time measurements of acetone and ethanol in breath is still challenging since in exhaled breath more than 400 chemical compounds are present. Therefore, it is difficult to have full selectivity towards one or two compounds over the others considering the huge number of analytes. However, the first step consists of the synthesis of a material that is highly sensitive to acetone having low or zero cross-sensitivity to other analytes present in breath. Therefore, our study is a starting point for investigating the possible production of a real-time sensor for breath analysis based on α - Bi_2O_3 nanowires. Moreover, noble metals (Au and Ag) and metal oxides (TiO_2) nanoparticles (NPs) -functionalized α - Bi_2O_3 nanowires have been investigated for hydrogen detection. TiO_2 nanoparticles functionalisation showed the greatest effect on hydrogen sensing performances. TiO_2 - α - Bi_2O_3 exhibits a great enhancement toward 500 ppm of H_2 at 350 °C with a 25-fold higher response compared with α - Bi_2O_3 .

In the third study, we proposed a scalable synthesis and profoundly simple approach of integrating 2H-WSe₂ nanosheets (prepared as per an ambient pressure CVD process) for highly sensitive, stable, and fully selective NO_2 sensor at room temperature were thoroughly investigated. The liquid phase exfoliation of 2H-WSe₂ nanosheets from the WSe₂ bulk,

additionally, allows the smooth homogenous dispersion of the material in a suitable solvent (both ethanol and isopropanol in our case), which was relatively stable up to 60 days. The integration of 2H-WSe₂ nanosheets is realized by the drop-casting with variable number of repetitions (2, 8, and 12 droplets). The as-prepared sensors showed a higher response at RT compared to 50 °C, 100 °C, and 150 °C. The gas sensing properties depends on the number of layers. Two droplets (2L) sensors have the highest response and selectivity towards NO₂ at RT (250 %, 328 %, and 361 % towards 2 ppm, 4 ppm, and 6 ppm of NO₂, respectively). 2H-WSe₂ sensors show excellent, reliable, and high stability (up to 9 months) towards NO₂. The sensors are not sensitive towards H₂, NH₃, H₂S, and acetone. It is, in fact, selective to NO₂ at room temperature (RT). These results demonstrated an inherent and extraordinary capability of 2D layered 2H-WSe₂ towards active and highly selective monitoring of NO₂ gas.

In summary, many chemical sensors based on different materials have been prepared during this PhD thesis, and all these devices have shown excellent sensing performances towards chemical compounds.

Along with this pursuit, we aim to further investigate the effect of functionalization of α -Bi₂O₃ with different metal and metal oxide nanoparticles on the sensing performances of α -Bi₂O₃ such as study the effect of humidity, investigating the the response towards other gases and examine the long term stability of these devices. We will focus also on the synthesis of composite materials such as Bi₂O₃_WSe₂ and ZnO _WSe₂ and investigate their capability in chemical sensors as well as in other applications such as batteries.

References

- [1] I. Union, O.F. Pure, A. Chemistry, COMMISSION ON GENERAL ASPECTS OF

ANALYTICAL CHEMISTRY * CLASSIFICATION AND CHEMICAL

CHARACTERISTICS OF IMMOBILIZED Classification and chemical characteristics of, 67 (1995) 597–600.

- [2] W. Wang, Introductory Chapter: What is Chemical Sensor?, *Progresses Chem. Sens.* (2016) 3–8. <https://doi.org/10.5772/64626>.
- [3] G. Korotcenkov, V. Brinzari, I.A. Pronin, M.H. Ham, B.K. Cho, Metal oxides for application in conductometric gas sensors: How to choose?, *Solid State Phenom.* 266 SSP (2017) 187–195. <https://doi.org/10.4028/www.scientific.net/SSP.266.187>.
- [4] N. Kaur, M. Singh, E. Comini, One-Dimensional Nanostructured Oxide Chemoresistive Sensors, *Langmuir.* 36 (2020) 6326–6344. <https://doi.org/10.1021/acs.langmuir.0c00701>.
- [5] M.M. Arafat, B. Dinan, S.A. Akbar, A.S.M.A. Haseeb, Gas sensors based on one dimensional nanostructured metal-oxides: A review, *Sensors (Switzerland).* 12 (2012) 7207–7258. <https://doi.org/10.3390/s120607207>.
- [6] P. Vazquez-Roig, Y. Pico, Gas chromatography and mass spectroscopy techniques for the detection of chemical contaminants and residues in foods, Woodhead Publishing Limited, 2012. <https://doi.org/10.1533/9780857095794.1.17>.
- [7] D. Punetha, M. Kar, S.K. Pandey, A new type low-cost, flexible and wearable tertiary nanocomposite sensor for room temperature hydrogen gas sensing, *Sci. Rep.* 10 (2020) 1–11. <https://doi.org/10.1038/s41598-020-58965-w>.
- [8] S. Feng, F. Farha, Q. Li, Y. Wan, Y. Xu, T. Zhang, H. Ning, Review on smart gas sensing technology, *Sensors (Switzerland).* 19 (2019) 1–22. <https://doi.org/10.3390/s19173760>.
- [9] C. Wang, L. Yin, L. Zhang, D. Xiang, R. Gao, Metal oxide gas sensors: Sensitivity and influencing factors, *Sensors.* 10 (2010) 2088–2106. <https://doi.org/10.3390/s100302088>.
- [10] A. Dey, Semiconductor metal oxide gas sensors: A review, *Mater. Sci. Eng. B Solid-State Mater. Adv. Technol.* 229 (2018) 206–217. <https://doi.org/10.1016/j.mseb.2017.12.036>.
- [11] E. Comini, C. Baratto, I. Concina, G. Faglia, M. Falasconi, M. Ferroni, V. Galstyan, E. Gobbi, A. Ponzoni, A. Vomiero, D. Zappa, V. Sberveglieri, G. Sberveglieri, Metal oxide nanoscience and nanotechnology for chemical sensors, *Sensors Actuators, B Chem.* 179 (2013) 3–20. <https://doi.org/10.1016/j.snb.2012.10.027>.
- [12] E. Comini, Metal oxides nanowires chemical/gas sensors: recent advances, *Mater.*

- Today Adv. 7 (2020) 100099. <https://doi.org/10.1016/j.mtadv.2020.100099>.
- [13] N. Kaur, E. Comini, D. Zappa, N. Poli, G. Sberveglieri, Nickel oxide nanowires: Vapor liquid solid synthesis and integration into a gas sensing device, *Nanotechnology*. 27 (2016) 1–9. <https://doi.org/10.1088/0957-4484/27/20/205701>.
- [14] A. Ponzoni, C. Baratto, N. Cattabiani, M. Falasconi, V. Galstyan, E. Nunez-Carmona, F. Rigoni, V. Sberveglieri, G. Zambotti, D. Zappa, Metal oxide gas sensors, a survey of selectivity issues addressed at the SENSOR lab, Brescia (Italy), *Sensors (Switzerland)*. 17 (2017). <https://doi.org/10.3390/s17040714>.
- [15] R.G. Pavelko, A.A. Vasiliev, E. Llobet, X. Vilanova, V.G. Sevastyanov, N.T. Kuznetsov, Selectivity problem of metal oxide based sensors in the presence of water vapors, *Procedia Eng.* 5 (2010) 111–114. <https://doi.org/10.1016/j.proeng.2010.09.060>.
- [16] V. Galstyan, A. Ponzoni, I. Kholmanov, M.M. Natile, E. Comini, G. Sberveglieri, Highly sensitive and selective detection of dimethylamine through Nb-doping of TiO₂ nanotubes for potential use in seafood quality control, *Sensors Actuators, B Chem.* 303 (2020) 127217. <https://doi.org/10.1016/j.snb.2019.127217>.
- [17] N. Kaur, M. Singh, A. Moumen, G. Duina, E. Comini, 1D titanium dioxide: Achievements in chemical sensing, *Materials (Basel)*. 13 (2020) 1–21. <https://doi.org/10.3390/ma13132974>.
- [18] A. Moumen, B. Hartiti, E. Comini, Z. El khalidi, H.M.M.M. Arachchige, S. Fadili, P. Thevenin, Preparation and characterization of nanostructured CuO thin films using spray pyrolysis technique, *Superlattices Microstruct.* 127 (2019) 2–10. <https://doi.org/10.1016/j.spmi.2018.06.061>.
- [19] S. Pirsra, Chemiresistive gas sensors based on conducting polymers, *Mater. Sci. Eng. Concepts, Methodol. Tools, Appl.* 1–3 (2017) 543–574. <https://doi.org/10.4018/978-1-5225-1798-6.ch022>.
- [20] J.H. Choi, J. Lee, M. Byeon, T.E. Hong, H. Park, C.Y. Lee, Graphene-Based Gas Sensors with High Sensitivity and Minimal Sensor-to-Sensor Variation, *ACS Appl. Nano Mater.* 3 (2020) 2257–2265. <https://doi.org/10.1021/acsanm.9b02378>.
- [21] T. Han, A. Nag, S. Chandra Mukhopadhyay, Y. Xu, Carbon nanotubes and its gas-sensing applications: A review, *Sensors Actuators, A Phys.* 291 (2019) 107–143. <https://doi.org/10.1016/j.sna.2019.03.053>.
- [22] J. Park, J. Mun, J.S. Shin, S.W. Kang, Highly sensitive two dimensional MoS₂ gas sensor decorated with Pt nanoparticles, *R. Soc. Open Sci.* 5 (2018) 1–9.

- <https://doi.org/10.1098/rsos.181462>.
- [23] E. Comini, Metal oxide nanowire chemical sensors: innovation and quality of life, *Mater. Today*. 19 (2016) 559–567. <https://doi.org/10.1016/j.mattod.2016.05.016>.
- [24] S.P. Lee, Electrodes for semiconductor gas sensors, *Sensors (Switzerland)*. 17 (2017). <https://doi.org/10.3390/s17040683>.
- [25] S. Saukko, V. Lantto, Influence of electrode material on properties of SnO₂-based gas sensor, *Thin Solid Films*. 436 (2003) 137–140. [https://doi.org/10.1016/S0040-6090\(03\)00509-1](https://doi.org/10.1016/S0040-6090(03)00509-1).
- [26] S.M.A. Durrani, The influence of electrode metals and its configuration on the response of tin oxide thin film CO sensor, *Talanta*. 68 (2006) 1732–1735. <https://doi.org/10.1016/j.talanta.2005.08.015>.
- [27] H. Omran, K.N. Salama, Design and fabrication of capacitive interdigitated electrodes for smart gas sensors, 2015 IEEE Int. Conf. Smart Instrumentation, Meas. Appl. ICSIMA 2015. (2016). <https://doi.org/10.1109/ICSIMA.2015.7559021>.
- [28] H. Esch, G. Huyberechts, R. Mertens, G. Maes, J. Manca, W. De Ceuninck, L. De Schepper, Stability of Pt heater and temperature sensing elements for silicon integrated tin oxide gas sensors, *Sensors Actuators, B Chem*. 65 (2000) 190–192. [https://doi.org/10.1016/S0925-4005\(99\)00301-9](https://doi.org/10.1016/S0925-4005(99)00301-9).
- [29] K. Oblov, A. Ivanova, S. Soloviev, N. Samotaev, A. Vasiliev, A. Sokolov, Fabrication of MEMS platform for sensors applications by laser micro engraving, *Phys. Procedia*. 72 (2015) 475–479. <https://doi.org/10.1016/j.phpro.2015.09.013>.
- [30] L. Chen, M. Mehregany, Exploring silicon carbide for thermal infrared radiators, *Proc. IEEE Sensors*. (2007) 620–623. <https://doi.org/10.1109/ICSENS.2007.4388475>.
- [31] M. Aslam, C. Gregory, J. V. Hatfield, Polyimide membrane for micro-heated gas sensor array, *Sensors Actuators, B Chem*. 103 (2004) 153–157. <https://doi.org/10.1016/j.snb.2004.04.102>.
- [32] N.C. Das, M. Jhabvala, D. Robinson, P. Shu, Low power polysilicon sources for IR applications, *Int. Conf. Solid-State Integr. Circuit Technol. Proc.* (1998) 884–886. <https://doi.org/10.1109/icsict.1998.786499>.
- [33] J.F. Creemer, D. Briand, H.W. Zandbergen, W. van der Vlist, C.R. de Boer, N.F. de Rooij, P.M. Sarro, Microhotplates with TiN heaters, *Sensors Actuators, A Phys*. 148 (2008) 416–421. <https://doi.org/10.1016/j.sna.2008.08.016>.
- [34] J. Dai, O. Ogbeide, N. Macadam, Q. Sun, W. Yu, Y. Li, B.L. Su, T. Hasan, X. Huang,

- W. Huang, Printed gas sensors, *Chem. Soc. Rev.* 49 (2020) 1756–1789.
<https://doi.org/10.1039/c9cs00459a>.
- [35] D. Zappa, V. Galstyan, N. Kaur, H.M.M. Munasinghe Arachchige, O. Sisman, E. Comini, “Metal oxide -based heterostructures for gas sensors”- A review, *Anal. Chim. Acta.* 1039 (2018) 1–23. <https://doi.org/10.1016/j.aca.2018.09.020>.
- [36] G. Korotcenkov, Current trends in nanomaterials for metal oxide-based conductometric gas sensors: Advantages and limitations. part 1: 1D and 2D nanostructures, *Nanomaterials.* 10 (2020) 1–62.
<https://doi.org/10.3390/nano10071392>.
- [37] N. Barsan, C. Simion, T. Heine, S. Pokhrel, U. Weimar, Modeling of sensing and transduction for p-type semiconducting metal oxide based gas sensors, *J. Electroceramics.* 25 (2010) 11–19. <https://doi.org/10.1007/s10832-009-9583-x>.
- [38] V.A. Lavrenko, I.A. Podchernyaeva, D. V. Shchur, A.D. Zolotareno, A.D. Zolotareno, Features of Physical and Chemical Adsorption During Interaction of Polycrystalline and Nanocrystalline Materials with Gases, *Powder Metall. Met. Ceram.* 56 (2018) 504–511. <https://doi.org/10.1007/s11106-018-9922-z>.
- [39] G. Williams, G.S.V. Coles, NO_x response of tin dioxide based gas sensors, *Sensors Actuators B. Chem.* 16 (1993) 349–353. [https://doi.org/10.1016/0925-4005\(93\)85208-R](https://doi.org/10.1016/0925-4005(93)85208-R).
- [40] J. Huang, Q. Wan, Gas sensors based on semiconducting metal oxide one-dimensional nanostructures, *Sensors.* 9 (2009) 9903–9924.
<https://doi.org/10.3390/s91209903>.
- [41] N. Barsan, U. Weimar, Conduction model of metal oxide gas sensors, *J. Electroceramics.* 7 (2001) 143–167. <https://doi.org/10.1023/A:1014405811371>.
- [42] Z. Li, H. Li, Z. Wu, M. Wang, J. Luo, H. Torun, P. Hu, C. Yang, M. Grundmann, X. Liu, Y. Fu, Advances in designs and mechanisms of semiconducting metal oxide nanostructures for high-precision gas sensors operated at room temperature, *Mater. Horizons.* 6 (2019) 470–506. <https://doi.org/10.1039/c8mh01365a>.
- [43] N. Bârsan, Transduction in semiconducting metal oxide based gas sensors - Implications of the conduction mechanism, *Procedia Eng.* 25 (2011) 100–103.
<https://doi.org/10.1016/j.proeng.2011.12.025>.
- [44] H.J. Kim, J.H. Lee, Highly sensitive and selective gas sensors using p-type oxide semiconductors: Overview, *Sensors Actuators, B Chem.* 192 (2014) 607–627.
<https://doi.org/10.1016/j.snb.2013.11.005>.

- [45] M. Hübner, C.E. Simion, A. Tomescu-Stănoiu, S. Pokhrel, N. Bârsan, U. Weimar, Influence of humidity on CO sensing with p-type CuO thick film gas sensors, *Sensors Actuators, B Chem.* 153 (2011) 347–353. <https://doi.org/10.1016/j.snb.2010.10.046>.
- [46] S. Choopun, N. Hongstith, E. Wongrat, Metal-Oxide Nanowires for Gas Sensors, *Nanowires - Recent Adv.* (2012) 3–24. <https://doi.org/10.5772/54385>.
- [47] C. Xu, J. Tamaki, N. Miura, N. Yamazoe, Grain size effects on gas sensitivity of porous SnO₂-based elements, *Sensors Actuators B. Chem.* 3 (1991) 147–155. [https://doi.org/10.1016/0925-4005\(91\)80207-Z](https://doi.org/10.1016/0925-4005(91)80207-Z).
- [48] G. Korotcenkov, S.D. Han, B.K. Cho, V. Brinzari, Grain size effects in sensor response of nanostructured SnO₂- and In₂O₃-based conductometric thin film gas sensor, *Crit. Rev. Solid State Mater. Sci.* 34 (2009) 1–17. <https://doi.org/10.1080/10408430902815725>.
- [49] G. Neri, First fifty years of chemoresistive gas sensors, *Chemosensors.* 3 (2015) 1–20. <https://doi.org/10.3390/chemosensors3010001>.
- [50] Y.F. Sun, S.B. Liu, F.L. Meng, J.Y. Liu, Z. Jin, L.T. Kong, J.H. Liu, Metal oxide nanostructures and their gas sensing properties: A review, *Sensors.* 12 (2012) 2610–2631. <https://doi.org/10.3390/s120302610>.
- [51] P.J.A. Borm, D. Robbins, S. Haubold, T. Kuhlbusch, H. Fissan, K. Donaldson, R. Schins, V. Stone, W. Kreyling, J. Lademann, J. Krutmann, D.B. Warheit, E. Oberdorster, The potential risks of nanomaterials: A review carried out for ECETOC, 2006. <https://doi.org/10.1186/1743-8977-3-11>.
- [52] D.B. Kittelson, Recent Measurements of Nanoparticle Emissions from Engines Current Research on Diesel Exhaust Particles, *Curr. Res. Diesel Exhaust Part.* 9 (2001) 451–457.
- [53] C. Buzea, I.I. Pacheco, K. Robbie, Nanomaterials and nanoparticles: Sources and toxicity, *Biointerphases.* 2 (2007) MR17–MR71. <https://doi.org/10.1116/1.2815690>.
- [54] T. Kjeldstad, A. Thøgersen, M. Stange, I.T. Jensen, E. Monakhov, A. Galeckas, Surface effects and optical properties of self-assembled nanostructured a-Si:Al, *Nanomaterials.* 9 (2019) 1–12. <https://doi.org/10.3390/nano9081106>.
- [55] G. Ramalingam, P. Kathirgamanathan, G. Ravi, T. Elangovan, B. Arjun kumar, N. Manivannan, K. Kasinathan, Quantum Confinement Effect of 2D Nanomaterials, *Quantum Dots - Fundam. Appl.* (2020) 1–12. <https://doi.org/10.5772/intechopen.90140>.

- [56] T. Edvinsson, Optical quantum confinement and photocatalytic properties in two-, one- and zerodimensional nanostructures, *R. Soc. Open Sci.* 5 (2018).
<https://doi.org/10.1098/rsos.180387>.
- [57] E. Roduner, Size matters: Why nanomaterials are different, *Chem. Soc. Rev.* 35 (2006) 583–592. <https://doi.org/10.1039/b502142c>.
- [58] E. Al-Shail, A. Hassan, A. Aldowaish, H. Katt, The Cultural Reinforcers of Child Abuse, *Child Abus. Negl. - A Multidimens. Approach.* (2012).
<https://doi.org/10.5772/50693>.
- [59] C.M. Chuang, P.R. Brown, M.G. Bawendi, U. States, U. States, C. Science, U. States, U. States, Through band alignment engineering, *Nat Mater.* 13 (2014) 796–801. <https://doi.org/10.1038/nmat3984>.Improved.
- [60] Z. Yue, F. Lisdat, W.J. Parak, S.G. Hickey, L. Tu, N. Sabir, D. Dorfs, N.C. Bigall, Quantum-dot-based photoelectrochemical sensors for chemical and biological detection, *ACS Appl. Mater. Interfaces.* 5 (2013) 2800–2814.
<https://doi.org/10.1021/am3028662>.
- [61] H. Liu, S. Xu, M. Li, G. Shao, H. Song, W. Zhang, W. Wei, M. He, L. Gao, H. Song, J. Tang, Chemiresistive gas sensors employing solution-processed metal oxide quantum dot films, *Appl. Phys. Lett.* 105 (2014) 1–6.
<https://doi.org/10.1063/1.4900405>.
- [62] B. Zhang, M. Li, Z. Song, H. Kan, H. Yu, Q. Liu, G. Zhang, H. Liu, Sensitive H₂S gas sensors employing colloidal zinc oxide quantum dots, *Sensors Actuators, B Chem.* 249 (2017) 558–563. <https://doi.org/10.1016/j.snb.2017.03.098>.
- [63] S. Shao, X. Chen, Y. Chen, L. Zhang, H.W. Kim, S.S. Kim, ZnO Nanosheets Modified with Graphene Quantum Dots and SnO₂Quantum Nanoparticles for Room-Temperature H₂S Sensing, *ACS Appl. Nano Mater.* 3 (2020) 5220–5230.
<https://doi.org/10.1021/acsanm.0c00642>.
- [64] Z. Wang, T. Hu, R. Liang, M. Wei, Application of Zero-Dimensional Nanomaterials in Biosensing, *Front. Chem.* 8 (2020) 1–19. <https://doi.org/10.3389/fchem.2020.00320>.
- [65] X. Liu, T. Ma, N. Pinna, J. Zhang, Two-Dimensional Nanostructured Materials for Gas Sensing, *Adv. Funct. Mater.* 27 (2017) 1–30.
<https://doi.org/10.1002/adfm.201702168>.
- [66] G. Neri, Thin 2D: The new dimensionality in gas sensing, *Chemosensors.* 5 (2017).
<https://doi.org/10.3390/chemosensors5030021>.
- [67] C. Tan, X. Cao, X.J. Wu, Q. He, J. Yang, X. Zhang, J. Chen, W. Zhao, S. Han, G.H.

- Nam, M. Sindoro, H. Zhang, Recent Advances in Ultrathin Two-Dimensional Nanomaterials, *Chem. Rev.* 117 (2017) 6225–6331.
<https://doi.org/10.1021/acs.chemrev.6b00558>.
- [68] S.S. Varghese, S.H. Varghese, S. Swaminathan, K.K. Singh, V. Mittal, Two-dimensional materials for sensing: Graphene and beyond, *Electron.* 4 (2015) 651–687. <https://doi.org/10.3390/electronics4030651>.
- [69] R.S. Rawat, Dense Plasma Focus - From Alternative Fusion Source to Versatile High Energy Density Plasma Source for Plasma Nanotechnology, *J. Phys. Conf. Ser.* 591 (2015). <https://doi.org/10.1088/1742-6596/591/1/012021>.
- [70] P. Bächtold, P. Bächtold, Top-Down Strategy, 2013. https://doi.org/10.1007/978-94-007-5252-8_3.
- [71] S. Kumar, P. Bhushan, S. Bhattacharya, Fabrication of Nanostructures with Bottom-up Approach and Their Utility in Diagnostics, Therapeutics, and Others, 2018. https://doi.org/10.1007/978-981-10-7751-7_8.
- [72] G. Heiland, Zum Einfluß von Wasserstoff auf die elektrische Leitfähigkeit an der Oberfläche von Zinkoxydkristallen, *Zeitschrift Für Phys.* 148 (1957) 15–27. <https://doi.org/10.1007/BF01327362>.
- [73] T. Seiyama, K. Fujiishi, M. Nagatani, A. Kato, A New Detector for Gaseous Components Using Zinc Oxide Thin Films, *J. Soc. Chem. Ind. Japan.* 66 (1963) 652–655. https://doi.org/10.1246/nikkashi1898.66.5_652.
- [74] P.J. Shaver, Activated tungsten oxide gas detectors, *Appl. Phys. Lett.* 11 (1967) 255–257. <https://doi.org/10.1063/1.1755123>.
- [75] N. Taguchi, A.E. Myer, A.E. Geoffrey, Gas Detective Device, *US Pat.* (1971) 1–5.
- [76] E. Comini, Metal oxide nano-crystals for gas sensing, *Anal. Chim. Acta.* 568 (2006) 28–40. <https://doi.org/10.1016/j.aca.2005.10.069>.
- [77] E. Lee, Y.S. Yoon, D.J. Kim, Two-Dimensional Transition Metal Dichalcogenides and Metal Oxide Hybrids for Gas Sensing, *ACS Sensors.* 3 (2018) 2045–2060. <https://doi.org/10.1021/acssensors.8b01077>.
- [78] W. Zhang, P. Zhang, Z. Su, G. Wei, Synthesis and sensor applications of MoS₂-based nanocomposites, *Nanoscale.* 7 (2015) 18364–18378. <https://doi.org/10.1039/c5nr06121k>.
- [79] G. Korotcenkov, Black phosphorus-new nanostructured material for humidity sensors: Achievements and limitations, *Sensors (Switzerland).* 19 (2019). <https://doi.org/10.3390/s19051010>.

- [80] K. Rajkumar, R.T.R. Kumar, Gas sensors based on two-dimensional materials and its mechanisms, Elsevier Ltd, 2019. <https://doi.org/10.1016/B978-0-08-102577-2.00006-3>.
- [81] V. Paolucci, S.M. Emamjomeh, L. Ottaviano, C. Cantalini, Near room temperature light-activated ws₂-decorated rgo as no₂ gas sensor, *Sensors (Switzerland)*. 19 (2019). <https://doi.org/10.3390/s19112617>.
- [82] D.J. Late, T. Doneux, M. Bougouma, Single-layer MoSe₂ based NH₃ gas sensor, *Appl. Phys. Lett.* 105 (2014). <https://doi.org/10.1063/1.4903358>.
- [83] Z. Feng, Y. Xie, E. Wu, Y. Yu, S. Zheng, R. Zhang, X. Chen, C. Sun, H. Zhang, W. Pang, J. Liu, D. Zhang, Enhanced Sensitivity of MoTe₂ Chemical Sensor through Light Illumination, *Micromachines*. 8 (2017). <https://doi.org/10.3390/mi8050155>.
- [84] R. Kumar, N. Goel, M. Hojamberdiev, M. Kumar, Transition metal dichalcogenides-based flexible gas sensors, *Sensors Actuators, A Phys.* 303 (2020) 111875. <https://doi.org/10.1016/j.sna.2020.111875>.
- [85] B. Chavillon, L. Cario, A. Renaud, F. Tessier, F. Cheviré, M. Boujtita, Y. Pellegrin, E. Blart, A. Smeigh, L. Hammarström, F. Odobel, S. Jobic, P-type nitrogen-doped ZnO nanoparticles stable under ambient conditions, *J. Am. Chem. Soc.* 134 (2012) 464–470. <https://doi.org/10.1021/ja208044k>.
- [86] P.J.P. Espitia, N. de F.F. Soares, J.S. dos R. Coimbra, N.J. de Andrade, R.S. Cruz, E.A.A. Medeiros, Zinc Oxide Nanoparticles: Synthesis, Antimicrobial Activity and Food Packaging Applications, *Food Bioprocess Technol.* 5 (2012) 1447–1464. <https://doi.org/10.1007/s11947-012-0797-6>.
- [87] M.A. Borysiewicz, ZnO as a functional material, a review, *Crystals*. 9 (2019). <https://doi.org/10.3390/cryst9100505>.
- [88] C.B. Ong, L.Y. Ng, A.W. Mohammad, A review of ZnO nanoparticles as solar photocatalysts: Synthesis, mechanisms and applications, *Renew. Sustain. Energy Rev.* 81 (2018) 536–551. <https://doi.org/10.1016/j.rser.2017.08.020>.
- [89] Ü. Özgür, V. Avrutin, H. Morkoç, Zinc Oxide Materials and Devices Grown by Molecular Beam Epitaxy, 2018. <https://doi.org/10.1016/b978-0-12-812136-8.00016-5>.
- [90] R.S. Koster, C.M. Fang, M. Dijkstra, A. Van Blaaderen, M.A. Van Huis, Stabilization of rock salt ZnO nanocrystals by low-energy surfaces and Mg additions: A first-principles study, *J. Phys. Chem. C*. 119 (2015) 5648–5656. <https://doi.org/10.1021/jp511503b>.

- [91] H. Karzel, W. Potzel, M. Köfferlein, W. Schiessl, M. Steiner, U. Hiller, G. Kalvius, D. Mitchell, T. Das, Lattice dynamics and hyperfine interactions in ZnO and ZnSe at high external pressures, *Phys. Rev. B - Condens. Matter Mater. Phys.* 53 (1996) 11425–11438. <https://doi.org/10.1103/PhysRevB.53.11425>.
- [92] Ü. Özgür, Y.I. Alivov, C. Liu, A. Teke, M.A. Reshchikov, S. Doğan, V. Avrutin, S.J. Cho, H. Morkoç, A comprehensive review of ZnO materials and devices, *J. Appl. Phys.* 98 (2005) 1–103. <https://doi.org/10.1063/1.1992666>.
- [93] J. Sheng, B. Yan, J. Ye, N. Li, F. Meng, F. Huang, G. Yu, Z. Wang, J. Yan, Y. Zhang, Y. Ai, C. Shou, Y. Zeng, Room-temperature sputtered aluminum-doped zinc oxide for semitransparent perovskite solar cells, *ACS Appl. Energy Mater.* 3 (2020) 9610–9617. <https://doi.org/10.1021/acsaem.0c01081>.
- [94] P. Erhart, K. Albe, A. Klein, First-principles study of intrinsic point defects in ZnO: Role of band structure, volume relaxation, and finite-size effects, *Phys. Rev. B - Condens. Matter Mater. Phys.* 73 (2006) 1–9. <https://doi.org/10.1103/PhysRevB.73.205203>.
- [95] Y. Gao, Z.L. Wang, Electrostatic potential in a bent piezoelectric nanowire. The fundamental theory of nanogenerator and nanopiezotronics, *Nano Lett.* 7 (2007) 2499–2505. <https://doi.org/10.1021/nl071310j>.
- [96] Z. Wang, *Nanogenerators for self-powered devices and systems*, 2011.
- [97] S. Vallisree, R. Thangavel, T.R. Lenka, Theoretical investigations on enhancement of photovoltaic efficiency of nanostructured CZTS/ZnS/ZnO based solar cell device, *J. Mater. Sci. Mater. Electron.* 29 (2018) 7262–7272. <https://doi.org/10.1007/s10854-018-8715-y>.
- [98] M. Luqman, M. Napi, S.M. Sultan, R. Ismail, *Electrochemical-Based Biosensors on Different Zinc*, (2019) 1–34.
- [99] D. Medina Cruz, E. Mostafavi, A. Vernet-Crua, H. Barabadi, V. Shah, J.L. Cholula-Díaz, G. Guisbiers, T.J. Webster, Green nanotechnology-based zinc oxide (ZnO) nanomaterials for biomedical applications: a review, *J. Phys. Mater.* 3 (2020) 034005. <https://doi.org/10.1088/2515-7639/ab8186>.
- [100] A. Moumen, N. Kaur, N. Poli, D. Zappa, E. Comini, One dimensional ZnO nanostructures: Growth and chemical sensing performances, *Nanomaterials.* 10 (2020) 1–16. <https://doi.org/10.3390/nano10101940>.
- [101] L. Leontie, M. Caraman, M. Alexe, C. Harnagea, Structural and optical characteristics of bismuth oxide thin films, *Surf. Sci.* 507–510 (2002) 480–485.

[https://doi.org/10.1016/S0039-6028\(02\)01289-X](https://doi.org/10.1016/S0039-6028(02)01289-X).

- [102] A.L.J. Pereira, D. Errandonea, A. Beltrán, L. Gracia, O. Gomis, J.A. Sans, B. García-Domene, A. Miquel-Veyrat, F.J. Manjón, A. Muñoz, C. Popescu, Structural study of α -Bi₂O₃ under pressure, *J. Phys. Condens. Matter.* 25 (2013).
<https://doi.org/10.1088/0953-8984/25/47/475402>.
- [103] A. Testino, I.R. Bellobono, V. Buscaglia, C. Canevali, M. D'Arienzo, S. Polizzi, R. Scotti, F. Morazzoni, Optimizing the photocatalytic properties of hydrothermal TiO₂ by the control of phase composition and particle morphology. A systematic approach, *J. Am. Chem. Soc.* 129 (2007) 3564–3575.
<https://doi.org/10.1021/ja067050+>.
- [104] R. Chen, Z.R. Shen, H. Wang, H.J. Zhou, Y.P. Liu, D.T. Ding, T.H. Chen, Fabrication of mesh-like bismuth oxide single crystalline nanoflakes and their visible light photocatalytic activity, *J. Alloys Compd.* 509 (2011) 2588–2596.
<https://doi.org/10.1016/j.jallcom.2010.11.102>.
- [105] A.M. Abu-dief, W.S. Mohamed, UV-photocatalytic activity and UV-photocatalytic activity, (n.d.).
- [106] L. Zhang, W. Wang, J. Yang, Z. Chen, W. Zhang, L. Zhou, S. Liu, Sonochemical synthesis of nanocrystallite Bi₂O₃ as a visible-light-driven photocatalyst, *Appl. Catal. A Gen.* 308 (2006) 105–110. <https://doi.org/10.1016/j.apcata.2006.04.016>.
- [107] H.Y. Wang, Y.C. Yang, L. Le, Y. Liu, J.H. Wei, R. Xiong, J. Shi, Photocatalytic Properties of α -Bi₂O₃ Nanoneedle Array Synthesized by Hydrothermal Method, *Solid State Phenom.* 181–182 (2011) 332–335.
<https://doi.org/10.4028/www.scientific.net/ssp.181-182.332>.
- [108] M.J. Jabeen Fatima, C. V. Niveditha, S. Sindhu, α -Bi₂O₃ photoanode in DSSC and study of the electrode-electrolyte interface, *RSC Adv.* 5 (2015) 78299–78305.
<https://doi.org/10.1039/c5ra12760b>.
- [109] S. Singh, R.K. Sahoo, N.M. Shinde, J.M. Yun, R.S. Mane, K.H. Kim, Synthesis of Bi₂O₃-MnO₂ nanocomposite electrode for wide-potential window high performance supercapacitor, *Energies.* 12 (2019). <https://doi.org/10.3390/en12173320>.
- [110] K. Szostak, P. Ostaszewski, J. Pulit-Prociak, M. Banach, Bismuth Oxide Nanoparticles in Drug Delivery Systems, *Pharm. Chem. J.* 53 (2019) 48–51.
<https://doi.org/10.1007/s11094-019-01954-9>.
- [111] F. Du, J. Lou, R. Jiang, Z. Fang, X. Zhao, Y. Niu, S. Zou, M. Zhang, A. Gong, C. Wu, Hyaluronic acid-functionalized bismuth oxide nanoparticles for computed

- tomography imaging-guided radiotherapy of tumor, *Int. J. Nanomedicine*. 12 (2017) 5973–5992. <https://doi.org/10.2147/IJN.S130455>.
- [112] Y. Zhao, J. Song, G.H. Ryu, K.Y. Ko, W.J. Woo, Y. Kim, D. Kim, J.H. Lim, S. Lee, Z. Lee, J. Park, H. Kim, Low-temperature synthesis of 2D MoS₂ on a plastic substrate for a flexible gas sensor, (2018) 9338–9345. <https://doi.org/10.1039/c8nr00108a>.
- [113] T. Jrvinen, G.S. Lorite, J. Perntie, G. Toth, S. Saarakkala, V.K. Virtanen, K. Kordas, WS₂ and MoS₂ thin film gas sensors with high response to NH₃ in air at low temperature, *Nanotechnology*. 30 (2019). <https://doi.org/10.1088/1361-6528/ab2d48>.
- [114] Y. Chen, S. Lee, T. Su, S. Wu, P. Chen, process as high performance NO gas sensors with a ppb-level detection limit †, (2019) 22314–22322. <https://doi.org/10.1039/c9ta05348d>.
- [115] R. Kappera, D. Voiry, S.E. Yalcin, B. Branch, G. Gupta, A.D. Mohite, M. Chhowalla, Phase-engineered low-resistance contacts for ultrathin MoS₂ transistors, *Nat. Mater*. 13 (2014) 1128–1134. <https://doi.org/10.1038/nmat4080>.
- [116] Y. Ma, B. Liu, A. Zhang, L. Chen, M. Fathi, C. Shen, A.N. Abbas, M. Ge, M. Mecklenburg, C. Zhou, Reversible Semiconducting-to-Metallic Phase Transition in Chemical Vapor Deposition Grown Monolayer WSe₂ and Applications for Devices, *ACS Nano*. 9 (2015) 7383–7391. <https://doi.org/10.1021/acs.nano.5b02399>.
- [117] X. Wang, X. Shen, Z. Wang, R. Yu, L. Chen, Atomic-scale clarification of structural transition of MoS₂ upon sodium intercalation, *ACS Nano*. 8 (2014) 11394–11400. <https://doi.org/10.1021/nn505501v>.
- [118] D. Voß, P. Krüger, A. Mazur, J. Pollmann, Atomic and electronic structure of (formula presented) from ab initio theory: bulk crystal and thin film systems, *Phys. Rev. B - Condens. Matter Mater. Phys*. 60 (1999) 14311–14317. <https://doi.org/10.1103/PhysRevB.60.14311>.
- [119] R. Coehoorn, C. Haas, J. Dijkstra, C.J.F. Flipse, R.A. De Groot, A. Wold, Electronic structure of MoSe₂, MoS₂, and WSe₂. I. Band-structure calculations and photoelectron spectroscopy, *Phys. Rev. B*. 35 (1987) 6195–6202. <https://doi.org/10.1103/PhysRevB.35.6195>.
- [120] Z. Meng, R.M. Stolz, L. Mendecki, K.A. Mirica, Electrically-transduced chemical sensors based on two-dimensional nanomaterials, *Chem. Rev*. 119 (2019) 478–598. <https://doi.org/10.1021/acs.chemrev.8b00311>.
- [121] Q. Zhou, J. Du, J. Duan, boost electron extraction for all-inorganic tri-, (2020) 7784–7791. <https://doi.org/10.1039/d0ta01645d>.

- [122] P. Xiong, B. Sun, N. Sakai, R. Ma, T. Sasaki, S. Wang, J. Zhang, G. Wang, 2D Superlattices for Efficient Energy Storage and Conversion, 1902654 (2020) 1–12. <https://doi.org/10.1002/adma.201902654>.
- [123] Y. Li, Y.L. Li, B. Sa, R. Ahuja, Review of two-dimensional materials for photocatalytic water splitting from a theoretical perspective, *Catal. Sci. Technol.* 7 (2017) 545–559. <https://doi.org/10.1039/c6cy02178f>.
- [124] A. Eftekhari, Tungsten dichalcogenides (WS₂, WSe₂, and WTe₂): Materials chemistry and applications, *J. Mater. Chem. A* 5 (2017) 18299–18325. <https://doi.org/10.1039/c7ta04268j>.
- [125] K. Share, J. Lewis, L. Oakes, R.E. Carter, A.P. Cohn, C.L. Pint, Tungsten diselenide (WSe₂) as a high capacity, low overpotential conversion electrode for sodium ion batteries, *RSC Adv.* 5 (2015) 101262–101267. <https://doi.org/10.1039/c5ra19717a>.
- [126] Y. Wang, S. Zhao, Y. Wang, D.A. Laleyan, Y. Wu, B. Ouyang, P. Ou, J. Song, Z. Mi, Wafer-scale synthesis of monolayer WSe₂: A multi-functional photocatalyst for efficient overall pure water splitting, *Nano Energy* 51 (2018) 54–60. <https://doi.org/10.1016/j.nanoen.2018.06.047>.
- [127] X. Wang, Y. Chen, B. Zheng, F. Qi, J. He, B. Yu, W. Zhang, Significant enhancement of photocatalytic activity of multi-walled carbon nanotubes modified WSe₂ composite, *Mater. Lett.* 197 (2017) 67–70. <https://doi.org/10.1016/j.matlet.2017.03.150>.
- [128] T. Akama, W. Okita, R. Nagai, C. Li, T. Kaneko, T. Kato, Schottky solar cell using few-layered transition metal dichalcogenides toward large-scale fabrication of semitransparent and flexible power generator, *Sci. Rep.* 7 (2017) 1–10. <https://doi.org/10.1038/s41598-017-12287-6>.
- [129] C. Soc, *Chem Soc Rev* focused on the development of, (2018) 4860–4908. <https://doi.org/10.1039/c8cs00417j>.
- [130] Y.K. Yap, D. Zhang, M. Technological, *Encyclopedia of Nanotechnology*, *Encycl. Nanotechnol.* (2016) 1–8. <https://doi.org/10.1007/978-94-007-6178-0>.
- [131] A.C. Jones, M.L. Hitchman, *Overview of Chemical Vapour Deposition*, 2009.
- [132] L. Gao, W. Ren, H. Xu, L. Jin, Z. Wang, T. Ma, L.P. Ma, Z. Zhang, Q. Fu, L.M. Peng, X. Bao, H.M. Cheng, Repeated growth and bubbling transfer of graphene with millimetre-size single-crystal grains using platinum, *Nat. Commun.* 3 (2012). <https://doi.org/10.1038/ncomms1702>.
- [133] J. Coraux, A.T. N'Diaye, C. Busse, T. Michely, Structural coherency of graphene on

- Ir(111), *Nano Lett.* 8 (2008) 565–570. <https://doi.org/10.1021/nl0728874>.
- [134] P. V. Pham, Atmosphere pressure chemical vapor deposition of graphene, ArXiv. (2018). <https://doi.org/10.5772/intechopen.81293>.
- [135] S. Bhaviripudi, X. Jia, M.S. Dresselhaus, J. Kong, Role of kinetic factors in chemical vapor deposition synthesis of uniform large area graphene using copper catalyst, *Nano Lett.* 10 (2010) 4128–4133. <https://doi.org/10.1021/nl102355e>.
- [136] T. Irisawa, N. Okada, W. Mizubayashi, T. Mori, W.H. Chang, K. Koga, A. Ando, K. Endo, S. Sasaki, T. Endo, Y. Miyata, CVD growth technologies of layered MX₂ materials for real LSI applications - Position and growth direction control and gas source synthesis, *IEEE J. Electron Devices Soc.* 6 (2018) 1159–1163. <https://doi.org/10.1109/JEDS.2018.2870893>.
- [137] M. Bosi, Growth and synthesis of mono and few-layers transition metal dichalcogenides by vapour techniques: A review, *RSC Adv.* 5 (2015) 75500–75518. <https://doi.org/10.1039/c5ra09356b>.
- [138] J.P. Shupp, A.S. Kinne, H.D. Arman, Z.J. Tonzetich, Synthesis and characterization of molybdenum(0) and tungsten(0) complexes of tetramethylthiourea: Single-source precursors for MoS₂ and WS₂, *Organometallics.* 33 (2014) 5238–5245. <https://doi.org/10.1021/om500567y>.
- [139] Z. Zhang, S.J. Wang, T. Yu, T. Wu, Controlling the growth mechanism of ZnO nanowires by selecting catalysts, *J. Phys. Chem. C.* 111 (2007) 17500–17505. <https://doi.org/10.1021/jp075296a>.
- [140] J. Bruncko, M. Michalka, J. Kovac, J. Andrej, A low - temperature limit for growth of ZnO nanowires by using of laser ablation processes, *Appl. Phys. A.* (2020). <https://doi.org/10.1007/s00339-020-03477-7>.
- [141] P. Sangpour, M. Roozbehi, O. Akhavan, A. Moshfegh, ZnO Nanowires from Nanopillars: Influence of Growth Time, *Curr. Nanosci.* 5 (2012) 479–484. <https://doi.org/10.2174/157341309789377998>.
- [142] A. Labidi, C. Lambert-Mauriat, C. Jacolin, M. Bendahan, M. Maaref, K. Aguir, dc and ac characterizations of WO₃ sensors under ethanol vapors, *Sensors Actuators, B Chem.* 119 (2006) 374–379. <https://doi.org/10.1016/j.snb.2005.12.036>.
- [143] E. Comini, C. Baratto, G. Faglia, M. Ferroni, A. Vomiero, G. Sberveglieri, Quasi-one dimensional metal oxide semiconductors: Preparation, characterization and application as chemical sensors, *Prog. Mater. Sci.* 54 (2009) 1–67. <https://doi.org/10.1016/j.pmatsci.2008.06.003>.

- [144] D. Sett, D. Basak, Highly enhanced H₂ gas sensing characteristics of Co:ZnO nanorods and its mechanism, *Sensors Actuators, B Chem.* 243 (2017) 475–483. <https://doi.org/10.1016/j.snb.2016.11.163>.
- [145] T.F. Choo, N.U. Saidin, K.Y. Kok, Hydrogen sensing enhancement of zinc oxide nanorods via voltage biasing, *R. Soc. Open Sci.* 5 (2018). <https://doi.org/10.1098/rsos.172372>.
- [146] L. Chen, S. Wu, Y. Yin, <Jp908114P.Pdf>, (2009) 21572–21576.
- [147] J.B. Hannon, S. Kodambaka, F.M. Ross, R.M. Tromp, The influence of the surface migration of gold on the growth of silicon nanowires, *Nature.* 440 (2006) 69–71. <https://doi.org/10.1038/nature04574>.
- [148] N. Tamaekong, C. Liewhiran, A. Wisitsoraat, S. Phanichphant, Sensing characteristics of flame-spray-made Pt/ZnO thick films as H₂ gas sensor, *Sensors.* 9 (2009) 6652–6669. <https://doi.org/10.3390/s90906652>.
- [149] N. Yamazoe, G. Sakai, K. Shimano, Oxide semiconductor gas sensors, *Catal. Surv. from Asia.* 7 (2003) 63–75. <https://doi.org/10.1023/A:1023436725457>.
- [150] R. Bahariqushchi, S. Cosentino, M. Scuderi, E. Dumons, L.P. Tran-huu-hue, Nanoscale Free carrier enhanced depletion in ZnO nanorods decorated with bimetallic AuPt nanoclusters †, (2020). <https://doi.org/10.1039/d0nr04134c>.
- [151] X. Chen, Y. Shen, P. Zhou, X. Zhong, G. Li, C. Han, D. Wei, S. Li, Bimetallic Au/Pd nanoparticles decorated ZnO nanowires for NO₂ detection, *Sensors Actuators, B Chem.* 289 (2019) 160–168. <https://doi.org/10.1016/j.snb.2019.03.095>.
- [152] S.A. Najim, N.Y. Jamil, K.M. Muhammed, Effect of Au dopant on the structural and optical properties of ZnO thin films prepared by CVD, *J. Nano- Electron. Phys.* 11 (2019). [https://doi.org/10.21272/jnep.11\(2\).02003](https://doi.org/10.21272/jnep.11(2).02003).
- [153] H. Wang, L. Xu, J. Fan, X. Ma, Z. Wei, Y. Zou, Y. Xu, Study of solid solubility of gold doped in ZnO films and its effect on optical properties, 2015 Int. Conf. Optoelectron. Microelectron. ICOM 2015. (2016) 407–410. <https://doi.org/10.1109/ICoOM.2015.7398854>.
- [154] A. Katoch, S.W. Choi, H.W. Kim, S.S. Kim, Highly sensitive and selective H₂ sensing by ZnO nanofibers and the underlying sensing mechanism, *J. Hazard. Mater.* 286 (2015) 229–235. <https://doi.org/10.1016/j.jhazmat.2014.12.007>.
- [155] Q.A. Drmosh, Z.H. Yamani, Synthesis, characterization, and hydrogen gas sensing properties of AuNs-catalyzed ZnO sputtered thin films, *Appl. Surf. Sci.* 375 (2016) 57–64. <https://doi.org/10.1016/j.apsusc.2016.02.238>.

- [156] H.W. Kim, H.G. Na, D.S. Kwak, H.Y. Cho, Y.J. Kwon, Enhanced gas sensing characteristics of Ag₂O-functionalized networked In₂O₃ nanowires, *Jpn. J. Appl. Phys.* 52 (2013). <https://doi.org/10.7567/JJAP.52.10MD01>.
- [157] J. Ding, J. Zhu, P. Yao, J. Li, H. Bi, X. Wang, Synthesis of ZnO-Ag Hybrids and Their Gas-Sensing Performance toward Ethanol, *Ind. Eng. Chem. Res.* 54 (2015) 8947–8953. <https://doi.org/10.1021/acs.iecr.5b01711>.
- [158] D. Barreca, D. Bekermann, E. Comini, A. Devi, R.A. Fischer, A. Gasparotto, C. MacCato, G. Sberveglieri, E. Tondello, 1D ZnO nano-assemblies by Plasma-CVD as chemical sensors for flammable and toxic gases, *Sensors Actuators, B Chem.* 149 (2010) 1–7. <https://doi.org/10.1016/j.snb.2010.06.048>.
- [159] C. Baratto, F. Rigoni, G. Faglia, E. Comini, D. Zappa, G. Sberveglieri, ZnO and SnO₂ one-dimensional sensors for detection of hazardous gases, *Proc. IEEE Sensors. 2017-Decem* (2017) 1–3. <https://doi.org/10.1109/ICSENS.2017.8234326>.
- [160] A. Qurashi, N. Tabet, M. Faiz, T. Yamzaki, Ultra-fast microwave synthesis of ZnO nanowires and their dynamic response toward hydrogen gas, *Nanoscale Res. Lett.* 4 (2009) 948–954. <https://doi.org/10.1007/s11671-009-9317-7>.
- [161] M. Zhao, M.H. Wong, H.C. Man, C.W. Ong, Resistive hydrogen sensing response of Pd-decorated ZnO “nanosponge” film, *Sensors Actuators, B Chem.* 249 (2017) 624–631. <https://doi.org/10.1016/j.snb.2017.04.020>.
- [162] A. Gupta, S.S. Pandey, M. Nayak, A. Maity, S.B. Majumder, S. Bhattacharya, Hydrogen sensing based on nanoporous silica-embedded ultra dense ZnO nanobundles, *RSC Adv.* 4 (2014) 7476–7482. <https://doi.org/10.1039/c3ra45316b>.
- [163] V. Galstyan, E. Comini, C. Baratto, G. Faglia, G. Sberveglieri, Nanostructured ZnO chemical gas sensors, *Ceram. Int.* 41 (2015) 14239–14244. <https://doi.org/10.1016/j.ceramint.2015.07.052>.
- [164] Z. El khalidi, E. Comini, B. Hartiti, A. Moumen, H.M.M. Munasinghe Arachchige, S. Fadili, P. Thevenin, A. Kamal, Effect of vanadium doping on ZnO sensing properties synthesized by spray pyrolysis, *Mater. Des.* 139 (2018) 56–64. <https://doi.org/10.1016/j.matdes.2017.10.074>.
- [165] M. Tonezzer, S. Iannotta, H₂ sensing properties of two-dimensional zinc oxide nanostructures, *Talanta.* 122 (2014) 201–208. <https://doi.org/10.1016/j.talanta.2014.01.051>.
- [166] L.J. Bie, X.N. Yan, J. Yin, Y.Q. Duan, Z.H. Yuan, Nanopillar ZnO gas sensor for hydrogen and ethanol, *Sensors Actuators, B Chem.* 126 (2007) 604–608.

<https://doi.org/10.1016/j.snb.2007.04.011>.

- [167] S. Ren, G. Fan, S. Qu, Q. Wang, Enhanced H₂ sensitivity at room temperature of ZnO nanowires functionalized by Pd nanoparticles, *J. Appl. Phys.* 110 (2011). <https://doi.org/10.1063/1.3647310>.
- [168] M. Drobek, J.H. Kim, M. Bechelany, C. Vallicari, A. Julbe, S.S. Kim, MOF-Based Membrane Encapsulated ZnO Nanowires for Enhanced Gas Sensor Selectivity, *ACS Appl. Mater. Interfaces.* 8 (2016) 8323–8328. <https://doi.org/10.1021/acsami.5b12062>.
- [169] S.K. Hazra, S. Basu, Hydrogen sensitivity of ZnO p-n homojunctions, *Sensors Actuators, B Chem.* 117 (2006) 177–182. <https://doi.org/10.1016/j.snb.2005.11.018>.
- [170] H.S. Al-Salman, M.J. Abdullah, N. Al-Hardan, ZnO thin film nanostructures for hydrogen gas sensing applications, *Ceram. Int.* 39 (2013) S447–S450. <https://doi.org/10.1016/j.ceramint.2012.10.111>.
- [171] F. Teimoori, K. Khojier, N.Z. Dehnavi, On the Dependence of H₂ Gas Sensitivity of ZnO thin Films on Film Thickness, *Procedia Mater. Sci.* 11 (2015) 474–479. <https://doi.org/10.1016/j.mspro.2015.11.061>.
- [172] V.S. Bhati, S. Ranwa, M. Fanetti, M. Valant, M. Kumar, Efficient hydrogen sensor based on Ni-doped ZnO nanostructures by RF sputtering, *Sensors Actuators, B Chem.* 255 (2018) 588–597. <https://doi.org/10.1016/j.snb.2017.08.106>.
- [173] F.-H. Chu, C.-W. Huang, C.-L. Hsin, C.-W. Wang, S.-Y. Yu, P.-H. Yeh, W.-W. Wu, Well-aligned ZnO nanowires with excellent field emission and photocatalytic properties, *Nanoscale.* 4 (2012) 1471–1475. <https://doi.org/10.1039/c1nr10796h>.
- [174] E. Teblum, Y. Gofer, C.L. Pint, G.D. Nessim, Role of catalyst oxidation state in the growth of vertically aligned carbon nanotubes, *J. Phys. Chem. C.* 116 (2012) 24522–24528. <https://doi.org/10.1021/jp305169b>.
- [175] M. Kumar, V. Bhatt, A.C. Abhyankar, J. Kim, A. Kumar, S.H. Patil, J.H. Yun, New insights towards strikingly improved room temperature ethanol sensing properties of p-Type Ce-doped SnO₂ sensors, *Sci. Rep.* 8 (2018) 1–12. <https://doi.org/10.1038/s41598-018-26504-3>.
- [176] F. Wang, H. Li, Z. Yuan, Y. Sun, F. Chang, H. Deng, L. Xie, H. Li, A highly sensitive gas sensor based on CuO nanoparticles synthesized: Via a sol-gel method, *RSC Adv.* 6 (2016) 79343–79349. <https://doi.org/10.1039/c6ra13876d>.
- [177] S. Matsushima, Y. Teraoka, N. Miura, N. Yamazoe, Electronic interaction between metal additives and tin dioxide in tin dioxide-based gas sensors, *Jpn. J. Appl. Phys.*

- 27 (1988) 1798–1802. <https://doi.org/10.1143/JJAP.27.1798>.
- [178] K. Jia, J.L. Bijeon, P.M. Adam, R.E. Ionescu, Large Scale Fabrication of Gold Nano-Structured Substrates Via High Temperature Annealing and Their Direct Use for the LSPR Detection of Atrazine, *Plasmonics*. 8 (2013) 143–151. <https://doi.org/10.1007/s11468-012-9444-3>.
- [179] X. Gou, R. Li, G. Wang, Z. Chen, D. Wexler, Room-temperature solution synthesis of Bi₂O₃ nanowires for gas sensing application, *Nanotechnology*. 20 (2009). <https://doi.org/10.1088/0957-4484/20/49/495501>.
- [180] S. Park, S. Kim, G.J. Sun, C. Lee, Synthesis, structure, and ethanol gas sensing properties of In₂O₃ nanorods decorated with Bi₂O₃ nanoparticles, *ACS Appl. Mater. Interfaces*. 7 (2015) 8138–8146. <https://doi.org/10.1021/acsami.5b00972>.
- [181] S. Wang, J. Cao, W. Cui, L. Fan, X. Li, D. Li, Facile synthesis of bamboo raft-like Co₃O₄ with enhanced acetone gas sensing performances, *J. Alloys Compd.* 758 (2018) 45–53. <https://doi.org/10.1016/j.jallcom.2018.05.139>.
- [182] N. Hongsith, C. Viriyaworasakul, P. Mangkorntong, N. Mangkorntong, S. Choopun, Ethanol sensor based on ZnO and Au-doped ZnO nanowires, *Ceram. Int.* 34 (2008) 823–826. <https://doi.org/10.1016/j.ceramint.2007.09.099>.
- [183] X. Zhang, B. Dong, W. Liu, X. Zhou, M. Liu, X. Sun, J. Lv, L. Zhang, W. Xu, X. Bai, L. Xu, S. Mintova, H. Song, Highly sensitive and selective acetone sensor based on three-dimensional ordered WO₃/Au nanocomposite with enhanced performance, *Sensors Actuators, B Chem.* 320 (2020) 128405. <https://doi.org/10.1016/j.snb.2020.128405>.
- [184] F. Teimoori, K. Khojier, N.Z. Dehnavi, Investigation of sensitivity and selectivity of ZnO thin film to volatile organic compounds, *J. Theor. Appl. Phys.* 11 (2017) 157–163. <https://doi.org/10.1007/s40094-017-0253-0>.
- [185] N. Kaur, D. Zappa, M. Ferroni, N. Poli, M. Campanini, R. Negrea, E. Comini, Branch-like NiO/ZnO heterostructures for VOC sensing, *Sensors Actuators, B Chem.* 262 (2018) 477–485. <https://doi.org/10.1016/j.snb.2018.02.042>.
- [186] Y. Liu, G. Li, R. Mi, C. Deng, P. Gao, An environment-benign method for the synthesis of p-NiO/n-ZnO heterostructure with excellent performance for gas sensing and photocatalysis, *Sensors Actuators, B Chem.* 191 (2014) 537–544. <https://doi.org/10.1016/j.snb.2013.10.068>.
- [187] V. Galstyan, E. Comini, C. Baratto, A. Ponzoni, M. Ferroni, N. Poli, E. Bontempi, M.

- Brisotto, G. Faglia, G. Sberveglieri, Large surface area biphasic titania for chemical sensing, *Sensors Actuators, B Chem.* 209 (2015) 1091–1096.
<https://doi.org/10.1016/j.snb.2014.12.027>.
- [188] W. Geng, S. Ge, X. He, S. Zhang, J. Gu, X. Lai, H. Wang, Q. Zhang, Volatile Organic Compound Gas-Sensing Properties of Bimodal Porous α -Fe₂O₃ with Ultrahigh Sensitivity and Fast Response, *ACS Appl. Mater. Interfaces.* 10 (2018) 13702–13711. <https://doi.org/10.1021/acsami.8b02435>.
- [189] T.J. Hsueh, C.L. Hsu, S.J. Chang, I.C. Chen, Laterally grown ZnO nanowire ethanol gas sensors, *Sensors Actuators, B Chem.* 126 (2007) 473–477.
<https://doi.org/10.1016/j.snb.2007.03.034>.
- [190] Z. El khalidi, B. Hartiti, S. Fadili, P. Thevenin, Nickel oxide optimization using Taguchi design for hydrogen detection, *Int. J. Hydrogen Energy.* 43 (2018) 12574–12583. <https://doi.org/10.1016/j.ijhydene.2018.04.162>.
- [191] Z.H. Ma, R.T. Yu, J.M. Song, Facile synthesis of Pr-doped In₂O₃ nanoparticles and their high gas sensing performance for ethanol, *Sensors Actuators, B Chem.* 305 (2020) 127377. <https://doi.org/10.1016/j.snb.2019.127377>.
- [192] J. Guo, J. Zhang, H. Gong, D. Ju, B. Cao, Au nanoparticle-functionalized 3D SnO₂ microstructures for high performance gas sensor, *Sensors Actuators, B Chem.* 226 (2016) 266–272. <https://doi.org/10.1016/j.snb.2015.11.140>.
- [193] F. Li, X. Gao, R. Wang, T. Zhang, Design of WO₃-SnO₂ core-shell nanofibers and their enhanced gas sensing performance based on different work function, *Appl. Surf. Sci.* 442 (2018) 30–37. <https://doi.org/10.1016/j.apsusc.2018.02.122>.
- [194] N. Banerjee, S. Roy, C.K. Sarkar, P. Bhattacharyya, Effect of Humidity on Ethanol Sensing Performance of Pd Sensitized ZnO Nanorod Based Sensors, *J. Surfaces Interfaces Mater.* 2 (2014) 154–160. <https://doi.org/10.1166/jsim.2014.1042>.
- [195] T. Lin, X. Lv, Z. Hu, A. Xu, C. Feng, Semiconductor metal oxides as chemoresistive sensors for detecting volatile organic compounds, 2019.
<https://doi.org/10.3390/s19020233>.
- [196] H. Farahani, R. Wagiran, M.N. Hamidon, Humidity Sensors Principle, Mechanism, and Fabrication Technologies: A Comprehensive Review, 2014.
<https://doi.org/10.3390/s140507881>.
- [197] D. Acharyya, P. Bhattacharyya, Alcohol sensing performance of ZnO hexagonal nanotubes at low temperatures: A qualitative understanding, *Sensors Actuators, B Chem.* 228 (2016) 373–386. <https://doi.org/10.1016/j.snb.2016.01.035>.

- [198] Q. Qi, T. Zhang, X. Zheng, H. Fan, L. Liu, R. Wang, Y. Zeng, Electrical response of Sm₂O₃-doped SnO₂ to C₂H₂ and effect of humidity interference, *Sensors Actuators, B Chem.* 134 (2008) 36–42. <https://doi.org/10.1016/j.snb.2008.04.011>.
- [199] J. Burgués, J.M. Jiménez-Soto, S. Marco, Estimation of the limit of detection in semiconductor gas sensors through linearized calibration models, *Anal. Chim. Acta.* 1013 (2018) 13–25. <https://doi.org/10.1016/j.aca.2018.01.062>.
- [200] V. Galstyan, N. Poli, A. D'Arco, S. Maclis, S. Lupi, E. Comini, A novel approach for green synthesis of WO₃nanomaterials and their highly selective chemical sensing properties, *J. Mater. Chem. A.* 8 (2020) 20373–20385. <https://doi.org/10.1039/d0ta06418a>.
- [201] G. Ejaimi, S. Saeed, An Introduction to Airway Assessment and Management (Concise Airway Anatomy and Pathophysiology), *Ann. Int. Med. Dent. Res.* 3 (2016) 1–7. <https://doi.org/10.21276/aimdr.2017.3.1.an1>.
- [202] J.H. Park, S. Vishwanath, X. Liu, H. Zhou, S.M. Eichfeld, S.K. Fullerton-Shirey, J.A. Robinson, R.M. Feenstra, J. Furdyna, D. Jena, H.G. Xing, A.C. Kummel, Scanning Tunneling Microscopy and Spectroscopy of Air Exposure Effects on Molecular Beam Epitaxy Grown WSe₂ Monolayers and Bilayers, *ACS Nano.* 10 (2016) 4258–4267. <https://doi.org/10.1021/acsnano.5b07698>.
- [203] J.H. Park, S. Vishwanath, S. Wolf, K. Zhang, I. Kwak, M. Edmonds, M. Breedon, X. Liu, M. Dobrowolska, J. Furdyna, J.A. Robinson, H.G. Xing, A.C. Kummel, Selective Chemical Response of Transition Metal Dichalcogenides and Metal Dichalcogenides in Ambient Conditions, *ACS Appl. Mater. Interfaces.* 9 (2017) 29255–29264. <https://doi.org/10.1021/acsmi.7b08244>.
- [204] R. Konar, Rosy, I. Perelshtein, E. Teblum, M. Telkhozhayeva, M. Tkachev, J.J. Richter, E. Cattaruzza, A. Pietropolli Charmet, P. Stoppa, M. Noked, G.D. Nessim, Scalable Synthesis of Few-Layered 2D Tungsten Diselenide (2H-WSe₂) Nanosheets Directly Grown on Tungsten (W) Foil Using Ambient-Pressure Chemical Vapor Deposition for Reversible Li-Ion Storage, *ACS Omega.* (2020). <https://doi.org/10.1021/acsomega.0c01155>.
- [205] N.T. Thang, L.T. Hong, N.H. Thoan, C.M. Hung, N. Van Duy, N. Van Hieu, N.D. Hoa, Controlled synthesis of ultrathin MoS₂ nanoflowers for highly enhanced NO₂ sensing at room temperature, *RSC Adv.* 10 (2020) 12759–12771. <https://doi.org/10.1039/d0ra00121j>.
- [206] P. Zhao, D. Kiriya, A. Azcatl, C. Zhang, M. Tosun, Y.S. Liu, M. Hettick, J.S. Kang, S.

- McDonnell, S. Kc, J. Guo, K. Cho, R.M. Wallace, A. Javey, Air stable p-doping of WSe₂ by covalent functionalization, *ACS Nano*. 8 (2014) 10808–10814.
<https://doi.org/10.1021/nn5047844>.
- [207] D. Ma, B. Ma, Z. Lu, C. He, Y. Tang, Z. Lu, Z. Yang, Interaction between H₂O, N₂, CO, NO, NO₂ and N₂O molecules and a defective WSe₂ monolayer, *Phys. Chem. Chem. Phys.* 19 (2017) 26022–26033. <https://doi.org/10.1039/c7cp04351a>.
- [208] F. Yavari, Z. Chen, A. V. Thomas, W. Ren, H.M. Cheng, N. Koratkar, High sensitivity gas detection using a macroscopic three-dimensional graphene foam network, *Sci. Rep.* 1 (2011) 1–5. <https://doi.org/10.1038/srep00166>.
- [209] S. Tongay, J. Suh, C. Ataca, W. Fan, A. Luce, J.S. Kang, J. Liu, C. Ko, R. Raghunathanan, J. Zhou, F. Ogletree, J. Li, J.C. Grossman, J. Wu, Defects activated photoluminescence in two-dimensional semiconductors: Interplay between bound, charged, and free excitons, *Sci. Rep.* 3 (2013) 1–5.
<https://doi.org/10.1038/srep02657>.
- [210] D.J. Late, Y.K. Huang, B. Liu, J. Acharya, S.N. Shirodkar, J. Luo, A. Yan, D. Charles, U. V. Waghmare, V.P. Dravid, C.N.R. Rao, Sensing behavior of atomically thin-layered MoS₂ transistors, *ACS Nano*. 7 (2013) 4879–4891.
<https://doi.org/10.1021/nn400026u>.
- [211] T.R. Thurston, J.P. Wilcoxon, Photooxidation of organic chemicals catalyzed by nanoscale MoS₂, *J. Phys. Chem. B*. 103 (1999) 11–17.
<https://doi.org/10.1021/jp982337h>.
- [212] Q. He, Z. Zeng, Z. Yin, H. Li, S. Wu, X. Huang, H. Zhang, Fabrication of flexible MoS₂ thin-film transistor arrays for practical gas-sensing applications, *Small*. 8 (2012) 2994–2999. <https://doi.org/10.1002/smll.201201224>.
- [213] V.M. Bermudez, Computational Study of the Adsorption of NO₂ on Monolayer MoS₂, (2020). <https://doi.org/10.1021/acs.jpcc.0c03786>.
- [214] K.D. Rasamani, F. Alimohammadi, Y. Sun, Interlayer-expanded MoS₂, *Mater. Today*. 20 (2017) 83–91. <https://doi.org/10.1016/j.mattod.2016.10.004>.
- [215] C. Balamurugan, S.J. Song, H.S. Kim, Enhancing gas response characteristics of mixed metal oxide gas sensors, *J. Korean Ceram. Soc.* 55 (2018) 1–20.
<https://doi.org/10.4191/kcers.2018.55.1.10>.
- [216] C.M. Hung, D.T.T. Le, N. Van Hieu, On-chip growth of semiconductor metal oxide nanowires for gas sensors: A review, *J. Sci. Adv. Mater. Devices*. 2 (2017) 263–285.
<https://doi.org/10.1016/j.jsamd.2017.07.009>.

- [217] S. Goutham, K.K. Sadasivuni, D.S. Kumar, K.V. Rao, Flexible ultra-sensitive and resistive NO₂ gas sensor based on nanostructured Zn(X)Fe(1-x)2O₄, *RSC Adv.* 8 (2018) 3243–3249. <https://doi.org/10.1039/c7ra10478b>.
- [218] J. Huang, J. Chu, Z. Wang, J. Zhang, A. Yang, X. Li, C. Gao, H. Huang, X. Wang, Y. Cheng, M. Rong, Chemisorption of NO₂ to MoS₂ Nanostructures and its Effects for MoS₂ Sensors, *ChemNanoMat.* 5 (2019) 1123–1130. <https://doi.org/10.1002/cnma.201900350>.
- [219] Y. Zhou, G. Liu, X. Zhu, Y. Guo, Ultrasensitive NO₂ gas sensing based on rGO/MoS₂ nanocomposite film at low temperature, *Sensors Actuators, B Chem.* 251 (2017) 280–290. <https://doi.org/10.1016/j.snb.2017.05.060>.
- [220] W. Yuan, L. Huang, Q. Zhou, G. Shi, Ultrasensitive and selective nitrogen dioxide sensor based on self-assembled graphene/polymer composite nanofibers, *ACS Appl. Mater. Interfaces.* 6 (2014) 17003–17008. <https://doi.org/10.1021/am504616c>.
- [221] R. Guo, Y. Han, C. Su, X. Chen, M. Zeng, N. Hu, Y. Su, Z. Zhou, H. Wei, Z. Yang, Ultrasensitive room temperature NO₂ sensors based on liquid phase exfoliated WSe₂ nanosheets, *Sensors Actuators, B Chem.* 300 (2019) 127013. <https://doi.org/10.1016/j.snb.2019.127013>.
- [222] M.J. Kang, J.Y. Kim, J. Seo, S. Lee, C. Park, S.M. Song, S.S. Kim, M.G. Hahm, Atomic-Layered Tungsten Diselenide-Based Porous 3D Architecturing for Highly Sensitive Chemical Sensors, *Phys. Status Solidi - Rapid Res. Lett.* 13 (2019) 3–8. <https://doi.org/10.1002/pssr.201900340>.
- [223] B. Cho, A.R. Kim, D.J. Kim, H.S. Chung, S.Y. Choi, J.D. Kwon, S.W. Park, Y. Kim, B.H. Lee, K.H. Lee, D.H. Kim, J. Nam, M.G. Hahm, Two-Dimensional Atomic-Layered Alloy Junctions for High-Performance Wearable Chemical Sensor, *ACS Appl. Mater. Interfaces.* 8 (2016) 19635–19642. <https://doi.org/10.1021/acsami.6b05943>.
- [224] K.Y. Ko, K. Park, S. Lee, Y. Kim, W.J. Woo, D. Kim, J.G. Song, J. Park, H. Kim, Recovery Improvement for Large-Area Tungsten Diselenide Gas Sensors, *ACS Appl. Mater. Interfaces.* 10 (2018) 23910–23917. <https://doi.org/10.1021/acsami.8b07034>.
- [225] F. Ricciardella, K. Lee, T. Stelz, O. Hartwig, M. Prectl, M. McCrystall, N. McEvoy, G.S. Duesberg, Calibration of Nonstationary Gas Sensors Based on Two-Dimensional Materials, *ACS Omega.* 5 (2020) 5959–5963. <https://doi.org/10.1021/acsomega.9b04325>.

[226] W.S. Lee, J. Choi, Two-Dimensional Tungsten Diselenides Integrated on Paper Substrate for Highly Flexible and Sensitive Gas Sensor, 2019 20th Int. Conf. Solid-State Sensors, Actuators Microsystems Eurosensors XXXIII, TRANSDUCERS 2019 EUROSENSORS XXXIII. (2019) 681–684.
<https://doi.org/10.1109/TRANSDUCERS.2019.8808482>.

ACKNOWLEDGEMENT

First, I would like to express my sincere gratitude to my supervisor **Prof. Elisabetta Comini** for the valuable guidance, helpful discussion, trust, generous help, constant encouragement, valuable insights concerning my research and dedication for making this thesis possible.

I would like to extend my profound gratitude to my co-supervisor **Dr. Dario Zappa** for the help, guidance and useful discussion and constant encouragement during the last years.

I would like to thank **Nicole Poli** for his kindness and his consistent help to make this thesis possible.

Great thanks to all my colleagues (**Navpreet, Vardan, Giorgio, Mandeep, Chaturanga and Hakime**) in SENSOR laboratory.

Great Thanks to my family and all my friends for the support they have given me.

List of publications

➤ Articles under review

1. **Abderrahim Moumen**, Navpreet Kaur, Dario Zappa and Elisabetta Comini, Evaporation condensation growth of one-dimensional metal oxide at SENSOR Lab in Brescia for chemical sensors applications, AISEM 2021, proceeding. (Submitted)

➤ **Accepted articles**

1. **Abderrahim Moumen**, Dario Zappa, Nicola Poli and Elisabetta Comini, Catalyst-assisted vapor liquid solid growth of α -Bi₂O₃ nanowires for acetone and ethanol detection, Sensors and Actuators B: Chemical, 2020. (IF: 7.1)
2. **Abderrahim Moumen**, Rajashree Konar, Dario Zappa, Eti Teblum, Ilana Perelshtein, Ronit Lavi, Sharon Ruthstein, Gilbert Daniel Nessim and Elisabetta Comini, Robust room-temperature NO₂ sensors from exfoliated 2D few-layered CVD-grown bulk Tungsten di-selenide (2H-WSe₂), ACS Applied Materials and Interfaces, 2020. (IF: 8.7)
3. **Moumen, A.**, Kaur, N., Poli, N., Zappa, D., Comini, E. One dimensional ZnO nanostructures: Growth and chemical sensing performances. Nanomaterials, 2020. (IF: 4.3)
4. Hakkoum, H, Tibermacine, T., Sengouga, N., Belahssen, O., Ghougali, M., Benhaya, **A., Moumen, A.**, Comini, E., Effect of the source solution quantity on optical characteristics of ZnO and NiO thin films grown by spray pyrolysis for the design NiO/ZnO photodetectors, Optical Materials, 2020. (IF: 2.7)
5. Navpreet Kaur, Mandeep Singh, **Abderrahim Moumen**, Giorgio Duina and Elisabetta Comini, 1D Titanium Dioxide: Achievements in Chemical Sensing, Materials, 2020. (IF: 3.5)
6. Mauro Epifani, Saulius Kaciulis, Alessio Mezzi, Ting Zhang, Jordi Arbiol, Pietro Siciliano, Anton Landström, Isabella Concina, **Abderrahim Moumen**, Elisabetta

Comini, Chu Xiang feng, Rhodium as efficient additive for boosting acetone sensing by TiO₂ nanocrystals. Beyond the classical view of noble metal additives, Sensors and Actuators B: Chemical, 2020. (IF: 7.1)

7. **Moumen**, B. Hartiti, E. Comini, Z. El khalidi, H. M. M. M. Arachchige, S. Fadili, P. Thevenin, Preparation and characterization of nanostructured CuO thin films using spray pyrolysis technique, Superlattices and Microstructures, 127, Pages 2-10 (2019). (IF: 2.12)

List of Conferences

➤ As presenter of oral or poster presentations

1. Oral communication title « Bi₂O₃ and ZnO nanowires growth using Vapor–Liquid–Solid (VLS) process for chemical sensors applications.

Abderrahim Moumen*, Navpreet Kaur, Dario Zappa, Nicola Poli, Elisabetta Comini

» At the 37th International Symposium on Dynamical Properties of Solids - DyProSo, 8-12 September 2019, in Ferrara, Italy.

2. Presented poster title: One dimensional ZnO nanostructures: growth control and chemical sensors performance

Abderrahim Moumen*, Navpreet Kaur, Dario Zappa, Nicola Poli, Elisabetta Comini.

At the European Materials Research Society (E-MRS) conference. May 27 to 31, 2019, in Nice, France.

➤ As Co-author of oral or poster presentations

1. (KEYNOTE) Giorgio Duina, Vardan Galstyan, Navpreet Kaur, **Abderrahim Moumen**, Nicola Poli, Mandeep Singh, Dario Zappa, **Elisabetta Comini**, "Metal oxides nano-

- and hetero-structures for chemical sensors", International Research Conference 2020, 17 June 2020, Sri Lanka Technological Campus (SLTC), web conference.
2. (KEYNOTE) Vardan Galstyan, Giorgio Duina, Navpreet Kaur, **Abderrahim Moumen**, Mandeep Singh, Dario Zappa, **Elisabetta Comini**, "Metal Oxides Nanostructures for Chemical Sensing", ICSEHV 2020 International Conference on Advances in Sensors, Energy and Hybrid Vehicles, Web Conference, 14-16 October 2020.
 3. (Oral presentation) **Elisabetta Comini**, "Metal oxide nanostructures for chemical sensing", Webinar on Nanomedicine, Nanomaterials and Nanotechnology, 17-20 Novembre 2020.
 4. (KEYNOTE) Vardan Galstyan, Giorgio Duina, Navpreet Kaur, **Abderrahim Moumen**, Mandeep Singh, Dario Zappa, **Elisabetta Comini** "Chemical/gas sensors based on metal oxide nanowires and heterostructures", MEMS the word – solid state and integrated gas sensors, GASG's 3rd online meeting, Thursday 25th March.
 5. (KEYNOTE) V. Galstyan, N. Kaur, **A. Moumen**, H.M. Munashinge, O. Sisman, G. Sberveglieri, D. Zappa, **E. Comini**, << Metal oxide nanostructures: growth and application to chemical sensing >>, TCM 2018, Crete, Greece, 14-19 October 2018